



저작자표시-비영리-변경금지 2.0 대한민국

이용자는 아래의 조건을 따르는 경우에 한하여 자유롭게

- 이 저작물을 복제, 배포, 전송, 전시, 공연 및 방송할 수 있습니다.

다음과 같은 조건을 따라야 합니다:



저작자표시. 귀하는 원저작자를 표시하여야 합니다.



비영리. 귀하는 이 저작물을 영리 목적으로 이용할 수 없습니다.



변경금지. 귀하는 이 저작물을 개작, 변형 또는 가공할 수 없습니다.

- 귀하는, 이 저작물의 재이용이나 배포의 경우, 이 저작물에 적용된 이용허락조건을 명확하게 나타내어야 합니다.
- 저작권자로부터 별도의 허가를 받으면 이러한 조건들은 적용되지 않습니다.

저작권법에 따른 이용자의 권리는 위의 내용에 의하여 영향을 받지 않습니다.

이것은 [이용허락규약\(Legal Code\)](#)을 이해하기 쉽게 요약한 것입니다.

[Disclaimer](#)

공학박사 학위논문

**Development of Megasonic-Spray Coating
Technology for Thin-Film Fabrication and Its
Solar Cell Application**

**박막 제조를 위한 메가소닉 스프레이 코팅 기술
개발 및 태양전지 응용**

2022년 8월

서울대학교 대학원

기계항공공학부

박민철

박막 제조를 위한 메가소닉 스프레이 코팅 기술 개발 및 태양전지 응용

Development of Megasonic-Spray Coating Technology
for Thin-Film Fabrication and Its Solar Cell Application

지도교수 최 만 수

이 논문을 공학박사 학위논문으로 제출함

2022 년 4 월

서울대학교 대학원

기계항공공학부

박 민 철

박민철의 공학박사 학위논문을 인준함

2022 년 6 월

위원장 : 이 윤 석 (인)

부위원장 : 최 만 수 (인)

위원 : 고 승 환 (인)

위원 : 장 세 근 (인)

위원 : 이 건 희 (인)

Development of Megasonic-Spray Coating Technology for Thin-Film Fabrication and Its Solar Cell Application

Mincheol Park
School of Mechanical and Aerospace Engineering
The Graduate School
Seoul National University

Abstract

Organometallic halide perovskite solar cells (PSCs) are highly promising next-generation photovoltaic power sources for solar energy conversion. State-of-the-art glass-substrates based PSCs have achieved power conversion efficiencies (PCEs) over 25%. This led to the increasing demand for flexible-substrate based PSCs (f-PSCs) which boast a variety of potential applications. In line with this trend, commercialization of PSCs enormously requires large-area continuous coating methods beyond spin-coating based lab-scale process. First, we developed a megasonic-spray coating method utilizing 1.7 MHz megasonic oscillator that could fabricate reproducible large-area planar efficient perovskite films on the glass substrates. As a result, our devices have reached a maximum efficiency of 16.9%, with an average efficiency of 16.4% from 21 samples. We also demonstrate the applicability of megasonic-spray coating to the fabrication of large-single cells, with a power conversion efficiency of 14.2% (active area : 1 cm², coating area : 7.5 x 7.5 cm²). Our megasonic-spray coating approach is therefore expected to be suitable for

large-area coating process. Second, we came up with a Film-Growth-Megasonic-Spray-Coating (FGMSC) method that continuously grows uniform perovskite film on large-area flexible substrates. The fundamental principles of perovskite film growth mechanisms on the flexible substrate via spray-coating were thoroughly investigated. As a result, we successfully fabricated defect-free uniform perovskite film on the flexible substrates via the FGMSC system. The scalability of this system is proved through fabrication of a flexible perovskite solar mini-module with PCE of 16.10% from an active area of 35.1 cm². These results prove that our FGMSC system is the automated scalable-coating system suitable for commercialization of f-PSCs for its scalability and efficiency. Third, the megasonic-spray method was applied to the coating of charge transport layers (e.g. hole transport layer and electron transport layer). Especially, we coated a PTAA (poly(triaryl amine)) thin-film which is one of the hole transport layers and successfully fabricated highly efficient PSCs. These results have significance in that all layers of the perovskite solar devices are fabricated by large-area continuous coating process. Our megasonic-spray coating system, therefore, is a highly practical, continuous fabrication technique for photovoltaic applications.

Keyword : perovskite solar cells, flexible perovskite solar cells, continuous fabrication, scalable process, megasonic-spray-coating

Student Number : 2016-20652

Table of Contents

Abstract	i
Table of Contents	iii
List of Tables	vii
List of Figures	ix
Nomenclature	xv
Chapter 1. Introduction	1
1.1. Background.....	1
1.1.1. Demand for the Megasonic-Spray Coating System	2
1.1.2. Demand for the Film-Growth-Megasonic-Spray-Coating System.....	5
1.2. Research Objectives.....	9
1.3. Thesis Outline	11
1.4. References.....	13
Chapter 2. Megasonic-Spray Coating System for Glass-Based Perovskite Solar Cells Fabrication.....	17
2.1. Introduction.....	17
2.2. Results and Discussion	22
2.2.1. Design of Megasonic-Spray Coating Process	22
2.2.2. Investigation of Perovskite Films According to Supply Rate of	

Droplets	24
2.2.3. Fabrication of PSCs and Device Characteristics.....	28
2.2.4. Scalability of Megasonic-Spray Coating Process	41
2.3. Conclusion	48
2.4. Experimental Methods.....	49
2.4.1. Fabrication of Megasonic-Spray Coated Perovskite Solar Cells	49
2.4.2. Characterizations and Measurements.....	50
2.5. References.....	52

Chapter 3. Film-Growth-Megasonic-Spray-Coating System for Flexible Perovskite Solar Cells and Modules..... 57

3.1. Introduction.....	57
3.2. Results and Discussion	63
3.2.1. Steady Production of Fine Perovskite Precursor Droplets .	63
3.2.2. Relation among Film Coverage, Crystal Growth and Supply Rate of Droplets	67
3.2.3. Film-Growth-Megasonic-Spray-Coating (FGMSC) Technique	70
3.2.4. Fabrication of f-PSCs and Device Performance	78
3.2.5. Large-Area (100 cm ²) f-PSCs and Flexible Perovskite Solar Mini-Module	88
3.3. Conclusion	98

3.4. Experimental Methods	99
3.4.1. Design of the FGMSC System	99
3.4.2. Fabrication of f-PSCs Using the FGMSC System	100
3.4.3. Characterizations and Measurements	102
3.5. References	104
Chapter 4. Charge Transport Layer Coating via Megasonic-Spray Coating System	109
4.1. Introduction	109
4.2. Results and Discussion	111
4.2.1. Optimization of the Substrate Temperature and Multiple Megasonic-Spray Coatings	111
4.2.2. Fabrication of PSCs and Device Performance	120
4.3. Conclusion	124
4.4. Experimental Methods	125
4.4.1. Fabrication of PSCs Using the Megasonic-Spray Coating System	125
4.4.2. Characterizations and Measurements	126
4.5. References	127
Chapter 5. Concluding Remarks	128
Acknowledgement	130

Abstract in Korean	131
List of Publications	133

List of Tables

Table 2.1. Photovoltaic parameters of 15 mm/s devices with and active area of 0.0754 cm ² under 1 sun illumination.....	32
Table 2.2. Maximum photovoltaic parameters of perovskite solar cells at different megasonic-spray coating scan speeds. The last line reports averages over 21 devices with a scan speed of 15 mm/s. The active area was 0.0754 cm ²	33
Table 2.3. Tri-exponential fitting parameters of the TRPL decay for the megasonic-spray coated perovskite films on a bare glass substrate	34
Table 2.4. The calculated mobility, average lifetime and diffusion length of spray coated perovskite films.....	35
Table 2.5. The photovoltaic performance parameters from reverse and forward scan of the best large (1 cm ²) perovskite solar cells obtained with a megasonic-spray coating scan speed of 15 mm/s	42
Table 2.6. Photovoltaic parameters of 15 mm/s devices with and active area of 1 cm ² under 1 sun illumination.....	43
Table 3.1. Thickness of perovskite layers at selected positions (A-C).....	73
Table 3.2. Tri-exponential fitting parameters of the TRPL decay for perovskite films on a bare PEN substrate. The perovskite layers were fabricated via the FGMSC system. Average lifetime (τ_{avg}) was calculated by $\tau_{avg} = \frac{\sum_i A_i \tau_i^2}{\sum_i A_i \tau_i}$, where A_i and τ_i are amplitude ratio and lifetime of each time-component, respectively	74
Table 3.3. Flexible perovskite solar cell performances. (average : 30 devices, active	

area : 0.078 cm ²).....	81
Table 3.4. Thickness of large-area (100 cm ²) perovskite layer at selected locations (A-H) under the coating speed of 225 mm/s with 3 cycles	90
Table 3.5. Photovoltaic parameters of large-area (100 cm ²) coated f-PSCs (64 sub-cells with the active area of 0.078 cm ²) and flexible perovskite solar mini-module with active area of 35.1 cm ²	91
Table 3.6. Photovoltaic parameters of 64 sub-cells with coating area of 100 cm ² . The perovskite layer was coated by the FGMSC system with coating speed of 225 mm/s with 3 cycles (active area of 0.078 cm ²).....	92
Table 4.1. Perovskite solar cell performances according to the coating method. The active area was 0.078 cm ²	121

List of Figures

Figure 1.1. Size distribution of the perovskite aerosol particles generated by the megasonic nebulizer. The geometric standard deviation (GSD) is given by $\exp\left(\sqrt{\sum n_j(\ln d_j - \ln d_g)^2/(N - 1)}\right)$, where d_j is the diameter of an individual particle, n_j is the number of particles in the j^{th} group, N is the total number of particles, and $\ln d_g$ is the natural logarithm of the geometric mean diameter (GMD) of the particles, defined as $\sum n_j \ln d_j / N$ 4

Figure 1.2. Schematic illustrations of coating mechanisms; (a) meniscus-assisted-coating and (b) spray-coating7

Figure 1.3. Contact angles of perovskite solution dropped on (a) glass/ITO, (b) PEN/ITO, (c) glass/ITO/PTAA and (d) PEN/ITO/PTAA substrates8

Figure 2.1. Size distribution of the perovskite aerosol particles generated by the megasonic nebulizer. The geometric standard deviation (GSD) is given by $\exp\left(\sqrt{\sum n_j(\ln d_j - \ln d_g)^2/(N - 1)}\right)$, where d_j is the diameter of an individual particle, n_j is the number of particles in the j^{th} group, N is the total number of particles, and $\ln d_g$ is the natural logarithm of the geometric mean diameter (GMD) of the particles, defined as $\sum n_j \ln d_j / N$ 20

Figure 2.2. Schematic illustration of an inverted planar MAPbI₃ perovskite solar cell fabricated via the megasonic-spray coating system21

Figure 2.3. Schematic representation of the megasonic-spray coating process ...23

Figure 2.4. Surface and FIB-cross-section SEM micrographs of the perovskite film grown on glass/ITO/PEDOT:PSS with scan speed: (a, d) 10 mm/s, (b, e) 15 mm/s, and (c, f) 20 mm/s. The films were annealed at 120 °C for 1 min with DMSO vapor after coating and for 4 min in air26

Figure 2.5. (a) XRD patterns of megasonic coated perovskite films. (b) UV-vis spectra of perovskite films coated on bare glass27

Figure 2.6. (a) J - V characteristics of the best performing devices with three coating scan speeds. (b) Photovoltaic performance distribution of 21 samples with a coating scan speed of 15 mm/s. The photovoltaic characteristics are measured under 1 sun illumination (100 mW cm⁻², AM 1.5G) with a shading mask36

Figure 2.7. IPCE and integrate J_{SC} of the 15 mm/s device with an active area of 0.0754 cm² under 1 sun illumination. The range from 350 to 400 nm could be absorbed by glass and transparent conducting oxide layers, therefore, it leads to less effect on integrated J_{SC} 37

Figure 2.8. EIS Nyquist plots with fitted plots under 1 sun illumination for voltages in the range 0.8-0.6 V38

Figure 2.9. (a) Resistance of the SCs and (b) Resistance of the perovskite layer, measured under various bias voltages. The plotted values were obtained from EIS measurements under 100 mW/cm² of white LED with voltages in the range 0.8-0.6 V and fitted using the equivalent model circuit shown in the inset of (a). (c) TRPL spectra of megasonic-spray coated perovskite films as a function of the scan speed. The perovskite films were coated on a bare glass substrate and annealed at 120 °C for 1 min with DMSO vapor after coating and for 4 min in air39

Figure 2.10. Dark current density-voltage curves and carrier diffusion lengths of FTO/MAPbI ₃ /Au.....	40
Figure 2.11. Large-area (7.5 cm × 7.5 cm) perovskite layer coating using the megasonic-spray coating method.....	44
Figure 2.12. Schematic image of the active areas (1 cm ²) on the large-area electrodes	45
Figure 2.13. <i>J-V</i> curves and histogram (inset) of 18 megasonic sprayed perovskite solar cells with a 1 cm ² active area under 1 sun illumination.....	46
Figure 2.14. Stabilized photocurrent density (blue) and power conversion efficiency (red) measured at maximum power voltage of 0.76V for 200 seconds of the 15 mm/s device with an active area of 1 cm ² under 1 sun illumination	47
Figure 3.1. Schematic illustrations of coating mechanisms; (a) meniscus-assisted-coating and (b) spray-coating.....	61
Figure 3.2. Contact angles of perovskite solution dropped on (a) glass/ITO, (b) PEN/ITO, (c) glass/ITO/PTAA and (d) PEN/ITO/PTAA substrates	62
Figure 3.3. Size distribution of generated perovskite precursor droplets by the FGMSC system. The geometric standard deviation (GSD) is given by $\exp\left(\sqrt{\frac{\sum n_j(\ln d_j - \ln d_g)^2}{N - 1}}\right)$, where d_j is the diameter of an individual particle, n_j is the number of particles in the j^{th} group, N is the total number of particles, and $\ln d_g$ is the natural logarithm of the geometric mean diameter (GMD) of the particles, defined as $\sum n_j \ln d_j / N$	64
Figure 3.4. Illustrations of Film-Growth-Megasonic-Spray-Coating (FGMSC) system which is consisted of two main parts: droplet generation part (left)	

and motion control part (right)	65
Figure 3.5. Changes in (a) size distribution, (b) geometric mean diameter (GMD, red) and geometric standard deviation (GSD, blue) of the perovskite droplets over 30 min.....	66
Figure 3.6. (a) Perovskite film coverage and (b) grain size according to nozzle moving speed from 50 to 500 mm/s.....	69
Figure 3.7. (a) Perovskite film coverage and (b) grain size with respect to 1 to 6 coating cycles and nozzle moving speed from 75 to 450 mm/s. (c) Photograph of perovskite layer on PEN/ITO substrate. (d) Cross-section SEM images of perovskite layers at the coating speed of 75, 225 and 450 mm/s.....	75
Figure 3.8. The SEM images of perovskite surface with respect to multiple coatings under each nozzle speed.....	76
Figure 3.9. (a) TRPL spectra and (b) UV-Vis absorption spectra of the perovskite films coated on bare PEN substrates with respect to three coating conditions. (c) XRD patterns obtained from perovskite films coated on PEN/ITO substrates at three coating conditions. (110) peaks and FWHMs of the perovskite films in the inserted graph.....	77
Figure 3.10. (a) $J-V$ curves of the best performing sub-cells at three coating conditions. (b) EIS Nyquist plots of the f-PSCs at three coating conditions measured under bias voltage of 0.8 V, which is fitted by the equivalent circuit model (inset). (c) Efficiency distribution of 50 devices with a coating speed of 225 mm/s. (d) Normalized PCEs of f-PSCs after 1000 bending cycles and (e) photographs of f-PSCs under various bending radius ($R_b = \infty, 10, 8, 6, 4$ mm)	82

Figure 3.11. EIS Nyquist plots with fitted plots under coating speed of (a) 75, (b) 225 and (c) 450 mm/s for voltages in the range 0-0.8 V 83

Figure 3.12. Resistance of the perovskite layer of the f-PSCs, measured under various bias voltages. The plotted values were obtained from EIS measurements under 100 mW/cm² of white LED with voltages in the range 0-0.8 V..... 84

Figure 3.13. *J-V* characteristics of the best f-PSC fabricated by the FGMSC system with a coating speed of 225 mm/s (active area of 0.078 cm²)..... 85

Figure 3.14. (a) IPCE and integrated *J_{SC}* of the 225 mm/s device with an active area of 0.078 cm². (b) Stabilized photocurrent density (red) and PCE (blue) measured at maximum power voltage of 0.87 V for 600 seconds of the 225 mm/s device with an active area of 0.078 cm² 86

Figure 3.15. Normalized PCEs of the f-PSCs coated by the FGMSC system with a coating speed of 225 mm/s according to the bending cycles under various bending radius 87

Figure 3.16. (a) *J-V* curve of the best performing flexible perovskite sub-cell (active area of 0.078 cm²). (b) Photovoltaic performance distribution of 64 sub-cells. (c) Average PCEs of sub-cells at each location. (four sub-cells in each location) and photograph of large-area (100 cm²) flexible perovskite film (inset)..... 95

Figure 3.17. (a) Photograph of large-area (100 cm²) perovskite film coated by the FGMSC system. We selected eight locations diagonally in the coated substrate to identify uniformity of the film. (b) FIB-cross-sectional images of the perovskite film obtained from the selected locations..... 96

Figure 3.18. (a) Schematic of cross-section view and photograph of flexible

perovskite solar mini-module. (b) $I-V$ curves of flexible perovskite solar mini-module with active of 35.1 cm^2 . (c) Efficiency degradation tracking of the glass-to-glass encapsulated flexible perovskite solar mini-module under continuous 1-sun illumination. These devices are coated by the FGMSC system with coating speed of 225 mm/s 97

Figure 4.1. Atomic Force Microscopy height images of megasonic-spray coated PTAA films according to substrate temperature..... 114

Figure 4.2. Atomic Force Microscopy height images and of megasonic-spray coated PTAA films according to coating repetition. Temperatures of substrate are (a-c) $40 \text{ }^\circ\text{C}$ and (d-f) $70 \text{ }^\circ\text{C}$ 115

Figure 4.3. Atomic Force Microscopy height images of megasonic-spray coated PTAA films according to coating repetition at ambient conditions. The concentration of PTAA solution is 6 mg/ml 116

Figure 4.4. Atomic Force Microscopy height images of megasonic-spray coated PTAA films according to coating repetition at ambient conditions. The concentration of PTAA solution is 3 mg/ml 117

Figure 4.5. Atomic Force Microscopy height images of (a) bare ITO/Glass substrate and (b) spin-coated PTAA film 118

Figure 4.6. FIB-cross-section SEM images of (a) spin-coated PTAA film and (b-e) megasonic-spray coated PTAA films according to coating repetition at ambient conditions. The concentration of PTAA solution is 3 mg/ml 119

Figure 4.7. Schematic illustration of an inverted perovskite solar cell fabricated via megasonic-spray coating system 122

Figure 4.8. Box charts of performance parameters according to coating process of PTAA thin-film. The active area was 0.078 cm^2 123

Nomenclature

Alphabetical

PCE	Power conversion efficiency
PV	Photovoltaic
PSC	Perovskite solar cell
PSM	Perovskite solar module
f-PSC	Flexible perovskite solar cell
f-PSM	Flexible perovskite solar module
CTL	Charge transport layer
HTL	Hole transport layer
ETL	Electron transport layer
TCO	Transparent conductive oxide
MAC	Meniscus-assisted-coating
DC	Droplet coating
FC	Film coating
J-V	Current density-voltage
J_{SC}	Short circuit current density
I_{SC}	Photocurrent
V_{OC}	Open circuit voltage
FF	Fill factor
R_S	Series resistance
SCs	Selective contacts
R_{SC}	Resistance of selective contact

C_{SC}	Capacitance of selective contact
R_{rec}	Recombination resistance of perovskite layer
C_{PS}	Capacitance of perovskite layer
GSD	Geometric standard deviation
GMD	Geometric mean diameter
d_j	Diameter of an individual particle
d_g	Grain size
R_b	Bending radius
n_j	Number of particles
N	Total number of particles
$\ln d_g$	Natural logarithm of the geometric mean diameter
L_d	Carrier diffusion length
k	Boltzmann constant
T	Temperature
RMS	Root mean square

Greek letters

γ	Surface tension of precursor
ρ	Density of precursor
f	Frequency of ultrasonic transducer, or frequency of vibrator
τ	Lifetime
μ	Carrier mobility
ε	Dielectric constant of perovskite
ε_0	Absolute permittivity (dielectric constant of vacuum)

Chapter 1. Introduction

1.1. Background

The rapid increase in efficiency of thin-film solar cells based on organometallic halide perovskites makes them highly promising candidates for the development of new photovoltaic devices for solar energy conversion [1-6]. Furthermore, the demand for flexible perovskite solar cells has also increased due to their numerous applications. [7-11] In line with this trend, it is clear that the path towards the commercialization of solution-processed perovskite solar cells requires the development of automated and scalable fabrication methods for linear coating techniques, such as roll-to-roll and sheet-fed processing rather than spin coatings that have been used mostly in laboratory.

1.1.1 Demand for the Megasonic-Spray Coating System

Spraying, a widely used technique in industrial processes, offers a number of advantages over spin coating, including the extendibility to the continuous fabrication of modules with large areas and reduced materials consumption. [12] Spray-deposited perovskite solar cells (PSCs) have been fabricated using ultrasonic-spray coating utilizing frequency of 35 kHz [13] and 120 kHz [14] (average PCE 14.1% [15]), electrospray coating (average PCE 11.7% [16]), and pneumatic-spray coating (average PCE 16.1% [17]). Generally, the mean droplet size produced by an ultrasonic nebulizer is expressed by Lang's equation:

$$d_d = 0.34 \left(\frac{8\pi\gamma}{\rho f^2} \right)^{1/3} \quad (1)$$

Where γ , ρ , and f are the surface tension of precursor (γ , N s/m²), density of precursor (ρ , kg/m³) and frequency of ultrasonic transducer (f , Hz) [18], respectively. Typical ultrasonic-spray methods which use under 1MHz frequency generate over 10 μm droplets and have broad size distribution [19]. Smaller droplets with a narrower size distribution are desirable to fabricate uniform coating [16]. Megasonic-spray uses a high-frequency (1.7 MHz) from a submerged transducer in contrast to the conventional ultrasonic-sprays that usually use under 1 MHz. Therefore, there is a possibility that can generate more homogeneous and smaller droplets with sizes of 2-4 μm and geometric standard deviation of 1.4 (**Figure 1.1**) than conventional ultrasonic-spray methods which have 1.8 geometric standard deviation [19]. Perovskite films obtained using megasonic-spray coating could exhibit high uniformity in large

areas, owing to the even size of the droplets. However, the megasonic-spray coating has not been studied for the fabrication of perovskite solar cells.

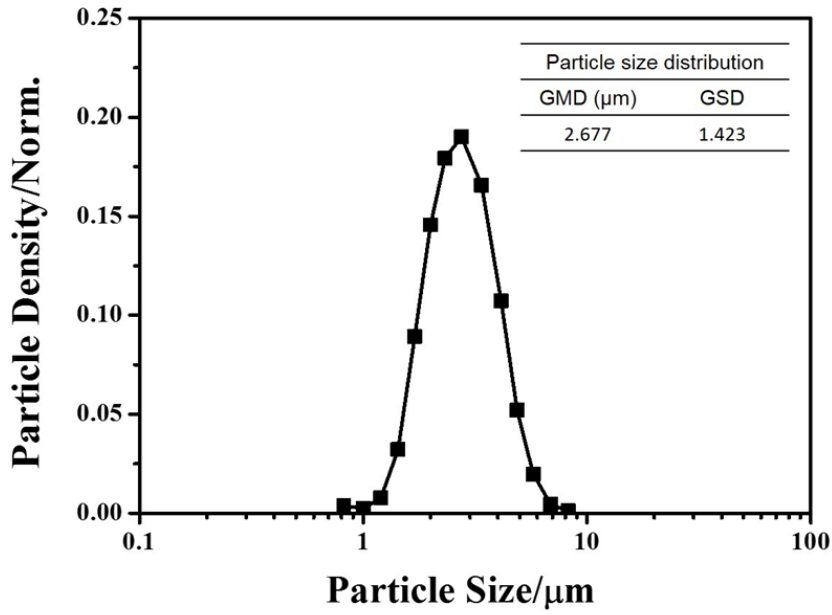


Figure 1.1. Size distribution of the perovskite aerosol particles generated by the megasonic nebulizer. The geometric standard deviation (GSD) is given by $\exp\left(\sqrt{\frac{\sum n_j (\ln d_j - \ln d_g)^2}{N - 1}}\right)$, where d_j is the diameter of an individual particle, n_j is the number of particles in the j^{th} group, N is the total number of particles, and $\ln d_g$ is the natural logarithm of the geometric mean diameter (GMD) of the particles, defined as $\sum n_j \ln d_j / N$.

1.1.2. Demand for the Film-Growth-Megasonic-Spray-Coating System

In automated scalable coating techniques, meniscus-assisted-coating (MAC) methods (e.g. slot-die-coating, bar-coating, etc.) exhibit the most remarkable coating performance on glass-based substrates with high PCEs over 20%. [20-24] However, the methods have not been considerably improved in terms of the flexible perovskite solar cells (f-PSCs) production compared to the glass-based PSCs due to the fundamental limitation between their coating principle and substrate wettability. [25-27] As suggested in **Figure 1.2a**, the main principle of the MAC techniques is to maintain uniform perovskite wet-film during crystallization by balancing the surface tension of perovskite precursor solution and the wettability between the substrate and the solution. [28-30] This principle is well applied on the glass-based hydrophilic substrates. However, conventional flexible-electrode-substrates, such as indium tin oxide (ITO) coated polyethylene naphthalate (PEN) and polyethylene terephthalate (PET) films, have much higher contact-angles (equals to hydrophobic surface) than commercial ITO coated glass (glass/ITO) substrates have, even with additional coating of a hole transporting layer (poly(triaryl amine), or PTAA), as shown in **Figure 1.3**. Then, maintaining the wet-film crystallization is a challenging task because of significant coverage reduction during coating and solvent evaporation (**Figure 1.2a-2**) when the MAC methods are applied to scalable coating on the flexible substrates. [28-30] Therefore, a new scalable coating method is necessary to achieve high quality film on the flexible substrates.

Spray-coating technique is one of the promising scalable coating methods for fabricating high quality perovskite film. The method generates fine precursor droplets from a precursor solution and transfers them to substrates. Theoretically, the

fine perovskite precursor droplets, not the wet-film, lead to much faster evaporation of solvent on the heated substrates due to their extremely small volume even without assisted treatment such as anti-solvent, air-knife, etc. [16, 31, 32] Therefore, there is little coverage reduction of the deposited droplets during coating and solvent evaporation, which facilitates the fabrication of defect-free, uniform perovskite film (**Figure 1.2b-3**) on unfavorable substrates. Noting this advantage, many researchers have reported the fabrication of perovskite films that utilize the spray method by taking advantages of its fine droplet size [16, 31], droplet size control [16], detailed thickness control [31], high material utilization, and automation properties. They have mainly endeavored to obtain high efficiency and stable unit cells on glass substrates. [16, 17, 31-35] Among this was our previous work which showed that the scalability can be easily achieved by using ultra-fine perovskite droplets. [31] In these studies including ours, however, the fundamental understanding of perovskite film growth principles on the flexible substrate via spray-coating had been elusive and flexible perovskite solar module fabrication had not been fully demonstrated.

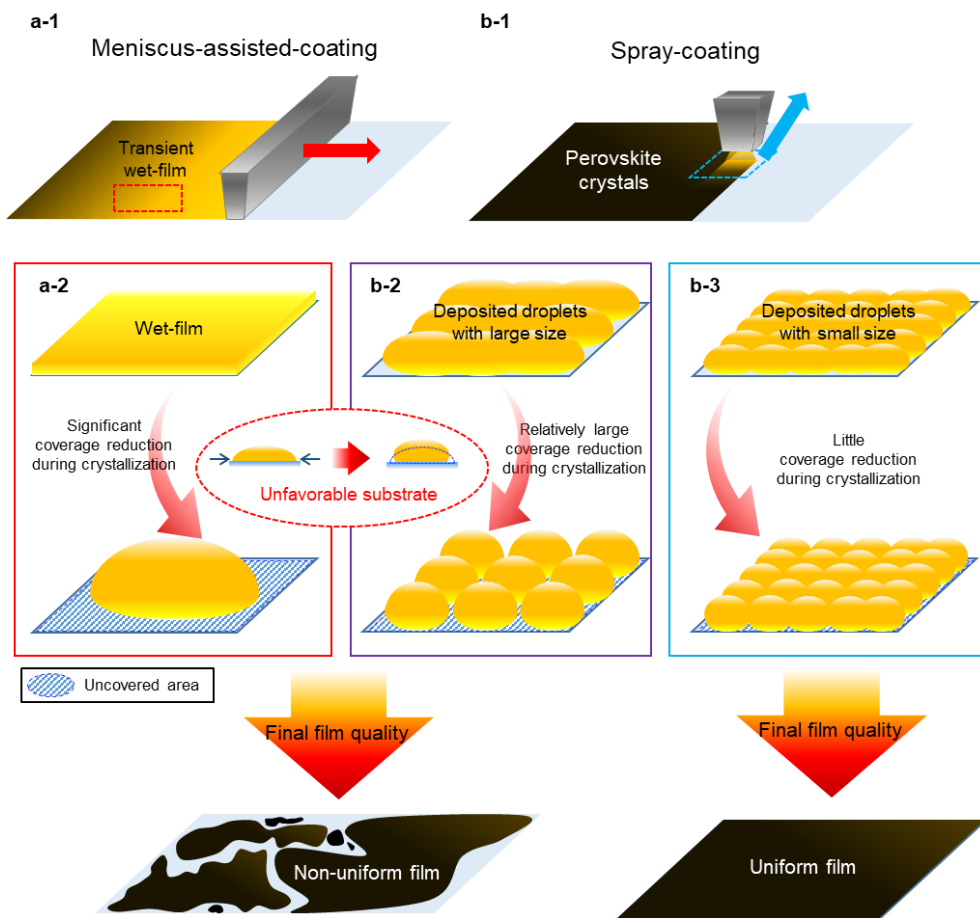


Figure 1.2. Schematic illustrations of coating mechanisms; (a) meniscus-assisted-coating and (b) spray-coating.

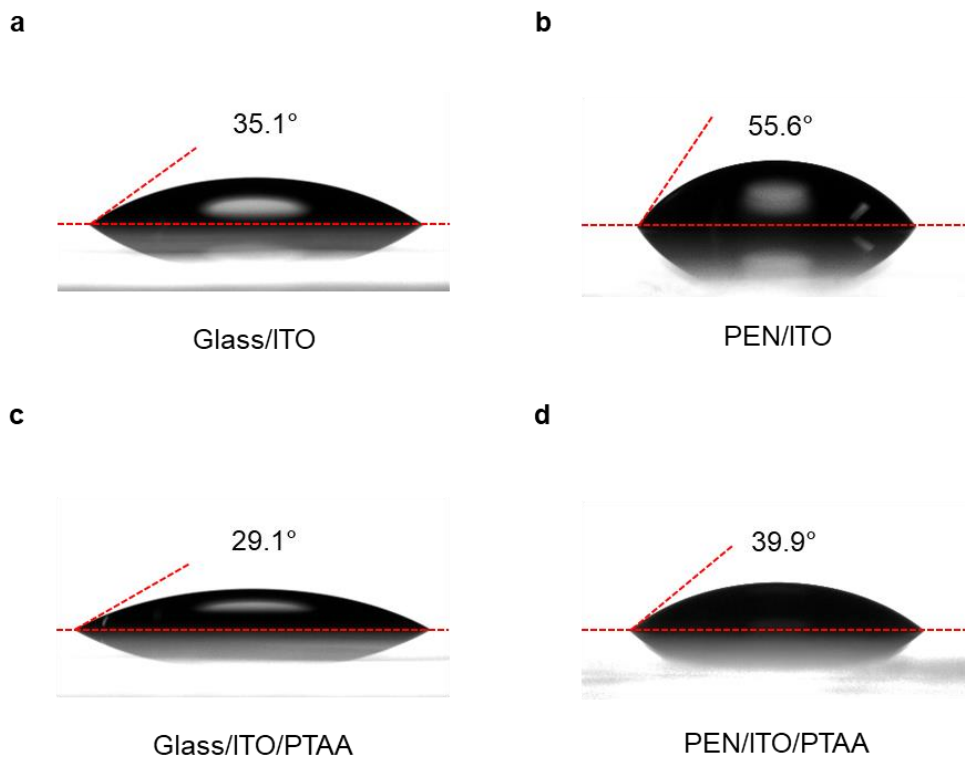


Figure 1.3. Contact angles of perovskite solution dropped on (a) glass/ITO, (b) PEN/ITO, (c) glass/ITO/PTAA and (d) PEN/ITO/PTAA substrates.

1.2. Research Objectives

This dissertation is directed to develop a new spray-coating method for scalable production of efficient perovskite solar cells. Moreover, we are directed to actualize a fully automated thin-film coating system which can continuously produce high performance flexible perovskite solar cells and modules with excellent reproducibility.

First, a simple, low-cost, large area and continuous scalable coating method is proposed for the fabrication of hybrid organic-inorganic perovskite solar cells. We developed a megasonic spray coating method utilizing 1.7 MHz megasonic nebulizer that could fabricate reproducible large-area planar efficient perovskite films. The coating method was shown to fabricate uniform large-area perovskite film with large-sized grain since smaller and narrower sized mist droplets could be generated by megasonic-spraying than those by existing ultrasonic-spray methods. We control the volume flow rate of the $\text{CH}_3\text{NH}_3\text{PbI}_3$ precursor solution and the reaction temperature, to obtain high quality perovskite active layer. Our devices reach a maximum efficiency of 16.9%, with an average efficiency of 16.4% from 21 samples. We also demonstrate the applicability of megasonic-spray coating to the fabrication of large-area solar cells (1 cm^2), with a power conversion efficiency of 14.2%.

Second, we have come up with a Film-Growth-Megasonic-Spray-Coating (FGMSC) method that continuously grows uniform perovskite film on large-area flexible substrates by using fine perovskite precursor droplets ($< 10 \text{ }\mu\text{m}$). The film growth mechanisms of a perovskite layer (e.g. film coverage, roughness, and crystal

grain size) according to the precursor droplet supply rate and the multiple spray was thoroughly investigated for manufacturing flexible perovskite solar mini-module. In complete automation that utilizes the two-dimensional transportation system, the FGMSC system has successfully fabricated a defect-free uniform perovskite layer on large-area flexible substrates with high reproducibility and flexibility by controlling perovskite film growth. The scalability of the system has also been validated in the fabrication of large area (100cm²) perovskite layer on a flexible substrate with uniform solar cells that have shown the average PCE of $17.47 \pm 0.22\%$ and flexible perovskite solar mini-module with PCE of 16.10% measured from an active area of 35.1 cm².

Third, we have applied the megasonic-spray coating method to the fabrication of PTAA layer which is used as a hole transport layer in inverted PSCs. Optimization of the spray-coating condition is successfully conducted by the AFM and FIB-SEM measurement. We have achieved effective PCEs comparable to those of spin-coated PTAA devices. These results clearly indicate that the megasonic-spray coating method can fabricate highly reproducible uniform films not only with the perovskite active layers but also with the charge transport layers that have a thickness of tens of nanometers. Our megasonic-spray coating system, therefore, is a highly practical, continuous fabrication technique for automated and scalable fabrication methods for linear coating techniques, such as roll-to-roll and sheet-fed processing.

1.3. Thesis Outline

This thesis is organized into five chapters. This chapter outlines overall introduction of this thesis.

Chapter 2 focused on the development of the megasonic-spray coating system for the continuous fabrication of hybrid organic-inorganic perovskite solar cells. Our method works at low temperature and in solvent-free conditions, and it can be used to create large-area perovskite films. The solar cells fabricated using our method achieve a maximum efficiency of 16.9 % with an average of 16.4 % of 21 samples. We also demonstrate the applicability of our megasonic-spray coating to the fabrication of large-area solar cells (1 cm²), with a power conversion efficiency of 14.2%. We believe that our study makes a significant contribution towards the commercialization of perovskite solar cells because the approach we propose is novel, highly tunable, and reproducible, and it can be used in industrial processes for the production of solar cells, including roll-to-roll processing.

Chapter 3 proposed the Film-Growth-Megasonic-Spray-Coating (FGMSC) system which is a scalable, continuous process that continuously grows uniform perovskite film on large-area flexible substrates. The fundamental principles of perovskite film growth mechanisms on the flexible substrate via spray-coating were thoroughly investigated. As a result, we have successfully fabricated defect-free uniform perovskite film on the flexible substrates with the FGMSC system. The scalability of this system is proved through fabrication of a flexible perovskite solar mini-module with PCE of 16.10% from an active area of 35.1 cm². These results prove that our FGMSC system is the automated, sustainable system that

continuously produces high-performance f-PSCs for its scalability and efficiency.

Chapter 4 deals with the fabrication of charge transport layer via megasonic-spray coating method. Through the optimization of both substrate temperature condition and multiple megasonic-spray coatings, we have successfully obtained PTAA films which have the same quality as the spin-coated films. These results suggest that the megasonics-spray coating technology is a highly practical, continuous coating process for production of photovoltaic applications.

Chapter 5 summarizes the work presented in this dissertation.

1.4. References

- [1] M. A. Green, A. Ho-Baillie, H. J. Snaith, *Nat. Photonics*, **2014**, *8*, 506-514.
- [2] W. S. Yang, J. H. Noh, N. J. Jeon, Y. C. Kim, S. Ryu, J. Seo, S. I. Seok, *Science*, **2015**, *348*, 1234-1237.
- [3] W. S. Yang, B.-W. Park, E. H. Jung, N. J. Jeon, Y. C. Kim, D. U. Lee, S. S. Shin, J. Seo, E. K. Kim, J. H. Noh, S. I. Seok, *Science*, **2017**, *356*, 1376-1379.
- [4] E. H. Jung, N. J. Jeon, E. Y. Park, C. S. Moon, T.-J. Shin, T. Y. Yang, J. H. Noh, J. Seo, *Nature*, **2019**, *567*, 511-515.
- [5] Q. Jiang, Y. Zhao, X. Zhang, X. Yang, Y. Chen, Z. Chu, Q. Ye, X. Li, Z. Yin, J. You, *Nat. Photonics*, **2019**, *13*, 460-466.
- [6] NREL chart, accessed: March 2022, <https://www.nrel.gov/pv/cell-efficiency.html>.
- [7] J. Yoon, H. Sung, G. Lee, W. Cho, N. Ahn, H. S. Jung, M. Choi, *Energy Environ. Sci.*, **2017**, *10*, 337-345.
- [8] J. Feng, X. Zhu, Z. Yang, X. Zhang, J. Niu, Z. Wang, S. Zuo, S. Priya, S. Liu, D. Yang, *Adv. Mater.*, **2018**, *30*, 1801418.
- [9] C. Wu, D. Wang, Y. Zhang, F. Gu, G. Liu, N. Zhu, W. Luo, D. Han, X. Guo, B. Qu, S. Wang, Z. Bian, Z. Chen, L. Xiao, *Adv. Funct. Mater.*, **2019**, *29*, 1902974.
- [10] G. Lee, M. Kim, Y. W. Choi, N. Ahn, J. Jang, J. Yoon, S. M. Kim, J.-G. Lee, D. Kang, H. S. Jung, M. Choi, *Energy Environ. Sci.*, **2019**, *12*, 3182-3191.
- [11] H. S. Jung, G. S. Han, N.-G. Park, M. J. Ko, *Joule*, **2019**, *3*, 1850-1880.

- [12] Z. Yang, S. Zhang, L. Li and W. Chen, *Journal of Materiomics*, **2017**, *3*, 231-244.
- [13] D. K. Mohamad, J. Griffin, C. Bracher, A. T. Barrows and D. G. Lidzey, *Advanced Energy Materials*, **2016**, *6*, 1600994.
- [14] S. Das, B. Yang, G. Gu, P. C. Joshi, I. N. Ivanov, C. M. Rouleau, T. Aytug, D. B. Geohegan and K. Xiao, *ACS Photonics*, **2015**, *2*, 680-686.
- [15] H. Huang, J. Shi, L. Zhu, D. Li, Y. Luo and Q. Meng, *Nano Energy*, **2016**, *27*, 352-358.
- [16] S. C. Hong, G. Lee, K. Ha, J. Yoon, N. Ahn, W. Cho, M. Park and M. Choi, *ACS applied materials & interfaces*, **2017**, *9*, 7879-7884.
- [17] J. H. Heo, M. H. Lee, M. H. Jang and S. H. Im, *Journal of Materials Chemistry A*, **2016**, *4*, 17636-17642.
- [18] W.-N. Wang, A. Purwanto, I. W. Lenggoro, K. Okuyama, H. Chang and H. D. Jang, *Industrial & Engineering Chemistry Research*, **2008**, *47*, 1650-1659.
- [19] S. Tsai, Y. Song, C. Tsai, C. Yang, W. Chiu and H. Lin, *Journal of materials science*, **2004**, *39*, 3647-3657.
- [20] M. He, B. Li, X. Cui, B. Jiang, Y. He, Y. Chen, D. O'Neil, P. Szymanski, M. A. El-Sayed, J. Huang, Z. Lin, *Nat. Commun.*, **2017**, *8*, 16045.
- [21] W.-Q. Wu, Z. Yang, P. N. Rudd, Y. Shao, X. Dai, H. Wei, J. Zhao, Y. Fang, Q. Wang, Y. Liu, Y. Deng, X. Xiao, Y. Feng, J. Huang, *Sci. Adv.*, **2019**, *5*, eaav8925.
- [22] H.-J. Kim, H.-S. Kim, N.-G. Park, *Adv. Energy Sustainability Res.*, **2021**, *2*, 2000051.
- [23] D.-K. Lee, K.-S. Lim, J.-W. Lee, N.-G. Park, *J. Mater. Chem. A*, **2021**, *9*,

3018-3028.

- [24] J. W. Yoo, J. Jang, U. Kim, Y. Lee, S.-G. Ji, E. Noh, S. Hong, M. Choi, S. I. Seok, *Joule*, **2021**, *5*, 2420-2436.
- [25] T. M. Schmidt, T. T. Larsen-Olsen, J. E. Carle, D. Angmo, F. C. Krebs, *Adv. Energy Mater.*, **2015**, *5*, 1500569. Y. Deng, X. Zheng, Y. Bai, Q. Wang, J. Zhao, J. Huang, *Nat. Energy*, **2018**, *3*, 560-566.
- [26] B. Dou, J. B. Whitaker, K. Bruening, D. T. Moore, L. M. Wheeler, J. Ryter, N. J. Breslin, J. J. Berry, S. M. Garner, F. S. Barnes, S. E. Shaheen, C. J. Tassone, K. Zhu, M. F. A. M. v. Hest, *ACS Energy Lett.*, **2018**, *3*, 2558-2565.
- [27] J.-E. Kim, S.-S. Kim, C. Zuo, M. Gao, D. Vak, D.-Y. Kim, *Adv. Funct. Mater.*, **2019**, *29*, 1809194.
- [28] Y. Deng, X. Zheng, Y. Bai, Q. Wang, J. Zhao, J. Huang, *Nat. Energy*, **2018**, *3*, 560-566.
- [29] X. Dai, Y. Deng, C. H. V. Brackle, J. Huang, *Int. J. Extrem. Manuf.*, **2019**, *1*, 022004.
- [30] M. Remeika, L. K. Ono, M. Maeda, Z. Hu, Y. Qi, *Org. Electron.*, **2018**, *54*, 72-79.
- [31] M. Park, W. Cho, G. Lee, S. C. Hong, M. Kim, J. Yoon, N. Ahn, M. Choi, *Small*, **2019**, *15*, 1804005.
- [32] S. Bag, J. R. Deneault, M. F. Durstock, *Adv. Energy Mater.*, **2017**, *7*, 1701151.
- [33] D. S. Lee, M. J. Ki, H. J. Lee, J. K. Park, S. Y. Hong, B. W. Kim, J. H. Heo, S. H. Im, *ACS Appl. Mater. Interfaces*, **2022**, *14*, 7926-7935.
- [34] J. E. Bishop, C. D. Read, J. A. Smith, T. J. Routledge, D. G. Lidzey, *Sci Rep*, **2020**, *10*, 6610.

- [35] J. E. Bishop, J. A. Smith, D. G. Lidzey, *ACS Appl. Mater. Interfaces*, **2020**, *12*, 48237-48245.

Chapter 2. Megasonic-Spray Coating System for Glass-Based Perovskite Solar Cells Fabrication

2.1. Introduction

The rapid increase in efficiency of thin-film solar cells based on organometallic halide perovskites makes them highly promising candidates for the development of new photovoltaic devices for solar energy conversion [1-6]. State-of-the-art devices achieve power conversion efficiencies (PCEs) over 22% [6], a value that is much higher than the record efficiencies of thin film silicon and organic semiconductor photovoltaics (PVs) [7]. It is clear that the path towards the commercialization of solution-processed perovskite solar cells requires the development of fabrication methods for linear coating techniques, such as roll-to-roll and sheet-fed processing rather than spin coatings that have been used mostly in laboratory. However, a few studies have appeared on scalable film-coating techniques that could be applied to the practical fabrication of large-size PSCs. Coating techniques like aerosol-spray [8-15], slot-die [16], inkjet printing [2], and blade coating [3, 5, 17, 18] were studied for the development of scalable techniques for coating perovskite thin films.

Spraying, a widely used technique in industrial processes, offers a number of advantages over spin coating, including the extendibility to the continuous

fabrication of modules with large areas and reduced materials consumption [19]. Spray-deposited PSCs have been fabricated using ultrasonic-spray coating utilizing frequency of 35 kHz [11] and 120 kHz [8] (average PCE 14.1% [14]), electrospray coating (average PCE 11.7% [10]), and pneumatic-spray coating (average PCE 16.1% [20]). Generally, the mean droplet size produced by an ultrasonic nebulizer is expressed by Lang's equation:

$$d_d = 0.34 \left(\frac{8\pi\gamma}{\rho f^2} \right)^{1/3} \quad (1)$$

Where γ , ρ , and f are the surface tension of precursor (γ , N s/m²), density of precursor (ρ , kg/m³) and frequency of ultrasonic transducer (f , Hz) [21], respectively. Typical ultrasonic-spray methods which use under 1MHz frequency generate over 10 μm droplets and have broad size distribution [22]. Smaller droplets with a narrower size distribution are desirable to fabricate uniform coating [10]. Megasonic-spray uses a low-intensity, high-frequency (1.7 MHz) from a submerged transducer in contrast to the conventional ultrasonic-sprays that usually use under 1 MHz. Therefore, there is a possibility that can generate more homogeneous and smaller droplets with sizes of 2-4 μm and geometric standard deviation of 1.4 (**Figure 2.1**) than conventional ultrasonic-spray methods which have 1.8 geometric standard deviation [22]. Perovskite films obtained using megasonic-spray coating could exhibit high uniformity in large areas, owing to the even size of the droplets.

However, the megasonic-spray coating has not been studied for the fabrication of perovskite solar cells. In this study we developed a continuous megasonic-spray coating that produces a narrower droplet size distribution and a smaller mean diameter than conventional ultrasonic-spray coating leading to the continuous fabrication of highly reproducible large-area perovskite solar cells. We

consider the common precursors PbI_2 and methyl ammonium iodide (MAI), and use them to obtain a highly uniform, pin-hole free perovskite coating layer with large grain sizes. We fabricate PSCs achieving PCEs of 16.5% (forward scan), 16.9% (reverse scan), and $16.4\% \pm 0.27\%$ (average over 21 samples) under 1 sun illumination condition, using an perovskite coating area of 56.25 cm^2 and an active area of 0.0754 cm^2 by using different mask aperture for Cu electrode. The schematic illustration of the device structure is shown in **Figure 2.2**. The best of average efficiencies of spray coated perovskite solar cells has been so far 16.1 % reported by Im group [20] in which they also reported the champion device efficiency 18.3 %. Furthermore, we find that increasing the single cell area to 1 cm^2 yields a maximum efficiency of 14.2% and an average efficiency of 13.7%, which is the record high efficiency for spray produced large area perovskite solar cells. Our megasonic-spray coating approach is therefore expected to be suitable for large-area continuous coating in PSCs, which makes it suitable for application in commercial roll-to-roll processing.

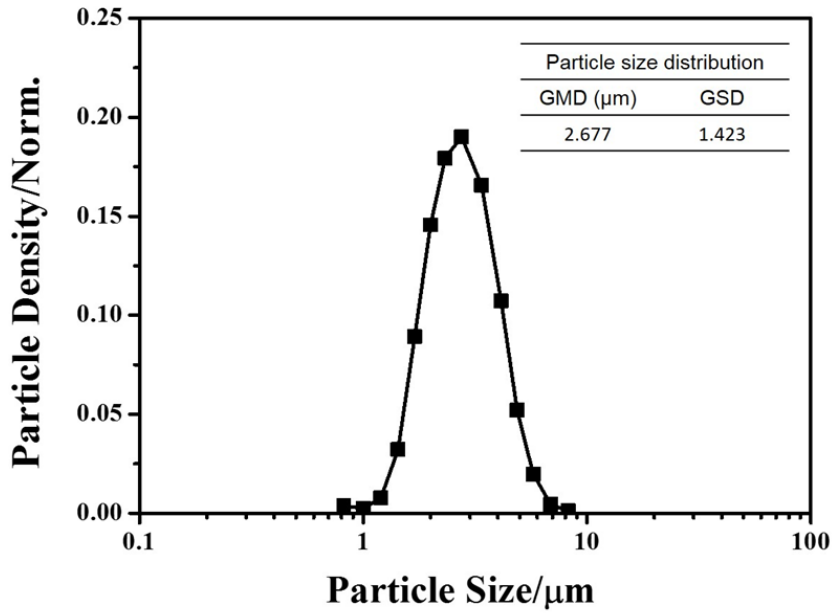


Figure 2.1. Size distribution of the perovskite aerosol particles generated by the megasonic nebulizer. The geometric standard deviation (GSD) is given by $\exp\left(\sqrt{\frac{\sum n_j (\ln d_j - \ln d_g)^2}{N - 1}}\right)$, where d_j is the diameter of an individual particle, n_j is the number of particles in the j^{th} group, N is the total number of particles, and $\ln d_g$ is the natural logarithm of the geometric mean diameter (GMD) of the particles, defined as $\sum n_j \ln d_j / N$.

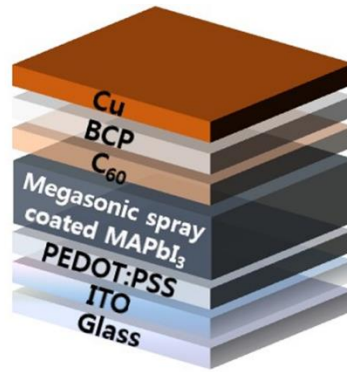


Figure 2.2. Schematic illustration of an inverted planar MAPbI₃ perovskite solar cell fabricated via the megasonic-spray coating system.

2.2 Results and Discussion

2.2.1. Design of Megasonic-Spray Coating Process

Figure 2.3 shows a schematic diagram of the megasonic nebulizer spray system that was used to coat the perovskite films. The system is composed of four main parts: (1) the megasonic nebulizer source (1.7 MHz, Busung Electronics), (2) the rectangular plastic nozzle (1 mm x 7 mm, Sang-A Pneumatic), (3) the motion stage (DST Robot), and (4) the mass flow controller (MFC, Bronkhorst High-Tech). The megasonic nebulizer source (1) generates micron sized aerosol droplets (2-4 μm) with a narrow size distribution. The aerosol is then mixed with the carrier gas (nitrogen) controlled by the MFC (4) and sprayed through the nozzle (2). The nozzle can be moved along the Y-axis. The substrates are mounted on the X-axis motion stages (3) as shown in **Figure 2.3**, and the temperature of the plate can be controlled. As the setup is fully automated, the spray operation can be accurately controlled, to obtain consistent and reliable coating on multiple devices and in different regions of the same device.

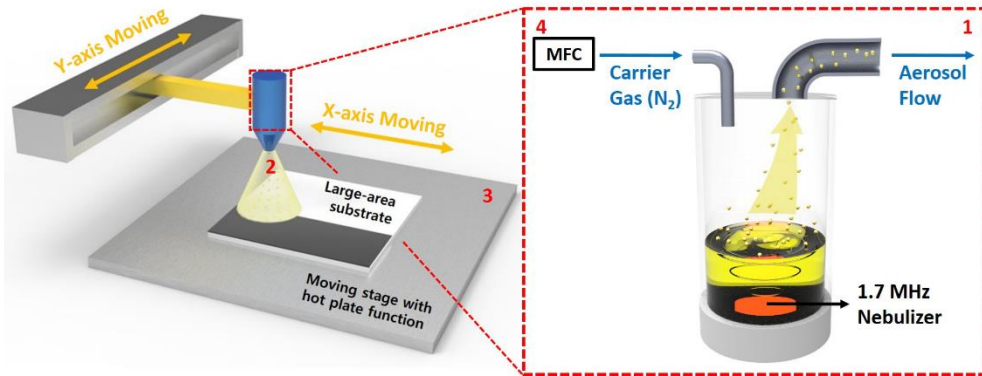


Figure 2.3. Schematic representation of the megasonic-spray coating process.

2.2.2. Investigation of Perovskite Films According to Supply Rate of Droplets

In the first stage of the coating process, a thin perovskite film is deposited onto a PEDOT:PSS-coated glass/ITO substrate using megasonic-spray coating, as described in the Experimental Section. In **Figure 2.4**, we show top-view and FIB cross-sectional SEM images of the perovskite films, obtained by setting the scan speed to 10, 15 and 20 mm/s. The top-view SEM images (**Figures 2.4a-c**) indicate that the morphology of the surface depends only slightly on the scan speed. All the films show similar morphologies, with differences in grain size of 350-900 nm. The largest grain size is obtained for the case of 15 mm/s scan speed. If the scan speed is too slow (in case of 10 mm/s scan speed), there may exist secondary nucleation on the already formed perovskite crystal [24]. These differences are related to the different number of droplets deposited per unit time. This indicates that there exists an optimum condition of the scan speed that would result in the high quality perovskite film and consequently high performance solar cell [25]. Cross-sectional SEM images of the complete device structure (ITO glass / PEDOT:PSS / MAPbI₃ / C60 / BCP / Cu) fabricated using FIB milling are shown in **Figures 2.4d-f**. The thickness of the perovskite films decreases linearly with the scan speed increasing. The top-view and cross-sectional images demonstrate that high quality, pinhole-free, and continuous perovskite films with large grains can be obtained using this method. The perovskite film with the larger grain sizes also shows improved crystallization, as confirmed by its XRD pattern (**Figure 2.5a**). XRD clearly indicates that the MAPbI₃ perovskite film formed by megasonic-spray coating has little or no impurities (e.g., PbI₂ at $2\theta = 13^\circ$). Sharp peaks, corresponding to the (100) and (200) planes, are observed at $2\theta = 14^\circ$ and $2\theta = 28.5^\circ$. The peak corresponding to the (110)

plane of the tetragonal lattice structure of the MAPbI₃ crystal ($2\theta = 20.5^\circ$) is very weak compared to the peaks corresponding to the (100) and (200) planes of the cubic structure [26]. This finding is important, because the crystal structure of MAPbI₃ is likely to affect the electronic properties of the material and to influence charge separation and transport.

Figure 2.5b shows the dependence of the optical absorption spectra of the samples of **Figure 2.4d-f** on the scan speed of the spray-coating. A decrease in absorption density is observed as the scan speed increases, owing to the change of the perovskite film thickness. (The thickness of the perovskite layers vary 400, 790 and 940 nm when scan speed is 20, 15, and 10 mm/s, respectively (**Figure 2.4**)) The optical absorption results are consistent with the film thickness data shown in **Figure 2.4d-f** [27].

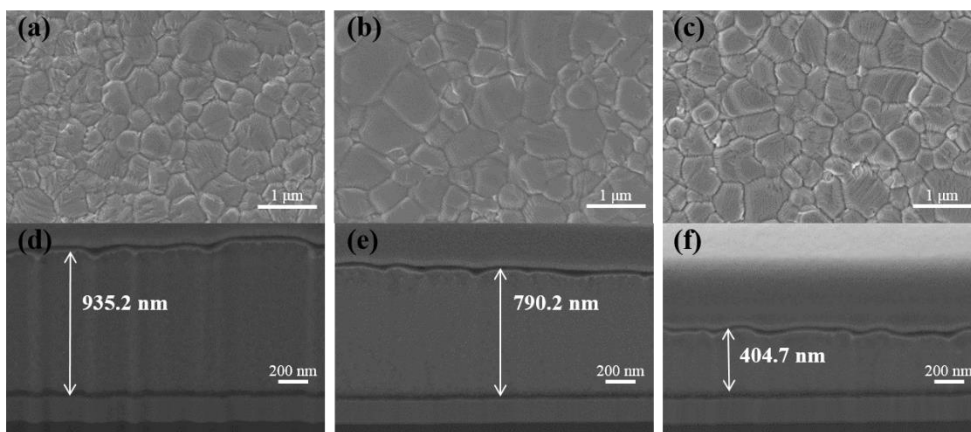


Figure 2.4. Surface and FIB-cross-section SEM micrographs of the perovskite film grown on glass/ITO/PEDOT:PSS with scan speed: (a, d) 10 mm/s, (b, e) 15 mm/s, and (c, f) 20 mm/s. The films were annealed at 120 °C for 1 min with DMSO vapor after coating and for 4 min in air.

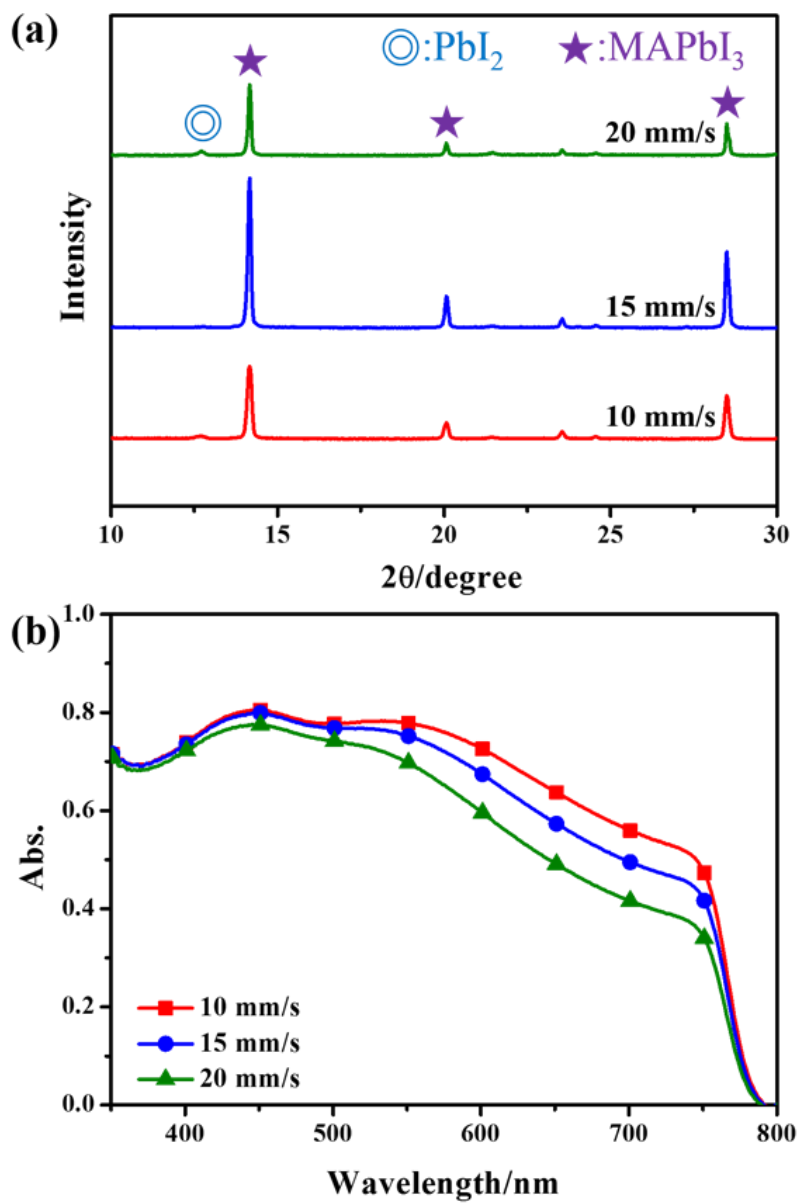


Figure 2.5. (a) XRD patterns of megasonic coated perovskite films. (b) UV-vis spectra of perovskite films coated on bare glass.

2.2.3. Fabrication of PSCs and Device Characteristics

We compared photovoltaic performance of three devices with different perovskite film thickness. As the perovskite film thickness increases, the short circuit current density (J_{SC}) are enhanced due to augmented photonic absorption (**Figure 2.6** and **Figure 2.5b**). A small change in J_{SC} is due to the J_{SC} have already reached almost maximum photocurrent density of MAPbI₃ based perovskite solar cell (~22.61 mAcm⁻²). [28] Because the fabricated perovskite films have enough thickness (400-900 nm) to absorb incident light. However, the open-circuit voltage (V_{OC}) is the highest in the case of 15 mm/s scan speed (790 nm thickness). The result is attributed to the largest grain size among three perovskite layers as can be found in **Figure 2.4**. (We discuss in detail below). As a result, the 790 nm thick perovskite layer shows the best PCE among three devices in our megasonic system as shown in **Figure 2.6**, which is relatively thicker than conventional optimized thickness of spin-coated perovskite layer (about 500-600 nm). [29, 30] Such results are consistent with other results of spraying-based perovskite solar cells, which might be due to larger grain size and different film density. [20, 25] Notably, in our systems, quite large grains of our megasonic-sprayed perovskite layer at scan speed of 15 mm/s lead to slow electron recombination rate (shown later), which finally show quite high V_{OC} in spite of its thick perovskite layer. As a consequence of optimization, we obtained the best PCE of 16.9% for the device fabricated at the 15 mm/s scan speed. The incident-photon-to-current efficiency (IPCE) of the best device is shown in **Figure 2.7**, along with the integrated current density, as a function of wavelength. The integrated short-circuit current density (J_{SC}) is 19.6 mA cm⁻¹, which is consistent with the measured J_{SC} .

To ensure the reproducibility of the results, 21 devices were fabricated and tested, with an optimized perovskite thickness of around 800 nm (**Table 2.1**). Histograms of the cell-performance characteristics are shown in **Figure 2.6b**, which demonstrate that all devices performed well. The V_{OC} values were highly reproducible and approaching 1.0 V, and the average J_{SC} was 21.3 mA cm⁻². As mentioned above, quite high V_{OC} values are originated from large grain size of MAPbI₃ coated with megasonic-spraying system even with an inverted structure with PEDOT:PSS. In addition, there are several previous reports which have V_{OC} values of over 1.0 V with inverted structure employing PEDOT:PSS [33-35]. Combined with the very good fill factors (nearly 80%), this gave an average PCE of 16.4% from 21 samples. These values are the highest average efficiency in those of other spray coated perovskite solar cells. [8, 10, 13, 20]

To obtain a deeper insight into the role of selective contact in the performance of PSCs, we have characterized the different samples using electrochemical impedance spectroscopy (EIS). We use the bias range of 0.8 to 0.6 V for observing the electron transfer kinetics nearby maximum power point for analysis in the real field operation conditions [36, 37]. **Figure 2.8** shows the Nyquist plots of PSCs at bias values of 0.8-0.6 V under 1 sun illumination. The inset in **Figure 2.9a** is the equivalent circuit employed to fit the spectra [38]. In the equivalent circuit, a series resistance (R_s) is used to model the interface resistance of the ITO substrate, and the interface of the selective contacts (SCs) with the perovskite layer are represented by the SC resistance (R_{SC}) and SC capacitance (C_{SC}) components. [19, 27, 39] R_{rec} and C_{ps} are the recombination resistance and the perovskite layer capacitance, respectively. [40] R_{SC} is the resistance associated with the high-frequency features in the Nyquist plots (**Figure 2.8**). The SC resistance

significantly affects the transport resistance at the selector layer, the charge-transfer rate at the interface (which can affect the bulk carrier density and, consequently, the bulk recombination), and the surface recombination at the SC interface. As shown in **Figure 2.9a**, the large R_{SC} in the 15 mm/s devices is likely to be caused by a reduced interface recombination.

Recombination processes in bulk perovskites are observed in the low-frequency region of the Nyquist plots of PSCs (**Figure 2.8**). [39] As shown in **Figure 2.9b**, R_{rec} increases for scan speeds along the series of 20, 10 and 15 mm/s. This large dependence of the recombination rate on the scan speed is related to the thickness and quality of the films. [41, 42] The value of R_{rec} for the 15 mm/s device is almost one order of magnitude larger than that of the other devices. Since recombination rate is inversely proportional to R_{rec} , the V_{OC} of 15mm/s is much higher than that of other devices due to optimum thickness.

To further investigate the dependence of the electron recombination rate on the scan speed, TRPL decay profiles were measured. The TRPL decay measurement was carried out for the Glass/MAPbI₃ films, and the data is shown in **Figure 2.9c**. A similar trend with the V_{OC} (**Table 2.2**) is observed in the TRPL response. Using a convolution of the TRPL decay with a third-order exponential function, we determine an average PL lifetime (τ_{avg}) for the 15 mm/s device (471.3 ns), which is much longer than that of the 10 and 20 mm/s ones (294.7 and 272.4 ns, respectively), as listed in **Table 2.3**. This indicates that the electron recombination rate of the 15 mm/s film is more efficiently suppressed than that of the 10 and 20 mm/s perovskite layers, owing to the better film quality [43]. As the slow component (τ_3) is related to the recombination, this suggests that the 10 and 20 mm/s coated layers contain more defects than the 15 mm/s film [44, 45]. By TRPL results, we conclude that the film

coated at a scan speed of 15 mm/s shows a slower PL decay rate, which are related to a lower density of defects [46]. Therefore, the 15 mm/s perovskite film has a high electron transport rate and a low carrier recombination rate compared to the other films. Furthermore, we calculated the carrier diffusion lengths using SCLC (Space-Charge-Limited-Current) method (**Figure 2.10**). As can be seen in **Table 2.4**, the perovskite film fabricated at 15 mm/s scan speed shows the longest diffusion length (256 nm) among three conditions, which means that photo-generated carrier can sufficiently diffuse in the device and transfer into charge transporting layers. Although 10 mm/s scan speed showed higher mobility than 15 mm/s scan speed, its diffusion length is shorter than the case of 15 mm/s scan speed due to short carrier lifetime. Consequently, its photovoltaic performance presented lower efficiency than the case of 15 mm/s scan speed. These results are consistent with performance results in **Table 2.2**. In the case of 20 mm/s scan speed which have low carrier mobility and short lifetime, it showed the smallest diffusion length and correspondingly the worst performance among three devices.

Cell#	V_{oc}/V	$J_{sc}/mAcm^{-2}$	FF	Eff./%
1	1.02	21.2	0.78	16.8
2	1.02	20.3	0.78	16.1
3	1.02	20.8	0.78	16.5
4	1.01	21.8	0.77	16.8
5	1.01	21.5	0.75	16.4
6	1.01	21.3	0.77	16.4
7	1.03	20.3	0.77	16.1
8	1.01	21.1	0.76	16.3
9	1.01	21.5	0.76	16.5
10	1.00	21.6	0.75	16.3
11	1.00	21.4	0.75	16.0
12	1.00	21.4	0.75	16.1
13	0.99	21.5	0.76	16.1
14	0.99	21.3	0.76	16.0
15	1.03	21.6	0.76	16.9
16	1.02	21.5	0.75	16.3
17	1.02	21.5	0.76	16.5
18	1.02	21.5	0.75	16.5
19	1.03	21.2	0.76	16.6
20	1.01	21.4	0.76	16.4
21	1.01	21.0	0.76	16.0
Average	1.01±0.01	21.3±0.4	0.76±0.01	16.4±0.3

Table 2.1. Photovoltaic parameters of 15 mm/s devices with and active area of 0.0754 cm² under 1 sun illumination.

	V_{oc}/V	$J_{sc}/mAcm^{-2}$	FF	Eff./%
10 mm/s	0.97	22.0	0.76	16.3
15 mm/s	1.03	21.6	0.76	16.9
20 mm/s	0.93	21.3	0.77	15.4
15 mm/s (avg.)	1.01±0.01	21.3±0.4	0.76±0.01	16.4±0.3

Table 2.2. Maximum photovoltaic parameters of perovskite solar cells at different megasonic-spray coating scan speeds. The last line reports averages over 21 devices with a scan speed of 15 mm/s. The active area was 0.0754 cm².

	$A_1/\%$	τ_1/ns	$A_2/\%$	τ_2/ns	$A_3/\%$	τ_3/ns	$\tau_{\text{avg}}/\text{ns}$
10 mm/s	31.09	2.21	8.60	54.2	60.31	302.0	294.7
15 mm/s	12.38	4.44	7.18	92.4	80.44	478.5	471.3
20 mm/s	24.95	3.90	11.71	64.6	63.34	282.7	272.4

Average lifetime (τ_{avg}) was calculated by $\tau_{\text{avg}} = \frac{\sum_i A_i \tau_i^2}{\sum_i A_i \tau_i}$. A_i and τ_i are amplitude ratios and lifetimes of each time components.

Table 2.3. Tri-exponential fitting parameters of the TRPL decay for the megasonic-spray coated perovskite films on a bare glass substrate.

	Perovskite film thickness (L)/nm	Mobility (μ)/cm ² V ⁻¹ s ⁻¹	τ_{avg} /ns	Diffusion length (L_d)/nm
10 mm/s	935	0.0714	294.7	233
15 mm/s	790	0.0537	471.3	256
20 mm/s	405	0.0053	272.4	61

Carrier diffusion length was calculated using the equation of $L_d = \sqrt{(kT\mu/e)\tau_{avg}}$, where k is Boltzmann constant, T is temperature, μ is carrier mobility, and τ_{avg} is average carrier lifetime from the TRPL measurement (Table S1). Mobility (μ) was estimated using Mott-Gurney law $J_D = (9\varepsilon\varepsilon_0\mu V^2)/8L^3$ from the SCLC (Space-Charge-Limited-Current) method, where ε and ε_0 are dielectric constants of perovskite [47-49] and vacuum permittivity, respectively, V is applied voltage and L is the perovskite film thickness. The observed response was analyzed according to SCLC theory [50-53].

Table 2.4. The calculated mobility, average lifetime and diffusion length of spray coated perovskite films.

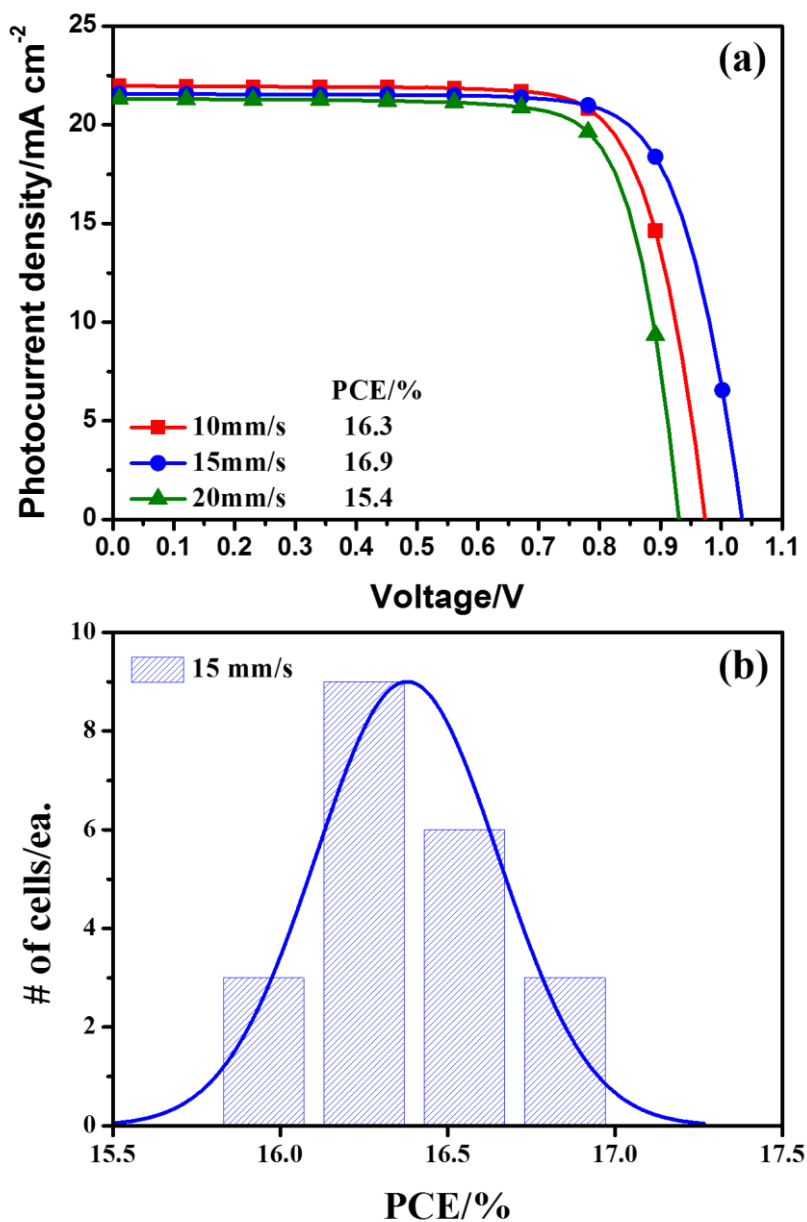


Figure 2.6. (a) J - V characteristics of the best performing devices with three coating scan speeds. (b) Photovoltaic performance distribution of 21 samples with a coating scan speed of 15 mm/s. The photovoltaic characteristics are measured under 1 sun illumination (100 mW cm^{-2} , AM 1.5G) with a shading mask.

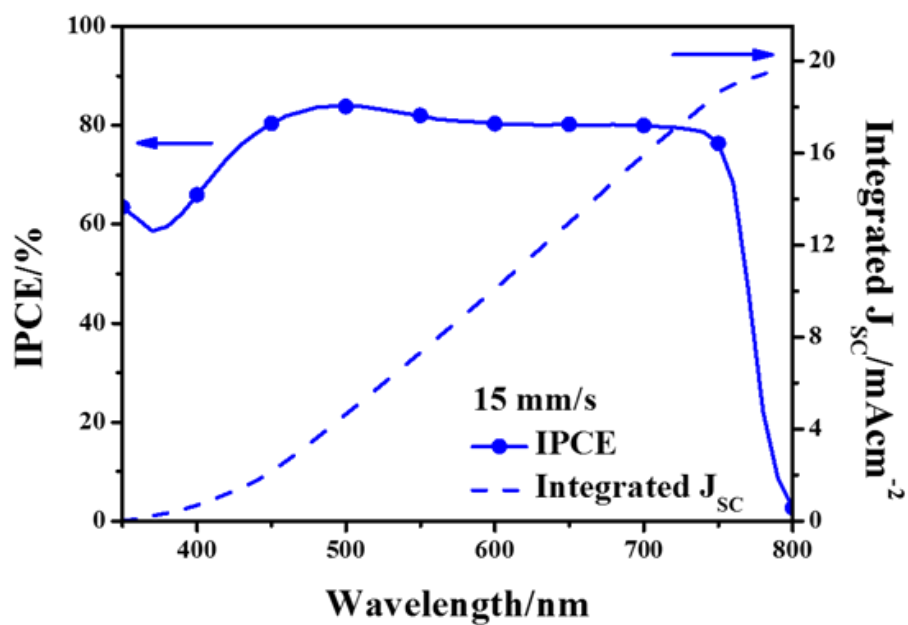


Figure 2.7. IPCE and integrate J_{sc} of the 15 mm/s device with an active area of 0.0754 cm^2 under 1 sun illumination. The range from 350 to 400 nm could be absorbed by glass and transparent conducting oxide layers, therefore, it leads to less effect on integrated J_{sc} . [31, 32]

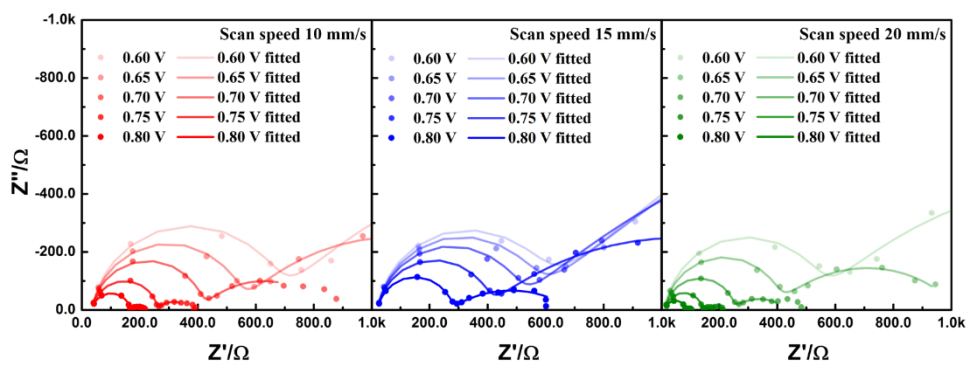


Figure 2.8. EIS Nyquist plots with fitted plots under 1 sun illumination for voltages in the range 0.8-0.6 V.

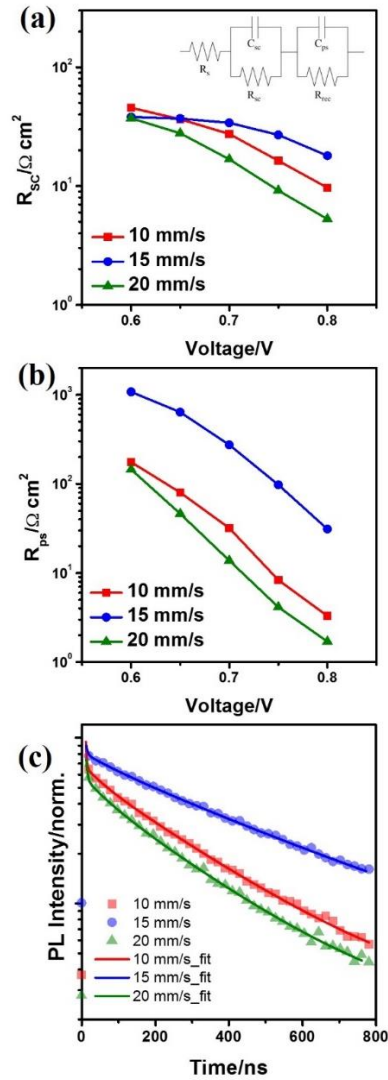


Figure 2.9. (a) Resistance of the SCs and (b) Resistance of the perovskite layer, measured under various bias voltages. The plotted values were obtained from EIS measurements under 100 mW/cm^2 of white LED with voltages in the range $0.8\text{-}0.6 \text{ V}$ and fitted using the equivalent model circuit shown in the inset of (a). (c) TRPL spectra of megasonic-spray coated perovskite films as a function of the scan speed. The perovskite films were coated on a bare glass substrate and annealed at $120 \text{ }^\circ\text{C}$ for 1 min with DMSO vapor after coating and for 4 min in air.

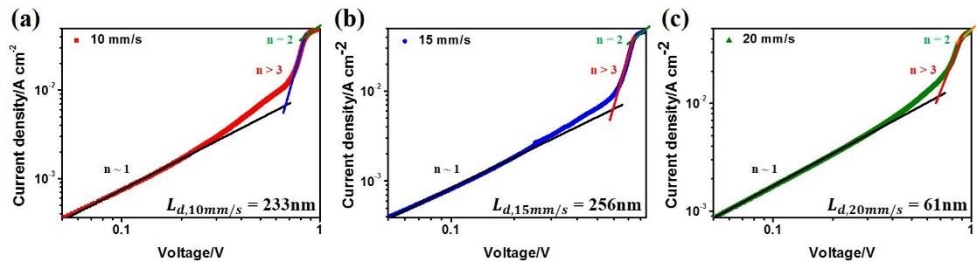


Figure 2.10. Dark current density-voltage curves and carrier diffusion lengths of FTO/MAPbI₃/Au.

2.2.4. Scalability of Megasonic-Spray Coating Process

Based on the above results and considerations, we coated 56.25 cm² of perovskite film (coating area, **Figure 2.11**) first and then made 18 sub-cells with active areas of 1cm² by using different mask aperture for Cu electrode deposition (**Figure 2.12**). **Figure 2.13** shows the best J - V curves with forward and reverse scans within this cells and a histogram (inset) obtained from 18 megasonic-spray coated cells under 1 sun conditions. We obtained the following photovoltaic performance parameters (without hysteresis, **Table 2.5**): $J_{SC} = 21.2 \text{ mA cm}^{-2}$, $V_{OC} = 1.03 \text{ V}$, FF = 0.65, and PCE = 14.2%. As far as we know, our study is the record high efficient large perovskite solar cell made by spray-coating. [14] The average PCE of the 18 devices is $13.7 \pm 0.3\%$ in reverse scan in **Table 2.6**. The stabilized steady-state J_{SC} and PCE are shown in **Figure 2.14**. This result confirms the applicability of our method to scalable linear coating techniques, like roll-to-roll fabrication.

Scan	V_{oc}/V	$J_{sc}/mAcm^{-2}$	FF	Eff./%
Reverse (Best)	1.03	21.2	0.65	14.2
Forward (Best)	1.01	21.3	0.65	14.1

Table 2.5. The photovoltaic performance parameters from reverse and forward scan of the best large (1 cm²) perovskite solar cells obtained with a megasonic-spray coating scan speed of 15 mm/s.

Cell#	V_{oc}/V	$J_{sc}/mAcm^{-2}$	FF	Eff./%
1	1.02	19.6	0.68	13.5
2	1.02	19.3	0.71	14.0
3	1.03	18.4	0.74	14.1
4	1.03	21.2	0.65	14.2
5	1.03	21.0	0.64	13.8
6	1.00	21.8	0.62	13.5
7	1.01	21.6	0.62	13.5
8	1.03	20.3	0.67	14.0
9	1.02	19.9	0.68	13.9
10	1.03	19.9	0.68	13.9
11	1.03	20.0	0.67	13.8
12	1.03	20.0	0.66	13.6
13	1.02	19.9	0.67	13.5
14	1.02	20.2	0.66	13.8
15	1.03	19.9	0.66	13.6
16	1.03	20.1	0.65	13.4
17	1.02	19.9	0.66	13.4
18	1.03	19.9	0.65	13.2
Average	1.02±0.01	20.2±0.8	0.67±0.03	13.7±0.3

Table 2.6. Photovoltaic parameters of 15 mm/s devices with and active area of 1 cm² under 1 sun illumination.

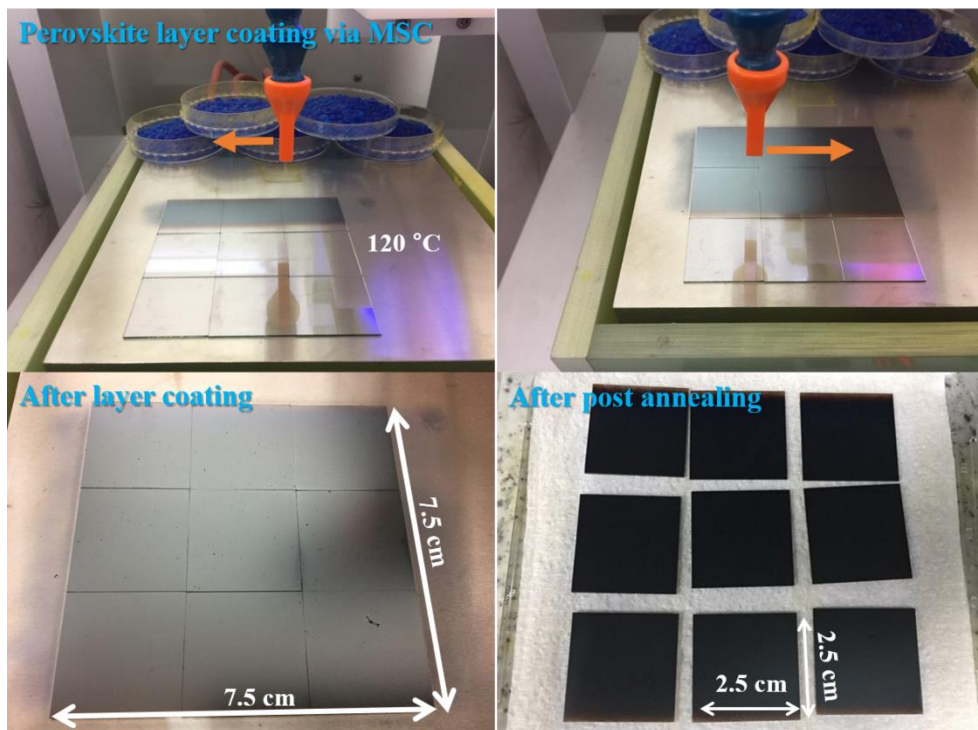


Figure 2.11. Large-area (7.5 cm × 7.5 cm) perovskite layer coating using the megasonic-spray coating method.

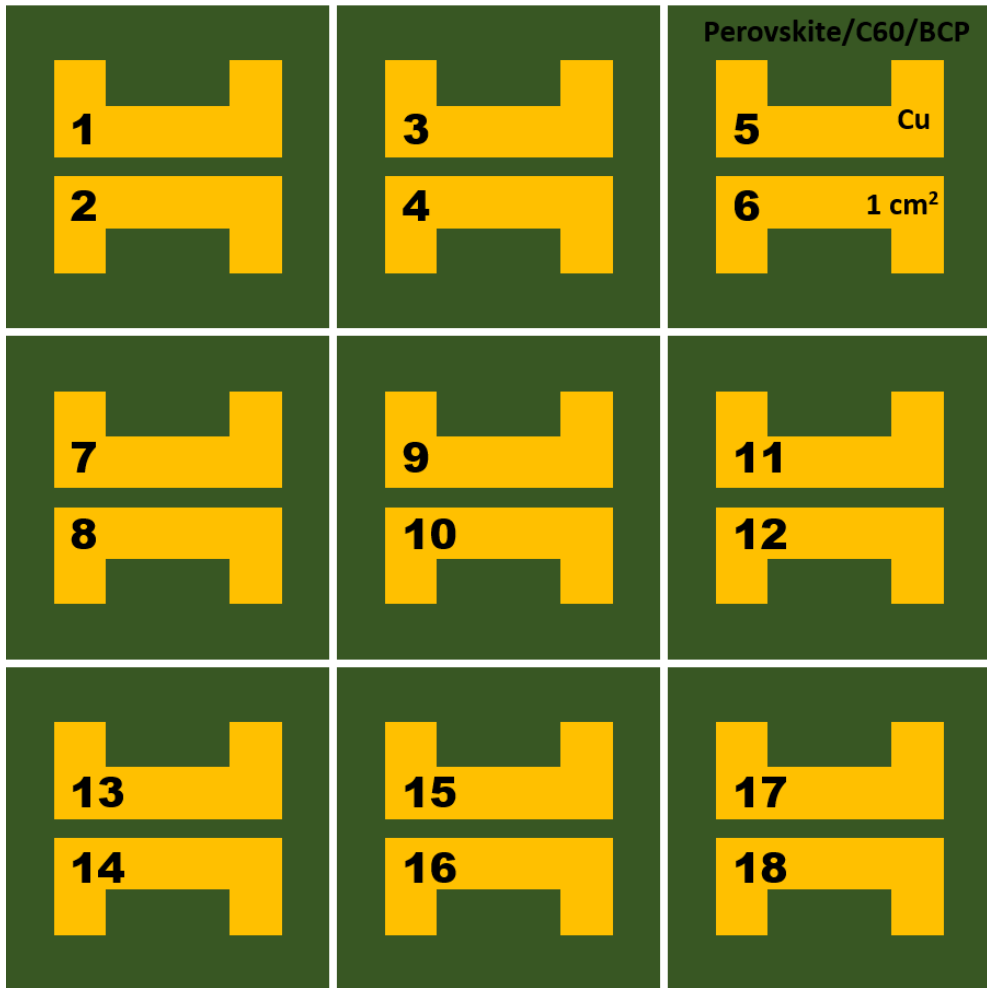


Figure 2.12. Schematic image of the active areas (1 cm²) on the large-area electrodes.

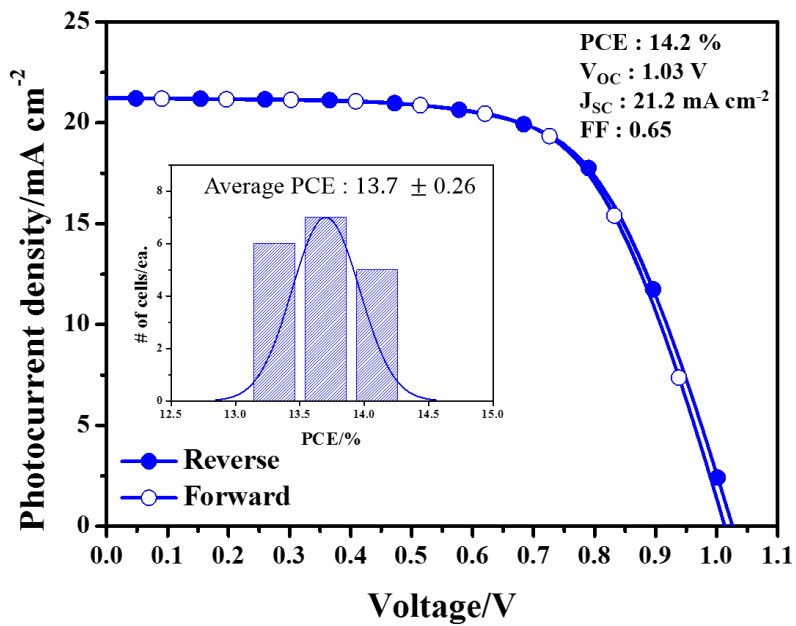


Figure 2.13. *J-V* curves and histogram (inset) of 18 megasonic sprayed perovskite solar cells with a 1 cm² active area under 1 sun illumination.

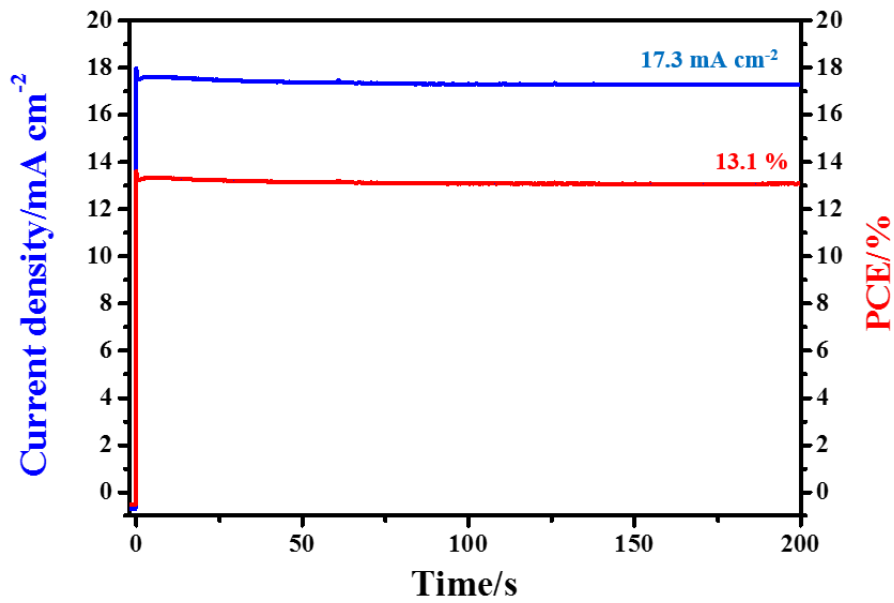


Figure 2.14. Stabilized photocurrent density (blue) and power conversion efficiency (red) measured at maximum power voltage of 0.76V for 200 seconds of the 15 mm/s device with an active area of 1 cm² under 1 sun illumination.

2.3. Conclusion

We have developed a highly reproducible megasonic-spray coating method for the fabrication of MAPbI₃ films for perovskite solar cells. In this method, high quality MAPbI₃ films can be prepared at low temperature with an anti-solvent free process at ambient conditions. The most efficient solar cells fabricated using megasonic-spray coating in our study exhibits a PCE of 16.9%, with an average PCE of 16.4% (the highest average efficiency among spray coated perovskite solar cells). Megasonic-spray coating was successfully applied to the continuous fabrication of uniform, highly crystalline, and large-grain MAPbI₃ films. Large-area optimized perovskite films were used to fabricate efficient PSCs with a PCE of 14.2% (with an active area of 1 cm²) (the highest efficiency among spray coated large area perovskite solar cells) and excellent film uniformity over large areas (an aperture area was used of 7.5 cm × 7.5 cm). The megasonic-spray coating process demonstrates a unique technique that could be easily adapted to polymer substrates, large area devices, and large area modules with its low temperature and ambient conditions. This method will open a new route for roll-to-roll and will be studied in our following project.

2.4. Experimental Methods

2.4.1. Fabrication of Megasonic-Spray Coated Perovskite Solar Cells

Substrates were treated with UV-ozone for 30 min to remove any remaining solvent and lower the surface energy. The PEDOT:PSS (Clevios PVP AI 4083, Heraeus) solution was spin-coated on the UV-ozone treated ITO-glass substrates at 5000 rpm for 40 s and dried at 120 °C for 20 min. The $\text{CH}_3\text{NH}_3\text{PbI}_3$ (MAPbI_3) perovskite precursor solution was then deposited on the substrates using a megasonic nebulizer spray system. The perovskite precursor solution was prepared by dissolving PbI_2 (Alfa Aesar) in a 1:1:1 molar ratio solution composed of MAI (synthesized using a previously reported method [23]), and DMSO (Sigma-Aldrich) in DMF (Sigma Aldrich) at 50 wt%. The substrates were deposited on a hot-plate, situated 30 mm under the nozzle. The temperature of the substrate was 120 °C during the spraying and the flow rate of the solution was set to 5 L/min with 7 mm² of nozzle size. The deposited substrates were post-annealed at 120 °C for 1 min with DMSO vapor and 4 min in air. All megasonic-spray coating and annealing processes were carried out in a closed chemical hood under ambient conditions. For scaling up this process, a careful control of exhaust gas flows should be needed. C_{60} (20 nm), bathocuproine (BCP, 10 nm), and Cu (50 nm) were then sequentially deposited by thermal evaporation. In the case of the large area (7.5 cm × 7.5 cm) perovskite layer coating, 9 substrates of 2.5 cm × 2.5 cm were deposited on the hot-plate which were processed with the same conditions.

2.4.2. Characterizations and Measurements

The $J-V$ characteristics were measured using a source meter (Keithley 2400, Tektronix) under AM 1.5G illumination conditions with an intensity of 100 mW/cm^2 using an Oriel S013 ATM solar simulator, calibrated by a KG5 filtered monocrystalline silicon reference solar cell (91150-KG5, Newport). Our devices were tested at room temperature ($25 \text{ }^\circ\text{C}$) in a glove box. The scan rates were set to 200 ms per 20 mV. The devices were covered with a metal shadow mask of 0.0754 cm^2 for the small cells and 1 cm^2 for the large cells, to restrict the size of the active area. IPCE spectra were measured with a Newport IQE200 system equipped with a 300 mW Xenon lamp and a lock-in amplifier. A sympatec HELOS laser diffraction droplet sizing system (Sympatec Inc., Clausthal, Germany) was used to measure size distribution of the perovskite aerosol particles. SEM images of the surfaces were obtained using a field-emission scanning electron microscope (MERLIN, Carl Zeiss), whereas cross-sectional images were obtained with a focused-ion-beam (FIB) system (AURIGA, Carl Zeiss). X-ray diffraction (XRD) analysis was carried out to characterize the crystal structure, using New D8 Advance (Bruker). Electrochemical impedance spectroscopy (EIS) analysis was carried out with an electrochemical workstation (Autolab, 320N, Metrohm) equipped with an Autolab LED driver kit. EIS measurements were carried out at various bias voltages with an intensity of 100 mW/cm^2 using a white LED (LDCNW, Autolab) light, with a frequency of 0.01-1 MHz. The EIS spectra were fitted using the Z-View software (Scribner Associates) with an equivalent circuit. The absorbance spectra and crystalline diffraction patterns were recorded using an ultraviolet-visible/near-infrared (NIR) spectrophotometer (Cary 5000, Agilent Technologies). Time-resolved photoluminescence (TRPL)

measurements were conducted using a FluoroMax-4 spectrofluorometer (Horiba). A 463-nm laser diode (DeltaDiode-470L, Horiba), pulsed at a frequency of 100 MHz, was used as a light source for photoexcitation. The resulting PL was measured using a high-sensitivity photon counting NIR detector.

2.5. References

- [1] S. S. Shin, E. J. Yeom, W. S. Yang, S. Hur, M. G. Kim, J. Im, J. Seo, J. H. Noh and S. I. Seok, *Science*, **2017**, *356*, 167-171.
- [2] Z. Wei, H. Chen, K. Yan and S. Yang, *Angewandte Chemie*, **2014**, *126*, 13455-13459.
- [3] M. Yang, Z. Li, M. O. Reese, O. G. Reid, D. H. Kim, S. Siol, T. R. Klein, Y. Yan, J. J. Berry and M. F. van Hest, *Nature Energy*, **2017**, *2*, 17038.
- [4] W. S. Yang, J. H. Noh, N. J. Jeon, Y. C. Kim, S. Ryu, J. Seo and S. I. Seok, *Science*, **2015**, *348*, 1234-1237.
- [5] Z. Yang, C. C. Chueh, F. Zuo, J. H. Kim, P. W. Liang and A. K. Y. Jen, *Advanced Energy Materials*, **2015**, *5*, 1500328.
- [6] W. S. Yang, B.-W. Park, E. H. Jung, N. J. Jeon, Y. C. Kim, D. U. Lee, S. S. Shin, J. Seo, E. K. Kim and J. H. Noh, *Science*, **2017**, *356*, 1376-1379.
- [7] D. Song, J. J. Kim, W. Cho, T.-Y. Kim, J. H. Lee, Y. R. Kim, D. Jeong, B. S. Kim, W. Wei and Y. S. Kang, *Macromolecular Research*, **2015**, *23*, 705-708.
- [8] S. Das, B. Yang, G. Gu, P. C. Joshi, I. N. Ivanov, C. M. Rouleau, T. Aytug, D. B. Geohegan and K. Xiao, *ACS Photonics*, **2015**, *2*, 680-686.
- [9] J. Fu, N. N. Daanen, E. E. Rugen, D. P. Chen and S. E. Skrabalak, *Chemistry of Materials*, **2016**, *29*, 62-68.
- [10] S. C. Hong, G. Lee, K. Ha, J. Yoon, N. Ahn, W. Cho, M. Park and M. Choi, *ACS applied materials & interfaces*, **2017**, *9*, 7879-7884.
- [11] D. K. Mohamad, J. Griffin, C. Bracher, A. T. Barrows and D. G. Lidzey, *Advanced Energy Materials*, **2016**, *6*, 1600994.

- [12] M. Ramesh, K. M. Boopathi, T.-Y. Huang, Y.-C. Huang, C.-S. Tsao and C.-W. Chu, *ACS applied materials & interfaces*, **2015**, 7, 2359-2366.
- [13] S. Bag, J. R. Deneault and M. F. Durstock, *Advanced Energy Materials*, **2017**, 7, 1701151.
- [14] H. Huang, J. Shi, L. Zhu, D. Li, Y. Luo and Q. Meng, *Nano Energy*, **2016**, 27, 352-358.
- [15] S. Uličná, B. Dou, D. H. Kim, K. Zhu, J. M. Walls, J. W. Bowers and M. F. A. M. van Hest, *ACS Applied Energy Materials*, **2018**, 1, 1853-1857.
- [16] K. Hwang, Y. S. Jung, Y. J. Heo, F. H. Scholes, S. E. Watkins, J. Subbiah, D. J. Jones, D. Y. Kim and D. Vak, *Advanced Materials*, **2015**, 27, 1241-1247.
- [17] W.-Q. Wu, Q. Wang, Y. Fang, Y. Shao, S. Tang, Y. Deng, H. Lu, Y. Liu, T. Li, Z. Yang, A. Gruverman and J. Huang, *Nature Communications*, **2018**, 9, 1625.
- [18] M. Yang, D. H. Kim, T. R. Klein, Z. Li, M. O. Reese, B. J. Tremolet de Villers, J. J. Berry, M. F. A. M. van Hest and K. Zhu, *ACS Energy Letters*, **2018**, 3, 322-328.
- [19] Z. Yang, S. Zhang, L. Li and W. Chen, *Journal of Materiomics*, **2017**, 3, 231-244.
- [20] J. H. Heo, M. H. Lee, M. H. Jang and S. H. Im, *Journal of Materials Chemistry A*, **2016**, 4, 17636-17642.
- [21] W.-N. Wang, A. Purwanto, I. W. Lenggoro, K. Okuyama, H. Chang and H. D. Jang, *Industrial & Engineering Chemistry Research*, **2008**, 47, 1650-1659.
- [22] S. Tsai, Y. Song, C. Tsai, C. Yang, W. Chiu and H. Lin, *Journal of materials*

science, **2004**, *39*, 3647-3657.

- [23] N. Ahn, D.-Y. Son, I.-H. Jang, S. M. Kang, M. Choi and N.-G. Park, *Journal of the American Chemical Society*, **2015**, *137*, 8696-8699.
- [24] Y. Jiang, C. Wu, L. Li, K. Wang, Z. Tao, F. Gao, W. Cheng, J. Cheng, X.-Y. Zhao and S. Priya, *Nano Energy*, **2018**, *53*, 440-448.
- [25] Z. Liang, S. Zhang, X. Xu, N. Wang, J. Wang, X. Wang, Z. Bi, G. Xu, N. Yuan and J. Ding, *Rsc Advances*, **2015**, *5*, 60562-60569.
- [26] Q. Wang, M. Lyu, M. Zhang, J.-H. Yun, H. Chen and L. Wang, *The Journal of Physical Chemistry Letters*, **2015**, *6*, 4379-4384.
- [27] T. Zhang, M. Yang, Y. Zhao and K. Zhu, *Nano letters*, **2015**, *15*, 3959-3963.
- [28] Y. H. Chiang, H. M. Cheng, M. H. Li, T. F. Guo and P. Chen, *ChemSusChem*, **2016**, *9*, 2620-2627.
- [29] S.-H. Turren-Cruz, M. Saliba, M. T. Mayer, H. Juárez-Santiesteban, X. Mathew, L. Nienhaus, W. Tress, M. P. Erodici, M.-J. Sher and M. G. Bawendi, *Energy & Environmental Science*, **2018**, *11*, 78-86.
- [30] Z. Yu, L. Zhang, S. Tian, F. Zhang, B. Zhang, F. Niu, P. Zeng, J. Qu, P. N. Rudd and J. Huang, *Advanced Energy Materials*, **2018**, *8*, 1701659.
- [31] H. Dong, S. Pang, Y. Zhang, D. Chen, W. Zhu, H. Xi, J. Chang, J. Zhang, C. Zhang and Y. Hao, *Nanomaterials*, **2018**, *8*, 720.
- [32] J. Jiang, Z. Jin, J. Lei, Q. Wang, X. Zhang, J. Zhang, F. Gao and S. F. Liu, *Journal of Materials Chemistry A*, **2017**, *5*, 9514-9522.
- [33] G. J. A. Wetzelaer, M. Scheepers, A. M. Sempere, C. Momblona, J. Ávila and H. J. Bolink, *Advanced Materials*, **2015**, *27*, 1837-1841.
- [34] J. H. Heo, H. J. Han, D. Kim, T. K. Ahn and S. H. Im, *Energy & Environmental Science*, **2015**, *8*, 1602-1608.

- [35] O. Malinkiewicz, A. Yella, Y. H. Lee, G. M. Espallargas, M. Graetzel, M. K. Nazeeruddin and H. J. Bolink, *Nature Photonics*, **2014**, *8*, 128.
- [36] P. Li, C. Liang, B. Bao, Y. Li, X. Hu, Y. Wang, Y. Zhang, F. Li, G. Shao and Y. Song, *Nano Energy*, **2018**, *46*, 203-211.
- [37] B. J. Kim, M. c. Kim, D. G. Lee, G. Lee, G. J. Bang, J. B. Jeon, M. Choi and H. S. Jung, *Advanced Materials Interfaces*, **2018**, 1800993.
- [38] H. Peng, W. Sun, Y. Li, W. Yan, P. Yu, H. Zhou, Z. Bian and C. Huang, *Journal of Photonics for Energy*, **2016**, *6*, 022002.
- [39] V. Gonzalez-Pedro, E. J. Juarez-Perez, W.-S. Arsyad, E. M. Barea, F. Fabregat-Santiago, I. Mora-Sero and J. Bisquert, *Nano letters*, **2014**, *14*, 888-893.
- [40] A. Fakharuddin, L. Schmidt-Mende, G. Garcia-Belmonte, R. Jose and I. Mora-Sero, *Advanced Energy Materials*, **2017**, *7*, 1700623.
- [41] F. Fabregat-Santiago, G. Garcia-Belmonte, I. Mora-Seró and J. Bisquert, *Physical chemistry chemical physics*, **2011**, *13*, 9083-9118.
- [42] E. J. Juarez-Perez, M. Wußler, F. Fabregat-Santiago, K. Lakus-Wollny, E. Mankel, T. Mayer, W. Jaegermann and I. Mora-Sero, *The journal of physical chemistry letters*, **2014**, *5*, 680-685.
- [43] H. Zhou, Q. Chen, G. Li, S. Luo, T.-b. Song, H.-S. Duan, Z. Hong, J. You, Y. Liu and Y. Yang, *Science*, **2014**, *345*, 542-546.
- [44] M.-c. Kim, B. J. Kim, D.-Y. Son, N.-G. Park, H. S. Jung and M. Choi, *Nano letters*, **2016**, *16*, 5756-5763.
- [45] B.-W. Park, B. Philippe, S. M. Jain, X. Zhang, T. Edvinsson, H. Rensmo, B. Zietz and G. Boschloo, *Journal of Materials Chemistry A*, **2015**, *3*, 21760-21771.

- [46] J. Chang, H. Zhu, B. Li, F. H. Isikgor, Y. Hao, Q. Xu and J. Ouyang, *Journal of Materials Chemistry A*, **2016**, *4*, 887-893.
- [47] M. Hirasawa, T. Ishihara, T. Goto, K. Uchida and N. Miura, *Physica B: Condensed Matter*, **1994**, *201*, 427-430.
- [48] Q. Lin, A. Armin, R. C. R. Nagiri, P. L. Burn and P. Meredith, *Nature Photonics*, **2015**, *9*, 106.
- [49] K. Tanaka, T. Takahashi, T. Ban, T. Kondo, K. Uchida and N. Miura, *Solid state communications*, **2003**, *127*, 619-623.
- [50] Q. Dong, Y. Fang, Y. Shao, P. Mulligan, J. Qiu, L. Cao and J. Huang, *Science*, **2015**, aaa5760.
- [51] Q. Jiang, L. Zhang, H. Wang, X. Yang, J. Meng, H. Liu, Z. Yin, J. Wu, X. Zhang and J. You, *Nature Energy*, **2017**, *2*, 16177.
- [52] Y. Li, Y. Zhao, Q. Chen, Y. Yang, Y. Liu, Z. Hong, Z. Liu, Y.-T. Hsieh, L. Meng and Y. Li, *Journal of the American Chemical Society*, **2015**, *137*, 15540-15547.
- [53] Z. Liu, L. Qiu, E. J. Juarez-Perez, Z. Hawash, T. Kim, Y. Jiang, Z. Wu, S. R. Raga, L. K. Ono and S. F. Liu, *Nature communications*, **2018**, *9*, 3880.

Chapter 3. Film-Growth-Megasonic-Spray-Coating System for Flexible Perovskite Solar Cells and Modules

3.1. Introduction

Organometallic halide perovskite solar cells (PSCs) have gained a reputation as a promising, next-generation energy generating device mainly due to their dramatic increase in power conversion efficiencies (PCEs). [1-6] This led to the increasing request for flexible-substrate based PSCs (f-PSCs) which boast a variety of potential applications including wearable electronics, portable electronic devices, flying objects, etc. [7-11] Although spin-coating methods to make f-PSCs with high PCEs have been available, [12] the scalable coating system needs to be developed for their commercialization which requires fabrication of large area perovskite layer on polymer-based flexible substrates. [13-16]

Meniscus-assisted-coating (MAC) methods (e.g. bar-coating, slot-die coating, etc.), among existing automatic scalable thin-film coating techniques, generate the most tenacious glass-based PSCs with high PCEs over 20%. [17-21] These methods, however, have not shown significant performance on f-PSCs in comparison with the glass-based ones due to the foundational limitation of their coating principle that does not work well with the low wettability substrate. [22-24] The MAC methods basically balance the surface tension of perovskite precursor

solution and the wettability between the substrate and the solution to sustain uniform perovskite wet-film during crystallization as shown in **Figure 3.1a**. [25-27] This applies well to the glass-based hydrophilic substrates. When this applies to scalable coating on the flexible substrates, however, maintaining the wet-film becomes challenging due to considerable coverage reduction during solution spreading and solvent evaporation (**Figure 3.1a-2**). This is due to the high contact-angles (equals to hydrophobic surface) that the conventional flexible-transparent conductive oxide (TCO)-substrates including indium tin oxide (ITO) coated polyethylene naphthalate (PEN) and polyethylene terephthalate (PET) films have. Even with a hole transporting layer (poly(triaryl amine), or PTAA) that has been additionally coated, their contact-angles are much higher than commercial ITO coated glass substrates (glass/ITO) as can be seen in **Figure 3.2**.

Compared to the aforementioned methods, spray-coating technique has many advantages explained below and thus is a promising scalable coating method to produce high quality perovskite film. With a precursor solution, this method fabricates fine precursor droplets and transports them to substrates. These fine perovskite precursor droplets with their exceptionally small volume support quick evaporation of solvent on the heated substrates with no additional treatments of anti-solvent, air-knife, etc. [28-30] This means that the deposited droplets has less coverage reduction during coating and solvent evaporation and thus stimulates of pinhole-free, uniform perovskite thin-film (**Figure 3.1b-3**) on adverse substrates. This advantage of the spraying method led many researchers to use its features of fine droplet size, [28,29] droplet size control, [28] detailed thickness control, [29] high material utilization, and automation properties for fabrication of perovskite films. The main focus of the studies was to fabricate high efficiency, stable unit cells

on glass-based substrates. [28-34] Our previous work was in line with this as we used fine perovskite droplets to easily attain scalability. [29] In these studies that utilized the spray-coating method including ours, however, the principles of perovskite film growth on flexible substrates by means of spray-coating had been ambiguous and fabrication of flexible perovskite solar module (f-PSM) had not been fully validated.

In the present study, we suggest Film-Growth-Megasonic-Spray-Coating (FGMSC) method, a completely automated system for continuous production of high performance, large-area flexible perovskite solar cells and modules. Among various spray technologies such as a few hundred kHz level ultrasonic-spray, [30] electro-spray, [28] and air-brush-spray, [31] we used the 1.7 MHz megasonic-spray method [29] that constantly generates fine and homogeneous perovskite precursor droplets ($< 10 \mu\text{m}$) and implemented multiple spray-coating to make flexible perovskite solar module. We have explicated the size distribution of megasonic-sprayed perovskite precursor droplets along with the wettability of the flexible substrates and examined in depth the formation characteristics of perovskite layer (e.g. film coverage, roughness, and crystal grain size) in accordance with droplet supply rate and multiple spray. As a result, we have effectively corroborated the principles of mechanisms of perovskite film growth and successfully demonstrated the use of our FGMSC system in the production of defect-free uniform perovskite film on the flexible substrates. The FGMSC system has attained outstanding PCEs of more than 18% proved by the best PCE in unit cells. The scalability of the system has also been validated in the fabrication of large area (100cm^2) perovskite layer on a flexible substrate with uniform solar cells that have shown the average PCE of $17.47 \pm 0.22\%$ and flexible perovskite solar mini-module with PCE of 16.10%

measured from an active area of 35.1 cm². The encapsulated flexible mini-module maintained 97% of its initial efficiency after 200 h under continuous 1-sun illumination.

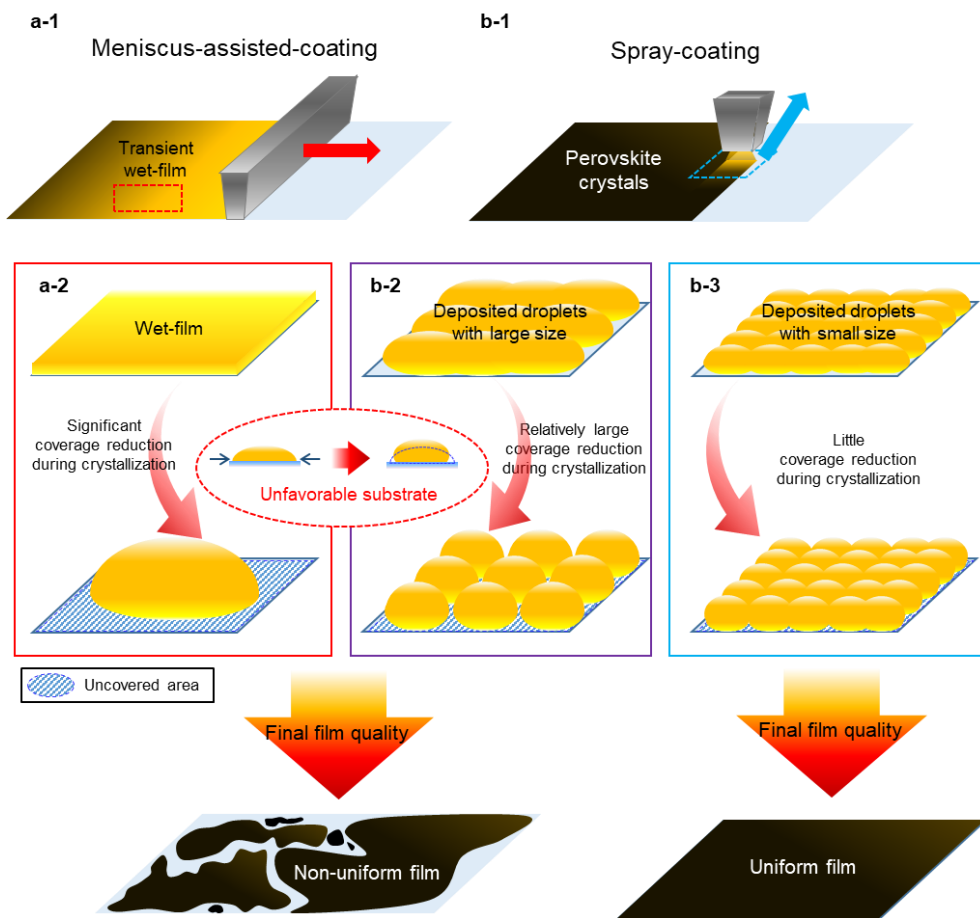


Figure 3.1. Schematic illustrations of coating mechanisms; (a) meniscus-assisted-coating and (b) spray-coating.

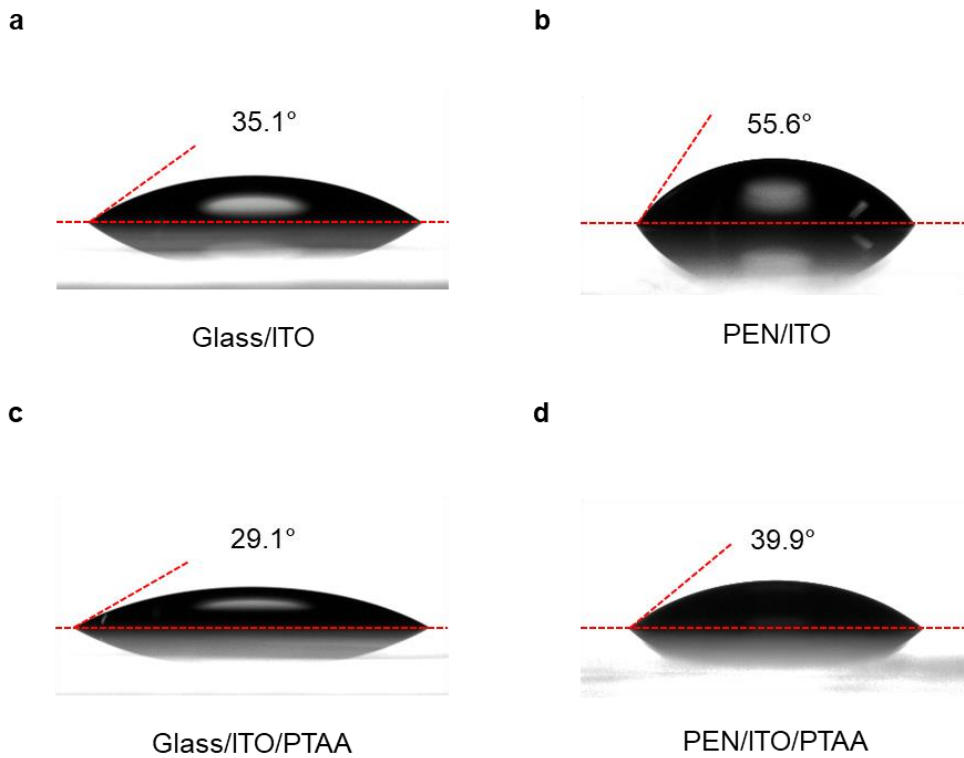


Figure 3.2. Contact angles of perovskite solution dropped on (a) glass/ITO, (b) PEN/ITO, (c) glass/ITO/PTAA and (d) PEN/ITO/PTAA substrates.

3.2. Results and Discussion

3.2.1. Steady Production of Fine Perovskite Precursor Droplets

In the system of spray-coating, the size and size uniformity of perovskite precursor droplets layered on a substrate directly affect the quality of the perovskite film. [28,29] When the droplets are large-sized, their evaporation is slowed even in a small number [28,29,35,36] which then may cause the substrate to have many pinholes and the film to have irregular surface roughness. In general, the mean droplet size created by a vibrating aerosol generator is expressed by Lang's equation:

$$d_d = 0.34 \left(\frac{8\pi\gamma}{\rho f^2} \right)^{1/3} \quad (1)$$

where γ , ρ , and f are the surface tension of precursor (γ , Ns/m²), density of precursor (ρ , kg/m³) and frequency of vibrator (f , Hz), respectively. [37] As can be seen in **Figure 3.3**, our FGMS system produces fine droplets (< 10 μm) that have the geometric mean diameter of (GMD) of 3.622 μm and geometric standard deviation (GSD) of 1.564 from the 1.7 MHz megasonic generator which shows much higher frequency than existing ultrasonic generators have. (< 0.5 MHz, **Figure 3.4**) [38-41] The droplets that are produced continuously exhibit no change of the GMD, GSD and the size distribution for more than 30 min (**Figure 3.5**).

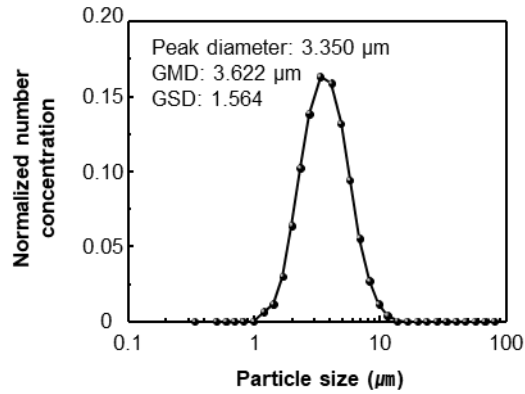


Figure 3.3. Size distribution of generated perovskite precursor droplets by the FGMS system. The geometric standard deviation (GSD) is given by $\exp\left(\sqrt{\frac{\sum n_j (\ln d_j - \ln d_g)^2}{N - 1}}\right)$, where d_j is the diameter of an individual particle, n_j is the number of particles in the j^{th} group, N is the total number of particles, and $\ln d_g$ is the natural logarithm of the geometric mean diameter (GMD) of the particles, defined as $\sum n_j \ln d_j / N$.

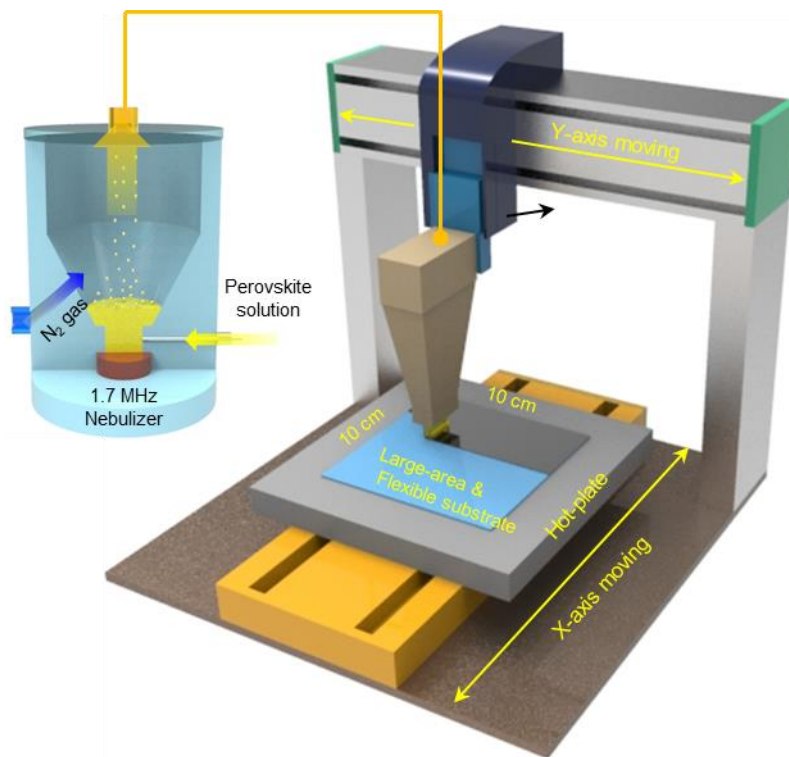


Figure 3.4. Illustrations of Film-Growth-Megasonic-Spray-Coating (FGMSC) system which is consisted of two main parts: droplet generation part (left) and motion control part (right).

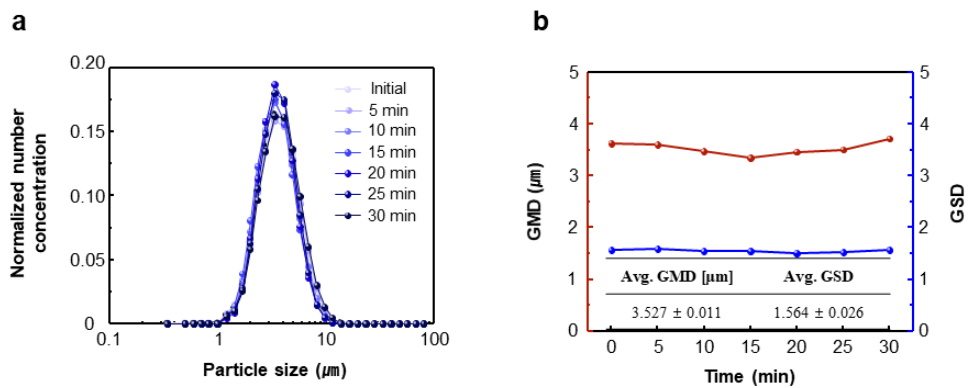


Figure 3.5. Changes in (a) size distribution, (b) geometric mean diameter (GMD, red) and geometric standard deviation (GSD, blue) of the perovskite droplets over 30 min.

3.2.2. Relationship among Film Coverage, Crystal Growth and Supply Rate of Droplets

To use the megasonic-spray coating system in production of uniform, high-quality perovskite film, we investigated the relationship among perovskite film surface coverage, perovskite crystals grain growth and supply rate of perovskite droplets on a substrate which can be managed by the moving speed of the spray nozzle. In **Figure 3.6a**, the relationship between the coverage of the films and the nozzle speed along with their SEM images, which presents a reversed S-shape curve. The coated substrates showed the shape of residues of the droplets at the speeds from 500 to 300 mm/s, because the droplets layered on the substrates were hardly joined with each other during coating due to the supply rate that was too low (compared to too fast nozzle speed). The coverage, then, failed to increase but remained below 50% even when decreasing the speed. (This region is, in the present study, referred to as “Droplet Coating (DC)” region.) On the contrary, at the speeds from 250 to 50 mm/s, the coated substrates exhibited the shape of film and were thus labelled as “Film Coating (FC)” region. The coverage in this FC region drastically increased compared to the DC region (from 45.7 to 78.6% at the speeds from 300 to 250 mm/s) which surpassed 99% when the speed dropped to 50 mm/s. These results demonstrate that droplets supported by the slow nozzle speed covered the substrates in adequate amount before they were completely evaporated during coating and thus formed in a shape of film.

The size of the perovskite crystal grain is also affected by the coating speed. **Figure 3.6b** shows the relationship between the grain size and nozzle speed along with SEM images of the grains in the film. We fitted a function of

$$d_g - d_{g,min} = d_{g,max}(e^{-v/v_0}) \quad (2)$$

with the average grain size measured in the experiment where d_g is the grain size, $d_{g,max}$ and $d_{g,min}$ are the maximum and minimum grain sizes, respectively. v is the nozzle speed and v_0 is the characteristic nozzle speed which can be the slope (α) obtained from the fitting equation in the logarithmic plot ($\alpha = -1/v_0$). The value of α is evidently distinguished in the FC and DC regions (-0.011 and -0.001, respectively) in **Figure 3.6b**. In the DC region where most of the droplets are evaporated separately and solidified without adhering to each other, the size of the grains ended up in ~ 100 nm, disregarding the speed. In the FC region, on the contrary, the droplets intermingle with each other, resulting in delayed evaporation and stimulated growth of perovskite crystals. The grain size, then, substantially enlarged according to the decreasing speed (from 147 to 1011 nm at the speeds from 250 to 50 mm/s). This size magnification is 10 times faster than in the DC region. With these results combined, we have employed repetitive megasonic-spray coating in FC mode to guarantee uniform surface roughness, large-grain perovskite films without pinholes.

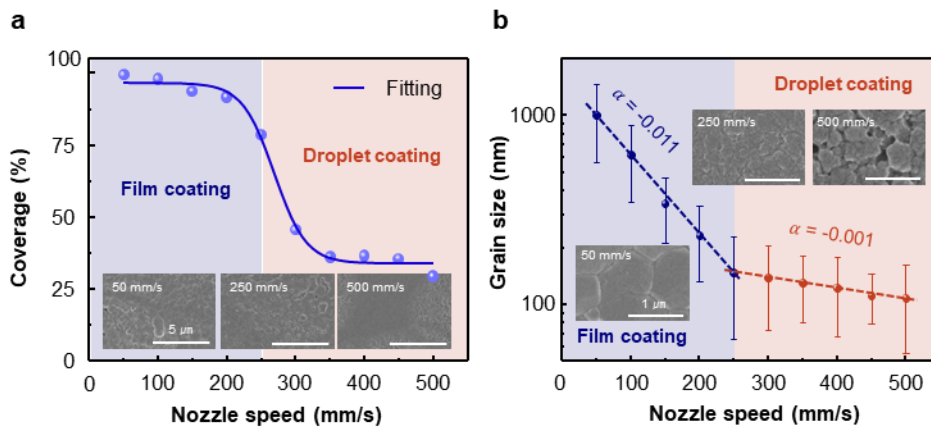


Figure 3.6. (a) Perovskite film coverage and (b) grain size according to nozzle moving speed from 50 to 500 mm/s.

3.2.3. Film-Growth-Megasonic-Spray-Coating (FGMSC) Technique

We have produced a perovskite film without any pinholes by repeated coating (coverage of 100% at 5 cycles) at the 450 mm/s (DC region) but the grain sizes of the film stayed as ~200 nm after the cycles, as shown in **Figure 3.7a-b** and **3.8**. This is because the droplets failed to be evenly distributed on the film during repeated coating cycles due to too fast nozzle speed and thus did not adequately resolve and resolidify the existing perovskite grains during repeated cycles. At the speeds from 75 and 225 mm/s (FC region), however, we have successfully produced uniformly layered perovskite films within a few cycles (100% at 2 cycles) with the grains that drastically increased in size up to 3 cycles of coating process; from 800 to 1000 nm at the 75 mm/s and from 200 to 650 nm at the 225 mm/s. Thanks to the high supply rate of droplets in FC mode, the grains that had been solidified were suitably resolved and progressively resolidified during the repeated coating. Therefore, the perovskite film coverage is expanded and the perovskite grains in the film are progressively and evenly augmented through the repeated coating process, which makes the film seem as growing. Thus, this technique is named as Film-Growth-Megasonic-Spray-Coating (FGMSC).

Furthermore, we examined the thickness and grain formation of the films by using the focused ion beam SEM (FIB-SEM) system to analyze their cross-sectional images. To examine spatial uniformity, we selected three locations (A-C) (**Figure 3.7c**.) For unbiased comparison, we settled the overall spraying time by managing the coating cycle of 1, 3 and 6 at the nozzle speed of 75 mm/s, 225 and 450 mm/s, respectively. The films produced through different nozzle speeds showed the average thickness of ~800 nm (Spray-coating based PSCs generally have the

perovskite layer with thickness of 800 nm. [29,31,42]) due to the equal total spraying time. However, their surface roughness and grain formation showed astounding differences, as can be seen in **Figure 3.7d** and **Table 3.1**. At the speed of 75 mm/s, although the thickness of the film is comparable to the grain size, the film exhibited the largest standard deviation of the average thickness of 273.6 nm and had pinholes (top of **Figure 3.7d**). The lowest standard deviation of 15.5 nm was observed at the speed of 450 mm/s and there were small grains accumulated in layers (bottom of **Figure 3.7d**). At the speed of 225 mm/s, the grains in the film were as big as those at the speed of 75 mm/s and the film was as uniform as at the speed of 450 mm/s (middle of **Figure 3.7d**).

To prove the effects of the repeated coating on the quality of perovskite films, we measured time-resolved photoluminescence (TRPL), examined the optical absorption, and studied x-ray diffraction (XRD) patterns (**Figure 3.9** and **Table 3.2**). The average PL lifetime (τ_{avg}) of the 225 mm/s film (368.40 ns) was similar to that of the 75 mm/s film (375.88 ns) and longer than that of the 450 mm/s film (307.28 ns) as presented in **Table 3.2**. This shows that the non-radiative charge recombination in both cases of 75 mm/s and 225 mm/s was sufficiently suppressed compared to that of the 450 mm/s film, which is consistent with the results of SEM images. [43-45] At the 450 mm/s film, many grain boundaries of small grains work as a recombination site which caused short carrier lifetime. On the contrary, the large grains of the 75 mm/s and 225 mm/s films let them have a longer carrier lifetime. The optical absorption (**Figure 3.9b**) demonstrated similar tendency to the results of the TRPL, which is also affected by the perovskite crystal grain size. As suggested in **Figure 3.9c**, the XRD patterns and full width at half maximum (FWHM, inset) of the peak corresponding to the black phase perovskite crystal plane of (110) (at $2\theta =$

14.1°) apparently show that all the films were formed with high crystalline perovskite crystals with little impurities, such as PbI_2 (at $2\theta = 12.6^\circ$) and yellow phase hexagonal crystals (at $2\theta = 11.6^\circ$). [2,46-48] These results prove that the FGMS technique successfully produces high-quality perovskite film on polymer-based flexible substrates with low wettability.

Nozzle speed [mm/s]	Location	Max [nm]	Min [nm]	Deviation b/w Max and Min [nm]	Average thickness [nm]
75	A	1102.7	0.0	1102.7	727.9 ± 392.7
	B	883.6	682.2	201.4	794.2 ± 86.3
	C	930.1	363.0	567.1	715.1 ± 243.6
	Average	972.1 ± 94.3	348.4 ± 278.7	623.7 ± 370.2	745.8 ± 273.6
225	A	864.4	724.7	139.7	803.0 ± 45.9
	B	847.9	754.8	93.2	819.5 ± 33.0
	C	864.4	820.5	43.8	843.8 ± 15.1
	Average	858.9 ± 7.7	766.7 ± 40.0	92.2 ± 39.2	822.1 ± 37.7
450	A	850.7	793.2	57.5	823.8 ± 19.6
	B	849.3	809.6	39.7	829.3 ± 14.8
	C	831.5	806.8	24.7	820.5 ± 9.0
	Average	843.8 ± 8.7	803.2 ± 7.2	40.6 ± 13.4	824.6 ± 15.5

Table 3.1. Thickness of perovskite layers at selected locations (A-C).

Nozzle speed [mm/s]	A_1 [%]	τ_1 [ns]	A_2 [%]	τ_2 [ns]	A_3 [%]	τ_3 [ns]	τ_{avg} [ns]
75	13	143.48	3	8.55	84	388.91	375.88
225	6	87.56	23	0.97	73	373.75	368.40
450	12	120.32	58	322.25	30	1.66	307.28

Table 3.2. Tri-exponential fitting parameters of the TRPL decay for perovskite films on a bare PEN substrate. The perovskite layers were fabricated via the FGMSC system. Average lifetime (τ_{avg}) was calculated by $\tau_{avg} = \sum_i A_i \tau_i^2 / \sum_i A_i \tau_i$, where A_i and τ_i are amplitude ratio and lifetime of each time-component, respectively.

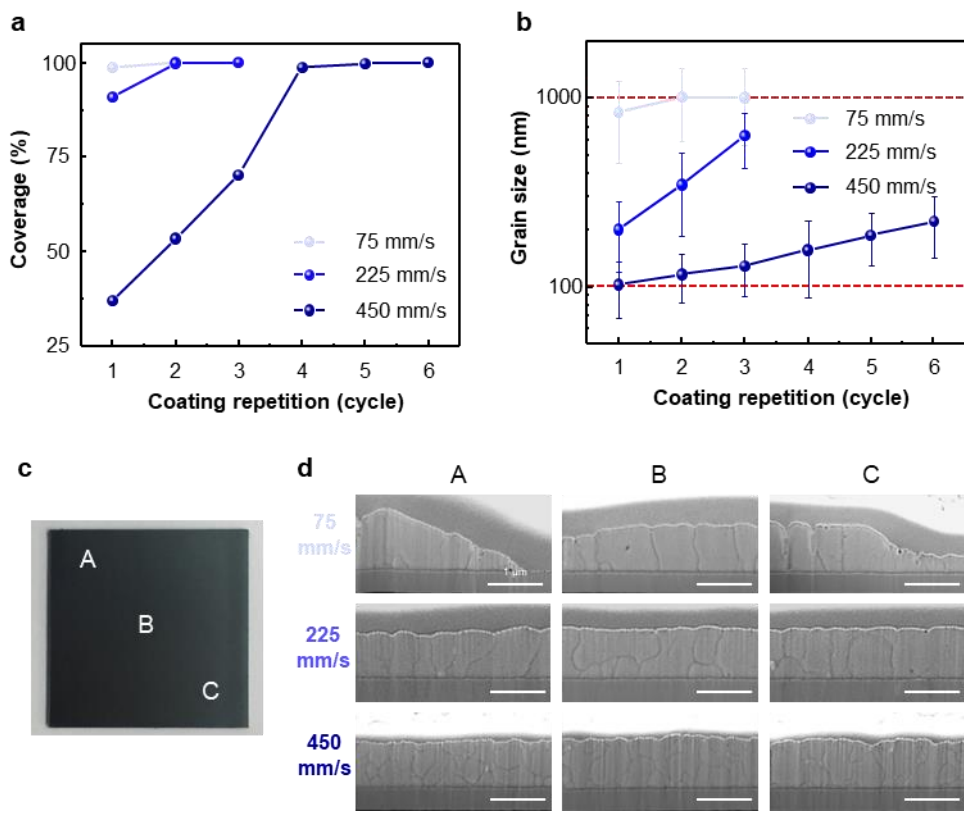


Figure 3.7. (a) Perovskite film coverage and (b) grain size with respect to 1 to 6 coating cycles and nozzle moving speed from 75 to 450 mm/s. (c) Photograph of perovskite layer on PEN/ITO substrate. (d) Cross-section SEM images of perovskite layers at the coating speed of 75, 225 and 450 mm/s.

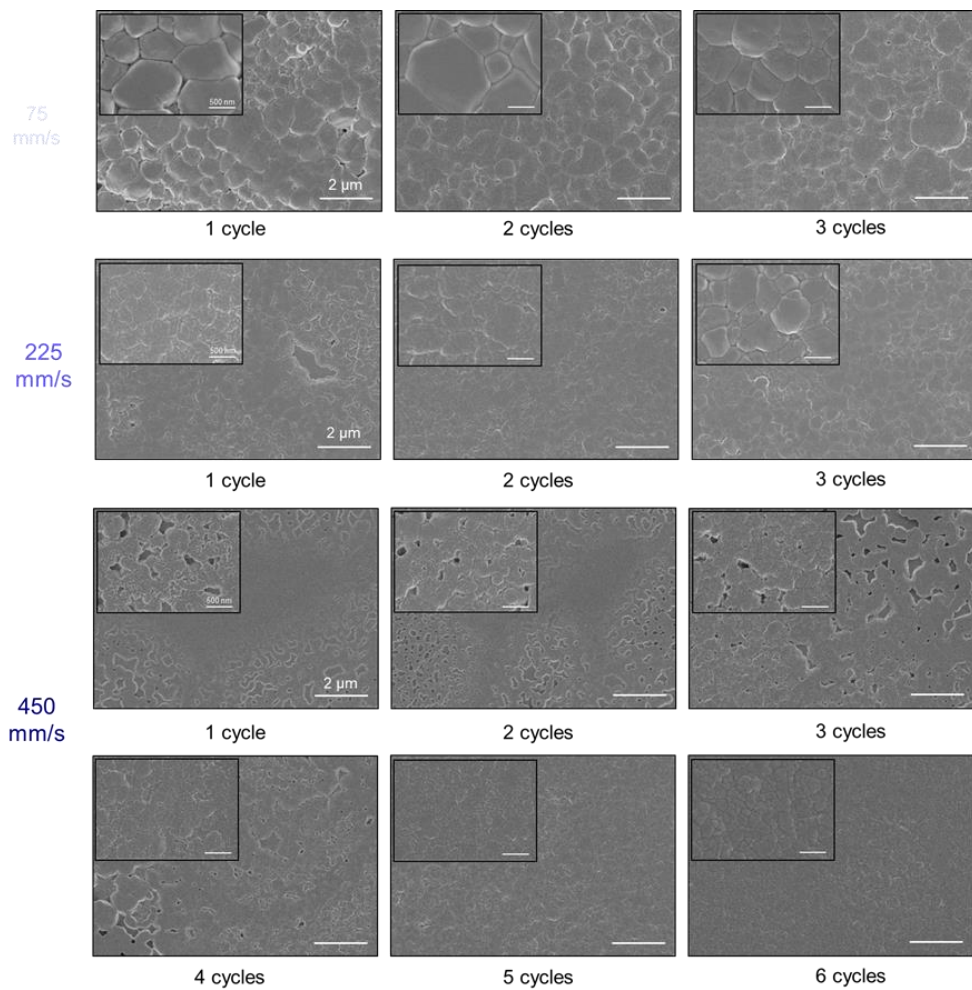


Figure 3.8. The SEM images of perovskite surface with respect to multiple coatings under each nozzle speed.

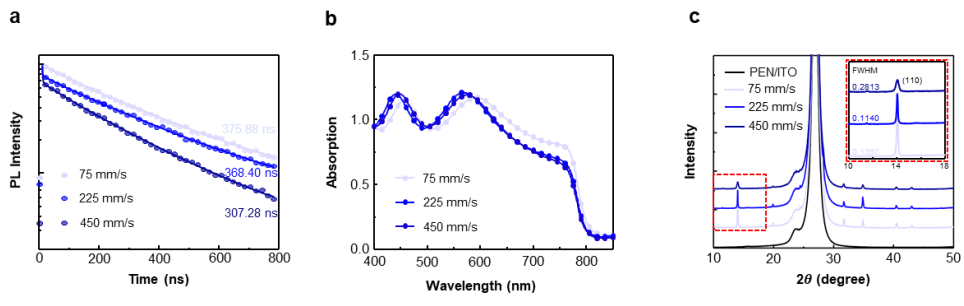


Figure 3.9. (a) TRPL spectra and (b) UV-Vis absorption spectra of the perovskite films coated on bare PEN substrates with respect to three coating conditions. (c) XRD patterns obtained from perovskite films coated on PEN/ITO substrates at three coating conditions. (110) peaks and FWHMs of the perovskite films in the inserted graph.

3.2.4. Fabrication of f-PSCs and Device Performance

We fabricated inverted f-PSCs (PEN/ITO/PTAA/perovskite/fullerene (C₆₀)/bathocuproine(BCP)/Cu) by using the triple cation perovskite composition ((CsPbI₃)_{0.02}(FA_{0.8}MA_{0.2}Pb(I_{2.8}Br_{0.2}))_{0.98}) to evaluate the photovoltaic performance of solar cells fabricated by our system. The photovoltaic performances of the devices are provided in **Figure 3.10a** and **Table 3.3**. The 225 mm/s devices demonstrated remarkable performances in all the three cases with the average PCE of $17.51 \pm 0.25\%$ with open-circuit voltage (V_{oc}) of 1.05 ± 0.01 V, short-circuit current density (J_{sc}) of 22.33 ± 0.50 mA/cm² and fill factor (FF) of 74.42 ± 1.56 . The 450 mm/s devices yielded an unsatisfactory result as the average PCE was $16.84 \pm 0.27\%$ with low J_{sc} due to the small grains with many grain boundaries (bottom image of **Figure 3.7d**) which showed defective crystallinity (**Figure 3.9c**) and short charge carrier lifetime (**Figure 3.9a**). Interestingly, the worst cell performances were shown in the 75 mm/s devices whose average PCE was $14.79 \pm 0.79\%$ even with the highest J_{sc} due to the largest grains. This is because the pinholes and unfavourable surface roughness of the film made the average V_{oc} and FF of the 75 mm/s devices drastically decrease over 10% as can be seen in the following experiments.

To examine the electrical features of the devices in three coating conditions, we carried out electrochemical impedance spectroscopy (EIS) measurements on the basis of the equivalent circuit analysis provided in **Figure 3.10b**, **3.11** and **3.12**. The semicircles of the high and low frequency regions are generally related to selective contact resistance (R_{sc}) and perovskite-interlayer-recombination resistance (R_{rec}), respectively. [49-51] As the second semicircles are identifiable in all cases, R_{rec} (**Figure 3.12**) is

effortlessly distinguished from the Nyquist plots. In the 75 mm/s device, the lowest R_{rec} value is found, which indicates the fastest recombination rate. The pinholes and rough surface of the film brings about direct carrier recombination at interfaces of charge transport layer (hole transport layer and electron transport layer), which cause V_{oc} and FF to decrease. [51] Contrastingly, the pinhole-free morphology of the perovskite film prevented recombination in 225 mm/s devices (the highest R_{rec}) and thus supported them to achieve the highest V_{oc} and FF. From these results, it is apparently clear that the FGMSC require optimum coating conditions (e.g. coating speed and number of coating repeats) to fabricate high performance solar devices. The best FGMSC condition among three cases, in the present study, is the 225mm/s with 3 cycles.

To exhibit the reproducibility of our FGMSC system, we fabricated additional f-PSCs under the best coating condition (50 unit-cells, 225 mm/s with 3 cycles). As presented in **Figure 3.10c**, the average PCE of the unit-cells was 17.51% with a small standard deviation of 0.26%, which exemplifies competent reproducibility of our FGMSC method. The highest PCE was 18.24% with little photocurrent hysteresis with J_{sc} was 22.37 mA/cm², with V_{oc} was 1.06 V, and with FF was 77.14 (**Figure 3.13**). Moreover, the f-PSCs produced by our system boasts high device stability which is supported by the results of the stabilized current density and PCE (**Figure 3.14**). The integrated current density analyzed by the external quantum efficiency (EQE) measurement was 21.77 mA/cm² and the stabilized current density and PCE at maximum power point (MPP) of 0.87 V for 600 s are 19.04 mA/cm² and 16.56%, respectively, which are in line with the result gained from the current density-voltage (J - V) curves.

To prove the flexibility of the f-PSCs produced by our FGMSC system, we performed bending durability tests with a variety of bending radius ($R_b = 10, 8, 6, 4$ mm, **Figure 3.10d-e**). The f-PSCs with $R_b = 10$ and 8 mm sustained their original PCEs after 1000 cycles (~100 and 80% of the values, respectively). On the other hand, the performances of the devices with $R_b = 6$ and 4 mm significantly declined (~60 and 30%, respectively) due to cracking of the ITO electrode. [7,52] (**Figure 3.15** shows the normalized PCEs of all bending tested f-PSCs according to the bending cycles.) Our results are in accordance with previous studies of f-PSCs produced on PEN/ITO substrates with a similar cell structure. [7,52]

Nozzle speed [mm/s]		V_{oc} [V]	J_{sc} [mA/cm ²]	FF [%]	PCE [%]
75	Best	1.00	23.24	68.27	15.86
	Average	0.96 ± 0.05	22.70 ± 0.45	67.95 ± 3.50	14.79 ± 0.79
225	Best	1.07	22.17	76.27	18.14
	Average	1.05 ± 0.01	22.33 ± 0.50	74.42 ± 1.56	17.51 ± 0.25
450	Best	1.05	21.67	76.41	17.43
	Average	1.04 ± 0.01	21.06 ± 0.45	76.64 ± 0.86	16.84 ± 0.27

Table 3.3. Flexible perovskite solar cell performances. (average : 30 devices, active area : 0.078 cm²)

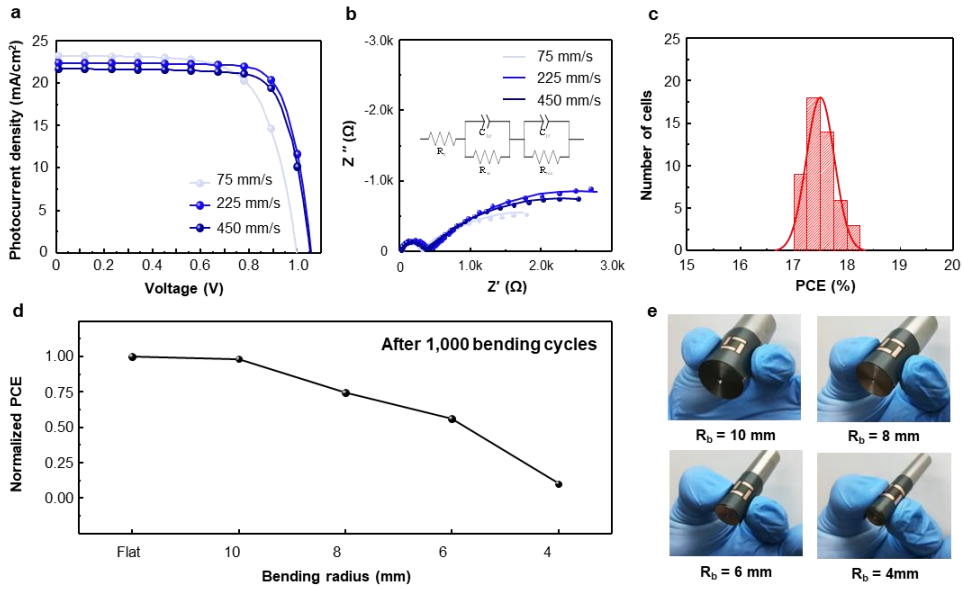


Figure 3.10. (a) $J-V$ curves of the best performing sub-cells at three coating conditions. (b) EIS Nyquist plots of the f-PSCs at three coating conditions measured under bias voltage of 0.8 V, which is fitted by the equivalent circuit model (inset). (c) Efficiency distribution of 50 devices with a coating speed of 225 mm/s. (d) Normalized PCEs of f-PSCs after 1000 bending cycles and (e) photographs of f-PSCs under various bending radius ($R_b = \infty, 10, 8, 6, 4$ mm).

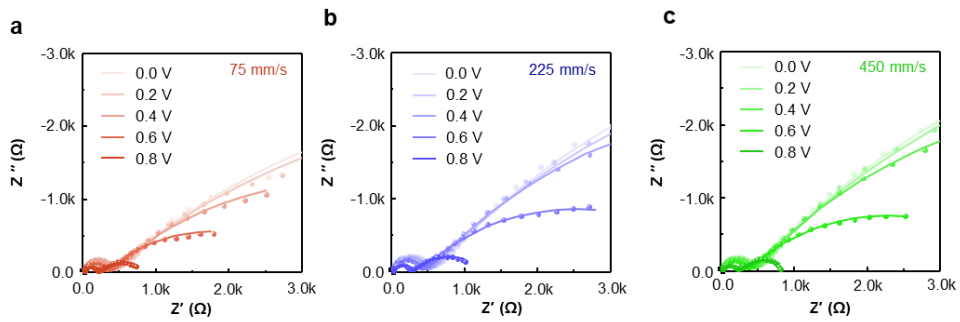


Figure 3.11. EIS Nyquist plots with fitted plots under coating speed of (a) 75, (b) 225 and (c) 450 mm/s for voltages in the range 0-0.8 V.

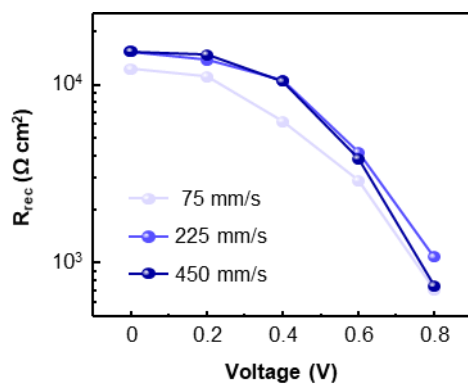


Figure 3.12. Resistance of the perovskite layer of the f-PSCs, measured under various bias voltages. The plotted values were obtained from EIS measurements under 100 mW/cm² of white LED with voltages in the range 0-0.8 V.

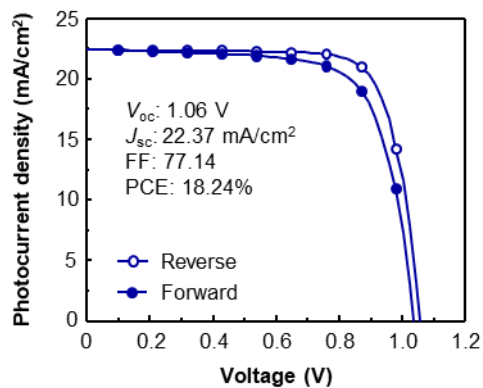


Figure 3.13. *J-V* characteristics of the best f-PSC fabricated by the FGMSC system with a coating speed of 225 mm/s (active area of 0.078 cm²).

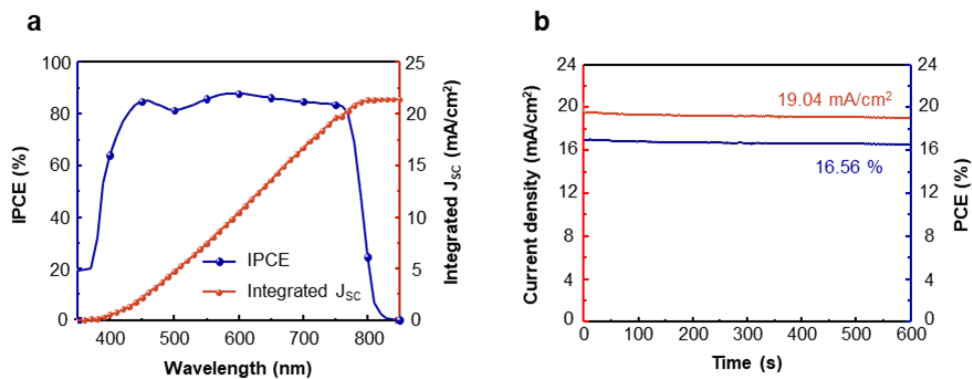


Figure 3.14. (a) IPCE and integrated J_{sc} of the 225 mm/s device with an active area of 0.078 cm². (b) Stabilized photocurrent density (red) and PCE (blue) measured at maximum power voltage of 0.87 V for 600 seconds of the 225 mm/s device with an active area of 0.078 cm².

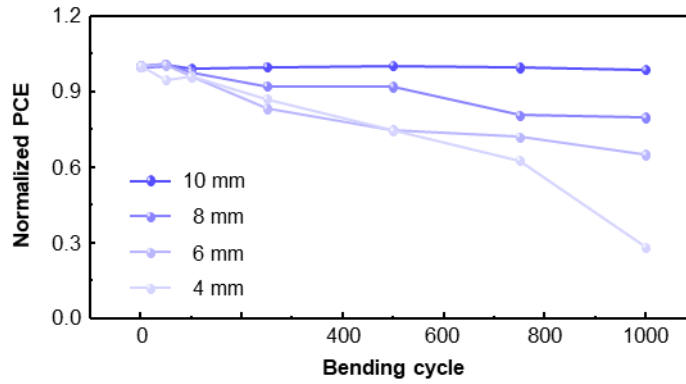


Figure 3.15. Normalized PCEs of the f-PSCs coated by the FGMSC system with a coating speed of 225 mm/s according to the bending cycles under various bending radius.

3.2.5. Large-Area (100 cm²) f-PSCs and Flexible Perovskite Solar Mini-Module.

For real-world power source application of FGMSC system, it is crucial to produce high-quality, large-scale devices. Noting this importance, we confirmed the scalability of the FGMSC system by coating a large-area perovskite film (10 × 10 cm²) on the flexible substrates (inset of **Figure 3.16c**), and then fabricating 64 sub-cells on the film (Active area of each cell is 0.078 cm².) As **Figure 3.17** shows, the film showed thicknesses of 916.2 ± 40.1 nm at the maximum, 795.4 ± 29.5 nm at the minimum and 855.7 ± 51.2 nm on the average, which indicates the consistent thickness similar with a small-area coated film (in **Table 3.4**). In terms of performance as presented in **Figure 3.16a** and **Table 3.5.**, the large-area coated film exhibited the highest PCE of 18.04% with V_{oc} of 1.06 V, J_{sc} of 22.40 mA/cm² and FF of 75.76, which suggests that there was little performance reduction compared to a small-area coated film. There are four sub-cells in different locations and **Figure 3.16c** displays the average PCEs of the sub-cells at each location. As can be seen, the PCEs are quite constant disregarding the locations; 17.71 ± 0.17% at the maximum, 17.30 ± 0.12% at the minimum was and 17.47 ± 0.22% on the average. This proves that our FGMSC system can satisfactorily perform scalable production of f-PSCs. (**Table 3.6** list PCEs of the sub-cells.)

To explore the feasibility of acquiring substantial power source, we made flexible perovskite solar mini-module, as presented in **Figure 3.18a**. **Figure 3.18b** exhibits the *I-V* curves with active area of 35.1 cm². The PCE from reverse scan is 16.10% without hysteresis (**Table 3.5**). We examined intrinsic operational flexible module stability under continuous 1-sun illumination (**Figure 3.18c**). The flexible

module was glass-to-glass encapsulated and sustained 97% of its initial efficiency after 200 h.

Location	Max [nm]	Min [nm]	Deviation b/w Max and Min [nm]	Average thickness [nm]
A	906.5	751.9	154.6	830.4 ± 49.2
B	986.9	743.9	243.0	869.8 ± 90.2
C	900.1	818.8	81.4	871.1 ± 28.2
D	943.9	806.4	137.5	869.0 ± 49.5
E	901.4	800.4	101.0	853.8 ± 32.8
F	844.3	794.4	49.9	818.8 ± 19.7
G	898.1	816.5	81.6	855.0 ± 28.6
H	948.1	831.4	116.8	877.7 ± 42.1
Average	916.2 ± 40.1	795.4 ± 29.5	120.7 ± 55.8	855.7 ± 51.2

Table 3.4. Thickness of large-area (100 cm²) perovskite layer at selected locations (A-H) under the coating speed of 225 mm/s with 3 cycles.

Active area [cm ²]			V_{oc} [V]	J_{sc} [mA/cm ²]	FF [%]	PCE [%]
64 cells	0.078	Best	1.06	22.40	75.76	18.04
		Average	1.05 ± 0.01	22.31 ± 0.38	74.41 ± 1.44	17.47 ± 0.22
Active area [cm ²]			V_{oc} [V]	I_{sc} [mA]	FF [%]	PCE [%]
Module (12 cells)	35.1	Reverse	12.92	60.60	72.19	16.10
		Forward	12.88	61.03	70.36	15.76

Table 3.5. Photovoltaic parameters of large-area (100 cm²) coated f-PSCs (64 sub-cells with the active area of 0.078 cm²) and flexible perovskite solar mini-module with active area of 35.1 cm².

Number of cells	V_{oc} [V]	J_{sc} [mA/cm²]	FF [%]	PCE [%]
1	1.06	22.40	75.76	18.04
2	1.05	22.12	76.30	17.70
3	1.05	22.36	75.06	17.64
4	1.06	22.32	73.03	17.29
5	1.05	22.42	74.91	17.69
6	1.06	22.97	73.60	17.91
7	1.04	23.05	72.13	17.27
8	1.05	22.53	72.40	17.21
9	1.06	22.99	73.25	17.78
10	1.06	22.46	74.57	17.71
11	1.05	22.72	72.25	17.19
12	1.05	22.08	75.10	17.44
13	1.06	22.13	73.61	17.25
14	1.05	22.20	75.92	17.73
15	1.06	22.98	72.77	17.66
16	1.06	21.94	75.47	17.48
17	1.05	22.36	75.10	17.61
18	1.05	22.42	74.89	17.65
19	1.06	22.08	76.60	18.00
20	1.06	22.33	74.37	17.58
21	1.06	22.85	72.95	17.63
22	1.05	23.06	73.17	17.79
23	1.05	22.16	73.89	17.19
24	1.05	22.08	75.65	17.50
25	1.05	22.00	75.77	17.53
26	1.06	22.47	73.55	17.51
27	1.04	21.94	75.42	17.21
28	1.06	22.21	73.48	17.34
29	1.06	21.51	76.79	17.44
30	1.07	21.91	76.08	17.79
31	1.04	23.03	72.55	17.37
32	1.05	22.41	73.97	17.39
33	1.06	22.05	75.09	17.47
34	1.05	22.34	72.97	17.15

35	1.06	22.40	73.11	17.36
36	1.05	22.52	74.47	17.65
37	1.05	22.17	76.71	17.83
28	1.05	22.02	75.46	17.50
39	1.04	22.49	73.93	17.35
40	1.06	22.21	73.86	17.36
41	1.06	22.51	72.94	17.36
42	1.05	22.76	72.41	17.30
43	1.04	21.66	76.56	17.32
44	1.05	21.98	76.74	17.68
45	1.04	21.72	76.54	17.24
46	1.06	22.34	73.17	17.34
47	1.06	21.72	76.07	17.54
48	1.04	22.40	74.11	17.27
49	1.05	21.85	75.39	17.28
50	1.06	22.33	75.34	17.77
51	1.05	22.73	73.16	17.51
52	1.06	22.20	73.67	17.25
53	1.06	22.36	72.92	17.25
54	1.05	21.50	76.89	17.43
55	1.06	22.45	73.43	17.41
56	1.05	22.54	72.74	17.20
57	1.06	22.44	72.55	17.20
58	1.05	22.40	73.70	17.34
59	1.06	22.87	72.29	17.48
60	1.04	21.68	76.40	17.20
61	1.05	22.07	76.81	17.79
62	1.04	22.91	72.69	17.35
63	1.05	21.84	75.38	17.34
64	1.06	21.86	74.10	17.17
Average	1.05 ± 0.01	22.31 ± 0.38	74.41 ± 1.44	17.47 ± 0.22

Table 3.6. Photovoltaic parameters of 64 sub-cells with coating area of 100 cm².

The perovskite layer was coated by the FGMSC system with coating speed of

225 mm/s with 3 cycles (active area of 0.078 cm²).

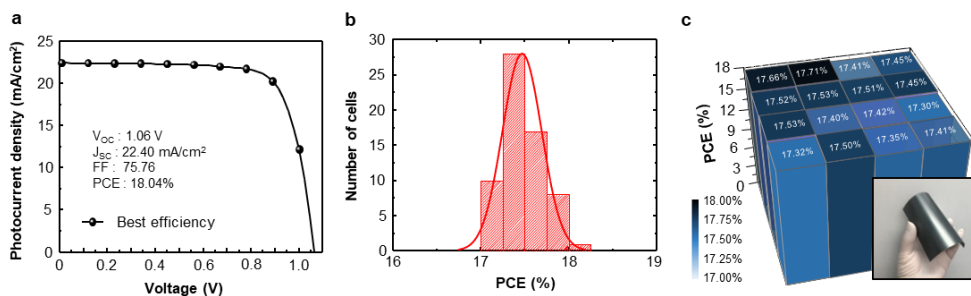


Figure 3.16. (a) J - V curve of the best performing flexible perovskite sub-cell (active area of 0.078 cm²). (b) Photovoltaic performance distribution of 64 sub-cells. (c) Average PCEs of sub-cells at each location. (four sub-cells in each location) and photograph of large-area (100 cm²) flexible perovskite film (inset).

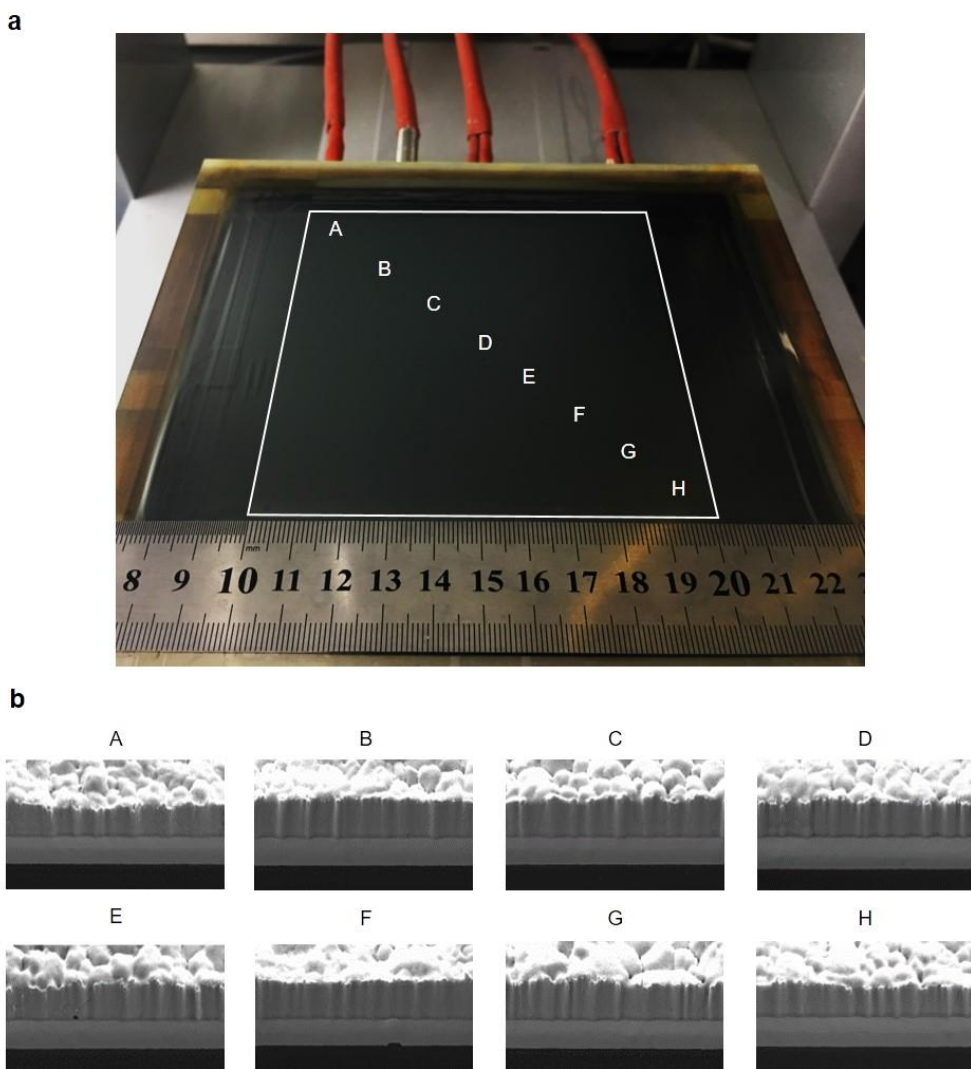


Figure 3.17. (a) Photograph of large-area (100 cm²) perovskite film coated by the FGMSC system. We selected eight locations diagonally in the coated substrate to identify uniformity of the film. (b) FIB-cross-sectional images of the perovskite film obtained from the selected locations.

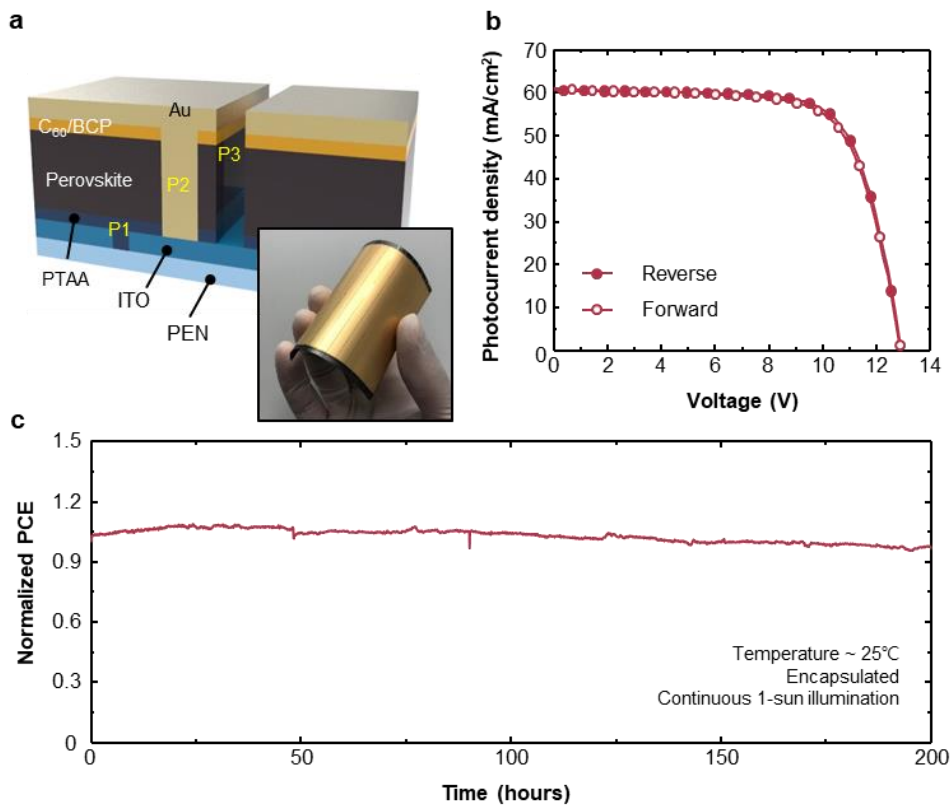


Figure 3.18. (a) Schematic of cross-section view and photograph of flexible perovskite solar mini-module. (b) I - V curves of flexible perovskite solar mini-module with active area of 35.1 cm². (c) Efficiency degradation tracking of the glass-to-glass encapsulated flexible perovskite solar mini-module under continuous 1-sun illumination. These devices are coated by the FGMSC system with coating speed of 225 mm/s.

3.3. Conclusion

We have developed an automated, sustainable FGMSC system that continuously produces high-performance flexible perovskite solar cells and modules. By using fine perovskite droplets ($< 10 \mu\text{m}$) and coating repetition technique, we have coated pinhole-free, uniform perovskite films with large grain sizes on the flexible substrates and confirmed the results with the SEM, TRPL, XRD and EIS analysis. Our f-PSCs boasted the best PCE of 18.24%. The fabrication of large-area (100cm^2) f-PSCs with the average PCE of $17.47 \pm 0.22\%$ and flexible perovskite solar mini-module with the PCE of 16.10% in the active area of 35.1 cm^2 proves the exceptional scalability of the FGMSC system. Our FGMSC system, therefore, is a practical fabrication technique for large-area, highly efficient f-PSMs.

3.4. Experimental Methods

3.4.1. Design of the FGMSC System

A schematic diagram of the FGMSC system is provided in **Figure 3.4**. There are two principal parts in the system: (1) megasonic aerosol generation and (2) spray motion control. In the former part, micro-sized aerosol droplets ($< 10 \mu\text{m}$, **Figure 3.3**) are generated with a narrow size distribution by high frequency generator (1.7 MHz, EMKnetworks Corp.). To generate droplets continuously and consistently, the generator is supplied with the perovskite solution by using a digital syringe pump (LEGATO 100, KdScientific). The droplets, then, are transported to the part of spray motion control by the N_2 carrier gas where the flow rate is managed by the mass flow controller (Bronkhorst High-Tech). The spray part consists of a metal slit-nozzle ($2 \times 25 \text{ mm}^2$) and the 2-axes (X, Y-axis) motion control system with a hot-plate (DST Robot). When the substrates are arranged, the temperature of the plate can be specifically managed. The setup is entirely automatic, which means that the spray operation is precisely controlled to coat uniform films on multiple substrates and in different locations of the same device.

3.4.2. Fabrication of f-PSCs Using the FGMSC System

Indium tin oxide (ITO) coated polyethylene naphthalate (PEN) (PEN/ITO) substrates are mounted on polydimethylsiloxane (PDMS, Dow Corning, Sylgard 184) thin-film coated bare-glass and are treated with O₂ plasma with 25 W for 30 s to eliminate any remaining solvent and to achieve better surface wettability. Poly(triaryl amine) (PTAA, MS solution) solution is spin-coated on the substrates at 6000 rpm for 30 s and dried at 100 °C for 10 min. The (CsPbI₃)_{0.02}(FA_{0.8}MA_{0.2}Pb(I_{2.8}Br_{0.2}))_{0.98} perovskite precursor solution droplets are then sprayed on the substrates through the FGMSC system. The perovskite solution is composed by dissolving PbI₂ (Alfa Aesar)/Formamidinium iodide (FAI, GreatCell Solar)/Methylammonium bromide (MABr, GreatCell Solar) (1:0.8:0.2 molar ratio) into γ -Butyrolactone (GBL, Junsei)/N,N-dimethylformamide (DMF, Sigma Aldrich)/dimethyl sulfoxide (DMSO, Sigma Aldrich) (16:4:1.125 volume ratio) at 28.8 wt%. The substrates are mounted on a hot-plate, located 1 mm under the spray nozzle. The temperature of the hot-plate is 60 °C during the spraying. The substrates are then post-annealed at 115 °C for 45 min in ambient condition. In the case of large-area (10 × 10 cm²) perovskite film fabrication, sixteen substrates of 2.5 × 2.5 cm² are mounted on the hotplate, as presented in Movie S1. The system does not require any other optimization to scale up. All FGMSC and annealing processes are conducted in a chemical fume hood under ambient conditions. After the annealing processes, fullerene (C₆₀, 20 nm), bathocuproine (BCP, 6 nm), and Cu (50 nm) are consecutively deposited with a thermal evaporator (Ultech). To produce flexible perovskite solar mini-modules, the ITO electrode, PTAA/perovskite/C₆₀/BCP stacking layer, and Au electrode (100nm) are ablated by a pico-second laser scribe

(Advanced Optowave) to pattern p1, p2, p3 (**Figure 3.18a**).

3.4.3. Characterizations and Measurements

The current density-voltage (J - V) characteristics were measured by using a source meter (Keithley 2400, Tektronix) under AM 1.5G illumination conditions with an intensity of 100 mW/cm^2 by an Oriel S013 ATM solar simulator, calibrated by a KG5 filtered monocrystalline silicon reference solar cell (91150-KG5, Newport). We tested our devices at room temperature ($25 \text{ }^\circ\text{C}$) in a glove box. The scan rates were set to $50 \text{ ms per } 20 \text{ mV}$. A metal shadow mask of 0.078 cm^2 covered the devices to limit the size of the active area. The Newport IQE200 system equipped with a 300 mW Xenon lamp and a lock-in amplifier was used to measure the external quantum efficiency (EQE) spectra. The size distribution of sprayed droplets was analyzed by sympatec HELOS laser diffraction droplet sizing system (Sympatec Inc., Clausthal, Germany). SmartDrop (FEMTOBIOMED) checked contact angles. Scanning electron microscope (SEM) images of the surfaces were acquired by field-emission SEM (MERLIN, Carl Zeiss), while cross-sectional images were obtained by focused-ion-beam SEM (FIB-SEM) system (AURIGA, Carl Zeiss). The crystal structure was characterized through X-ray diffraction (XRD) analysis by using New D8 Advance (Bruker). Electrochemical impedance spectroscopy (EIS) measurement was conducted at an electrochemical workstation (Autolab, 320N, Metrohm) equipped with an Autolab LED driver kit. EIS measurements were performed at each of bias voltages with intensity of 100 mW/cm^2 by using a white LED light (LDCNW, Autolab) with frequency of 0.1 - 1 MHz . The EIS spectra were fitted by the Z-View software (Scribner Associates). The absorption spectra were recorded by an ultraviolet-visible/near-infrared (NIR) spectrophotometer (Cary 5000, Agilent Technologies). Time-resolved photoluminescence (TRPL) analysis were performed

by a FluoroMax-4 spectrofluorometer (Horiba). A 463-nm laser diode (DeltaDiode-470L, Horiba), pulsed at the frequency of 100 MHz, was used as a light source for photoexcitation. The resulting PL was measured by a high-sensitivity photon counting NIR detector. The continuous 1-sun illumination stability test of flexible perovskite solar mini-module was performed by using reliability measurement equipment (K3600, McScience). *I-V* characteristics of the module was measured every 5 minutes.

3.5. References

- [1] M. A. Green, A. Ho-Baillie, H. J. Snaith, *Nat. Photonics*, **2014**, *8*, 506-514.
- [2] W. S. Yang, J. H. Noh, N. J. Jeon, Y. C. Kim, S. Ryu, J. Seo, S. I. Seok, *Science*, **2015**, *348*, 1234-1237.
- [3] W. S. Yang, B.-W. Park, E. H. Jung, N. J. Jeon, Y. C. Kim, D. U. Lee, S. S. Shin, J. Seo, E. K. Kim, J. H. Noh, S. I. Seok, *Science*, **2017**, *356*, 1376-1379.
- [4] E. H. Jung, N. J. Jeon, E. Y. Park, C. S. Moon, T.-J. Shin, T. Y. Yang, J. H. Noh, J. Seo, *Nature*, **2019**, *567*, 511-515.
- [5] Q. Jiang, Y. Zhao, X. Zhang, X. Yang, Y. Chen, Z. Chu, Q. Ye, X. Li, Z. Yin, J. You, *Nat. Photonics*, **2019**, *13*, 460-466.
- [6] NREL chart, accessed: March 2022, <https://www.nrel.gov/pv/cell-efficiency.html>.
- [7] J. Yoon, H. Sung, G. Lee, W. Cho, N. Ahn, H. S. Jung, M. Choi, *Energy Environ. Sci.*, **2017**, *10*, 337-345.
- [8] J. Feng, X. Zhu, Z. Yang, X. Zhang, J. Niu, Z. Wang, S. Zuo, S. Priya, S. Liu, D. Yang, *Adv. Mater.*, **2018**, *30*, 1801418.
- [9] C. Wu, D. Wang, Y. Zhang, F. Gu, G. Liu, N. Zhu, W. Luo, D. Han, X. Guo, B. Qu, S. Wang, Z. Bian, Z. Chen, L. Xiao, *Adv. Funct. Mater.*, **2019**, *29*, 1902974.
- [10] G. Lee, M. Kim, Y. W. Choi, N. Ahn, J. Jang, J. Yoon, S. M. Kim, J.-G. Lee, D. Kang, H. S. Jung, M. Choi, *Energy Environ. Sci.*, **2019**, *12*, 3182-3191.
- [11] H. S. Jung, G. S. Han, N.-G. Park, M. J. Ko, *Joule*, **2019**, *3*, 1850-1880.

- [12] L. Yang, Q. Xiong, Y. Li, P. Gao, B. Xu, H. Lin, X. Li, T. Miyasaka, *J. Mater. Chem. A*, **2021**, *9*, 1574-1582.
- [13] Z. Yang, C.-C. Chueh, F. Zuo, J. H. Kim, P.-W. Liang, A. K.-Y. Jen, *Adv. Energy Mater.*, **2015**, *5*, 1500328
- [14] Y. Galagan, F. D. Giacomo, H. Gorter, G. Kirchner, I. d. Vries, R. Andriessen, P. Groen, *Adv. Energy Mater.*, **2018**, *8*, 1801935.
- [15] Y. Y. Kim, T.-Y. Yang, R. Suhonen, M. Valimaki, T. Maaninen, A. Kemppainen, N. J. Jeon, J. Seo, *Adv. Sci.*, **2019**, *6*, 1802094.
- [16] J.-W. Lee, D.-K. Lee, D.-N. Jeong, N.-G. Park, *Adv. Funct. Mater.*, **2018**, *29*, 1807047.
- [17] M. He, B. Li, X. Cui, B. Jiang, Y. He, Y. Chen, D. O'Neil, P. Szymanski, M. A. El-Sayed, J. Huang, Z. Lin, *Nat. Commun.*, **2017**, *8*, 16045.
- [18] W.-Q. Wu, Z. Yang, P. N. Rudd, Y. Shao, X. Dai, H. Wei, J. Zhao, Y. Fang, Q. Wang, Y. Liu, Y. Deng, X. Xiao, Y. Feng, J. Huang, *Sci. Adv.*, **2019**, *5*, eaav8925.
- [19] H.-J. Kim, H.-S. Kim, N.-G. Park, *Adv. Energy Sustainability Res.*, **2021**, *2*, 2000051.
- [20] D.-K. Lee, K.-S. Lim, J.-W. Lee, N.-G. Park, *J. Mater. Chem. A*, **2021**, *9*, 3018-3028.
- [21] J. W. Yoo, J. Jang, U. Kim, Y. Lee, S.-G. Ji, E. Noh, S. Hong, M. Choi, S. I. Seok, *Joule*, **2021**, *5*, 2420-2436.
- [22] T. M. Schmidt, T. T. Larsen-Olsen, J. E. Carle, D. Angmo, F. C. Krebs, *Adv. Energy Mater.*, **2015**, *5*, 1500569.
- [23] B. Dou, J. B. Whitaker, K. Bruening, D. T. Moore, L. M. Wheeler, J. Ryter, N. J. Breslin, J. J. Berry, S. M. Garner, F. S. Barnes, S. E. Shaheen, C. J.

- Tassone, K. Zhu, M. F. A. M. v. Hest, *ACS Energy Lett.*, **2018**, *3*, 2558-2565.
- [24] J.-E. Kim, S.-S. Kim, C. Zuo, M. Gao, D. Vak, D.-Y. Kim, *Adv. Funct. Mater.*, **2019**, *29*, 1809194.
- [25] Y. Deng, X. Zheng, Y. Bai, Q. Wang, J. Zhao, J. Huang, *Nat. Energy*, **2018**, *3*, 560-566.
- [26] X. Dai, Y. Deng, C. H. V. Brackle, J. Huang, *Int. J. Extrem. Manuf.*, **2019**, *1*, 022004.
- [27] M. Remeika, L. K. Ono, M. Maeda, Z. Hu, Y. Qi, *Org. Electron.*, **2018**, *54*, 72-79.
- [28] S. C. Hong, G. Lee, K. Ha, J. Yoon, N. Ahn, W. Cho, M. Park, M. Choi, *ACS Appl. Mater. Interfaces*, **2017**, *9*, 7879-7884.
- [29] M. Park, W. Cho, G. Lee, S. C. Hong, M. Kim, J. Yoon, N. Ahn, M. Choi, *Small*, **2019**, *15*, 1804005.
- [30] S. Bag, J. R. Deneault, M. F. Durstock, *Adv. Energy Mater.*, **2017**, *7*, 1701151.
- [31] J. H. Heo, M. H. Lee, M. H. Jang, S. H. Im, *J. Mater. Chem. A*, **2016**, *4*, 17636-17642.
- [32] D. S. Lee, M. J. Ki, H. J. Lee, J. K. Park, S. Y. Hong, B. W. Kim, J. H. Heo, S. H. Im, *ACS Appl. Mater. Interfaces*, **2022**, *14*, 7926-7935.
- [33] J. E. Bishop, C. D. Read, J. A. Smith, T. J. Routledge, D. G. Lidzey, *Sci Rep*, **2020**, *10*, 6610.
- [34] J. E. Bishop, J. A. Smith, D. G. Lidzey, *ACS Appl. Mater. Interfaces*, **2020**, *12*, 48237-48245.
- [35] S. Han, H. Kim, S. Lee, C. Kim, *ACS Appl. Mater. Interfaces*, **2018**, *10*, 7281-7288.

- [36] Y. Jiang, C. Wu, L. Li, K. Wang, Z. Tao, F. Gao, W. Cheng, J. Cheng, X.-Y. Zhao, S. Priya, W. Deng, *Nano Energy*, **2018**, *53*, 440-448.
- [37] W.-N. Wang, A. Purwanto, I. W. Lenggoro, K. Okuyama, H. Chang, H. D. Jang, *Ind. Eng. Chem. Res.*, **2008**, *47*, 1650-1659.
- [38] A. T. Barrows, A. J. Pearson, C. K. Kwak, A. D. F. Dunbar, A. R. Buckley, D. G. Lidzey, *Energy Environ. Sci.*, **2014**, *7*, 2944.
- [39] H. Huang, J. Shi, L. Zhu, D. Li, Y. Luo, Q. Meng, *Nano Energy*, **2016**, *27*, 352-358.
- [40] S. Ulicna, B. Dou, D. H. Kim, K. Zhu, J. M. Walls, J. W. Bowers, M. F. A. M. v. Hest, *ACS Appl. Energy Mater.*, **2018**, *1*, 1853-1857.
- [41] S. C. Tsai, Y. L. Song, C. S. Tsai, C. C. Yang, W. Y. Chiu, H. M. Lin, *J. Mater. Sci.*, **2004**, *39*, 3647-3657.
- [42] Z. Liang, S. Zhang, X. Xu, N. Wang, J. Wang, X. Wang, Z. Bi, G. Xu, N. Yuan, J. Ding, *RSC Adv.*, **2015**, *5*, 60562-60569.
- [43] H. Zhou, Q. Chen, G. Li, S. Luo, T. Song, H.-S. Duan, Z. Hong, J. You, Y. Liu, Y. Yang, *Science*, **2014**, *345*, 542-546.
- [44] B. Park, B. Philippe, S. M. Jain, X. Zhang, T. Edvinsson, H. Rensmo, B. Zietz, G. Boschloo, *J. Mater. Chem. A*, **2015**, *3*, 21760-21771.
- [45] M. Kim, B. J. Kim, D.-Y. Son, N.-G. Park, H. S. Jung, M. Choi, *Nano Lett.*, **2016**, *16*, 5756-5763.
- [46] M. Saliba, T. Matsui, J.-Y. Seo, K. Domanski, J.-P. Correa-Baena, M. K. Nazeeruddin, S. M. Zakeeruddin, W. Tress, A. Abate, A. Hagfeldt, M. Gratzel, *Energy Environ. Sci.*, **2016**, *9*, 1989-1997.
- [47] H. Sung, N. Ahn, M. S. Jang, J.-K. Lee, H. Yoon, N.-G. Park, M. Choi, *Adv. Energy Mater.*, **2016**, *6*, 1501873.

- [48] G. Murugadoss, R. Thangamuthu, S. Vijayaraghavan, H. Kanda, S. Ito, *Electrochim. Acta*, **2017**, *257*, 267-280.
- [49] V. Gonzalez-Pedro, E. J. Juarez-Perez, W.-S. Arsyad, E. M. Barea, F. Fabregat-Santiago, I. Mora-Sero, J. Bisquert, *Nano Lett.*, **2014**, *14*, 888-893.
- [50] J. A. Christians, R. C. Fung, P. V. Kamat, *J. Am. Chem. Soc.*, **2014**, *136*, 758-764.
- [51] Q. Tai, P. You, H. Sang, Z. Liu, C. Hu, H. L. Chan, F. Yan, *Nat. commun.*, **2016**, *7*, 11105.
- [52] B. J. Kim, D. H. Kim, Y.-Y. Lee, H.-W. Shin, G. S. Han, J. S. Hong, K. Mahmood, T. K. Ahn, Y.-C. Joo, K. S. Hong, N.-G. Park, S. Lee, H. S. Jung, *Energy Environ. Sci.*, **2015**, *8*, 916-921.

Chapter 4. Charge Transport Layer Coating via Megasonic-Spray Coating System

4.1. Introduction

Commercialization of perovskite solar cells (PSCs) requires effective scalable coating process beyond spin-coating process from lab-scale experiments. Various scalable coating methods (e.g. bar-coating, slot-die coating, spray-coating) have been studied for fabrication of large-area PSCs.[1-9] However, most of the research has only focused on scalable coating of perovskite active layers and charge transport layers (CTL) (e.g. Electron transport layer (ETL), Hole transport layer (HTL)) have rarely been investigated in depth.[1-9]

Inverted PSCs have structure of Substrate/TCO (Transparent Conductive Oxide)/HTL/Perovskite/ETL/Electrode.[6, 7, 9] Among them, HTL and perovskite layer are mostly coated by solution process, and ETL/electrodes are mainly deposited by thermal evaporation. Therefore, if only the HTL/perovskite layer coating is conducted by scalable coating method, the subsequent layers can be coated at once by thermal evaporation process, and then it would be applicable to continuous roll-to-roll or sheet-to-sheet manufacturing. In our previous work, we already demonstrated coating of high-crystalline, large-area perovskite layers on both glass substrates and flexible substrates via megasonic-spray coating (MSC) process. In this study, we have applied the MSC method to the HTL layer coating (especially PTAA (poly(triaryl amine) layer). Through the optimization of both

substrate temperature condition and multiple megasonic-spray coatings, we have successfully obtained PTAA films which have the same quality as the spin-coated films. These results suggest that the megasonic-spray coating method is a highly practical, continuous coating process in commercialization of PSCs.

4.2. Results and Discussion

In the beginning, the megasonic-spray nozzle moving speed is fixed with the maximum speed of 500 mm/s to minimize the supply rate of the PTAA droplets to satisfy the extremely thin target thickness (about 20 nm) of PTAA layer in the inverted PSCs. The optimization process is conducted with the distance between nozzle to the substrate as 1 mm and 2 mg/ml concentration ratio of the PTAA solution is used in reference to the spin-coating process.[7] The Glass/ITO/PTAA substrate is post-annealed at 100°C for 10 min right after the spraying process.

4.2.1. Optimization of the Substrate Temperature and Multiple Megasonic-Spray Coatings

Atomic Force Microscopy (AFM) analysis is performed to figure out both the surface morphology and the roughness of the spray-coated PTAA films according to the substrate temperature. In **Figure 4.1**, aggregation of the PTAA droplets occurs when the temperature of substrate is lower than 50°C and this phenomenon disappears above 50°C. Meanwhile, all PTAA films have pinholes and high surface roughness regardless of the substrate temperature. To control the pinholes and roughness issue, both multiple megasonic-spray coating method and higher concentration ratio of the PTAA solution (6 mg/ml) are applied.

A parameter study of the multiple megasonic-spray coating is performed in two substrate temperature conditions with and without the aggregation phenomenon. The pinholes are gradually controlled according to the repetition of the megasonic-

spray coating in every temperature condition as shown in **Figure 4.2**. However, the substrates are coated in the shape of droplet residues of the PTAA droplets after coating repetition due to the coffee-ring effect. This coffee-ring effect becomes more severe when the temperature of the substrate is increased. Considering that the target thickness is as very thin as around 20 nm, the coffee-ring effect severely affects the surface roughness. Therefore, we have done same multiple megasonic-spray coating in ambient condition without heating. Because the wet-film could be affected by the jet-force, we adjusted the distance between nozzle and the substrate to 10 mm. As a result, the droplet shape is completely disappeared and the pinholes are also controlled by coating repetition (**Figure 4.3**). In particular, 4-cycles coated PTAA film achieves 50% decreased root mean square (RMS) than the others. However, the RMS was still high and the phenomenon of aggregation of PTAA polymers had not been resolved. To control this phenomenon, further optimization was performed by lowering the concentration ratio of PTAA solution from 6mg/ml to 3mg/ml (**Figure 4.4**). In this case, 3-cycles to 5-cycles coated PTAA films show similar RMS to spin-coated film (**Figure 4.5**) and PTAA aggregation is completely disappeared. Meanwhile, the aggregation re-occurs at 6-cycles coating process because of over-crosslinking of PTAA polymers in the wet-film condition due to long process time and results in increasing of RMS.

Based on the parameter study results, we estimated the thickness of PTAA films according to the coating process by FIB-SEM measurement. As shown in **Figure 4.6**, all the PTAA films show similar morphology with uniform thickness through the measured area. Particularly, the thickness of megasonic-spray coated PTAA film is gradually increased as the coating repeats except for the 6-cycles coating process which have the over-crosslinking problem of PTAA polymers, as

mentioned above.

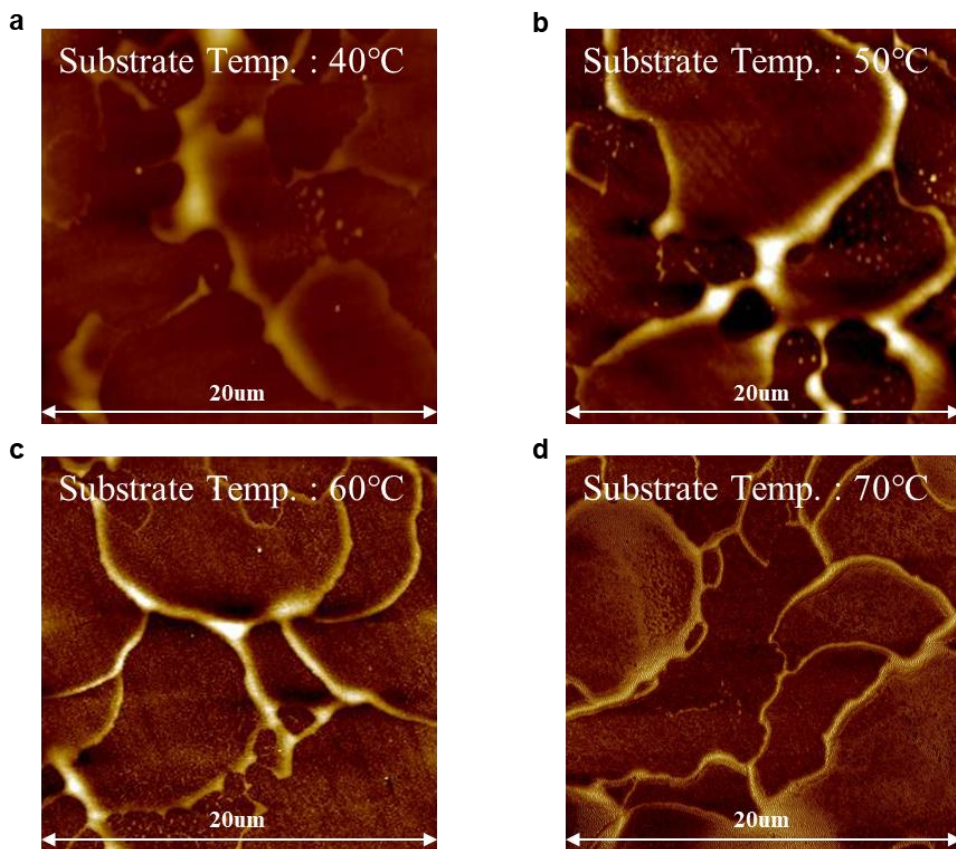


Figure 4.1. Atomic Force Microscopy height images of megasonic-spray coated PTAA films according to substrate temperature.

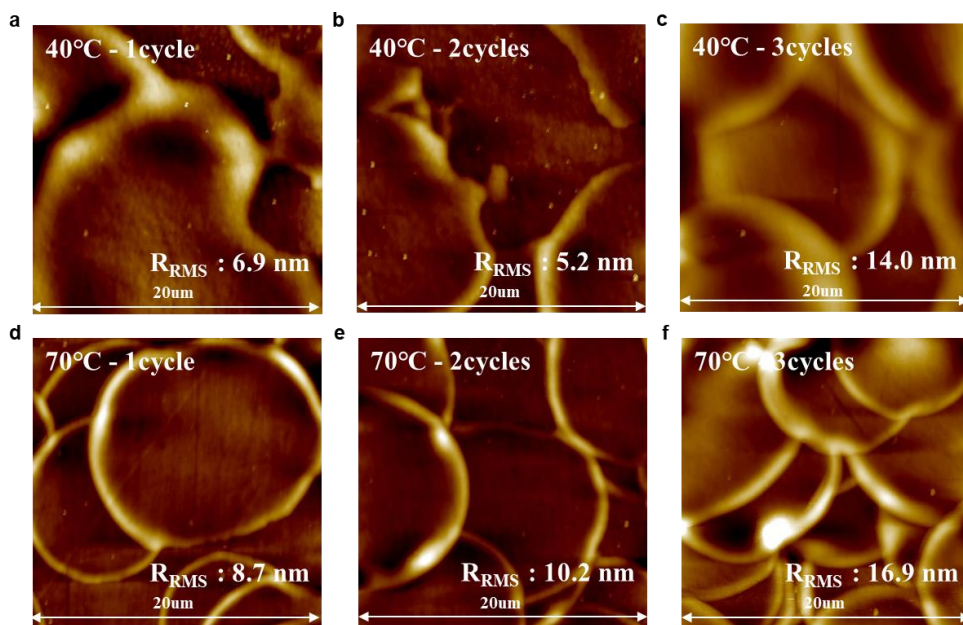


Figure 4.2. Atomic Force Microscopy height images and of megasonic-spray coated PTAA films according to coating repetition. Temperatures of substrate are (a-c) 40 °C and (d-f) 70 °C.

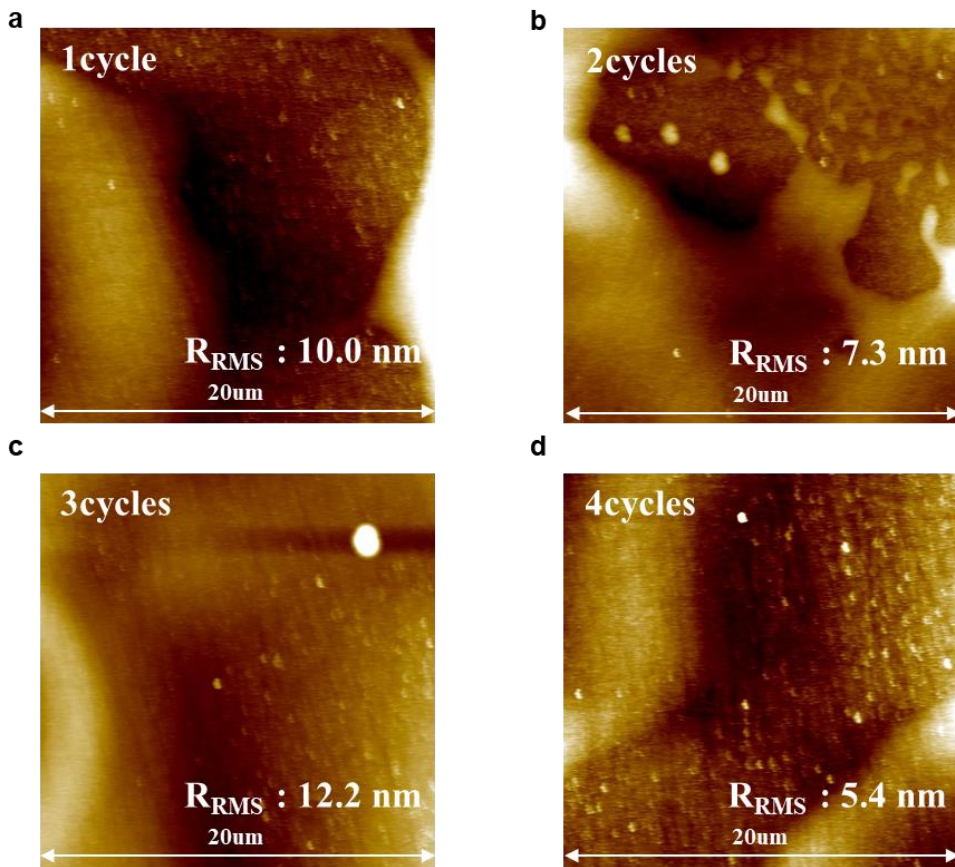


Figure 4.3. Atomic Force Microscopy height images of megasonic-spray coated PTAA films according to coating repetition at ambient conditions. The concentration of PTAA solution is 6mg/ml.

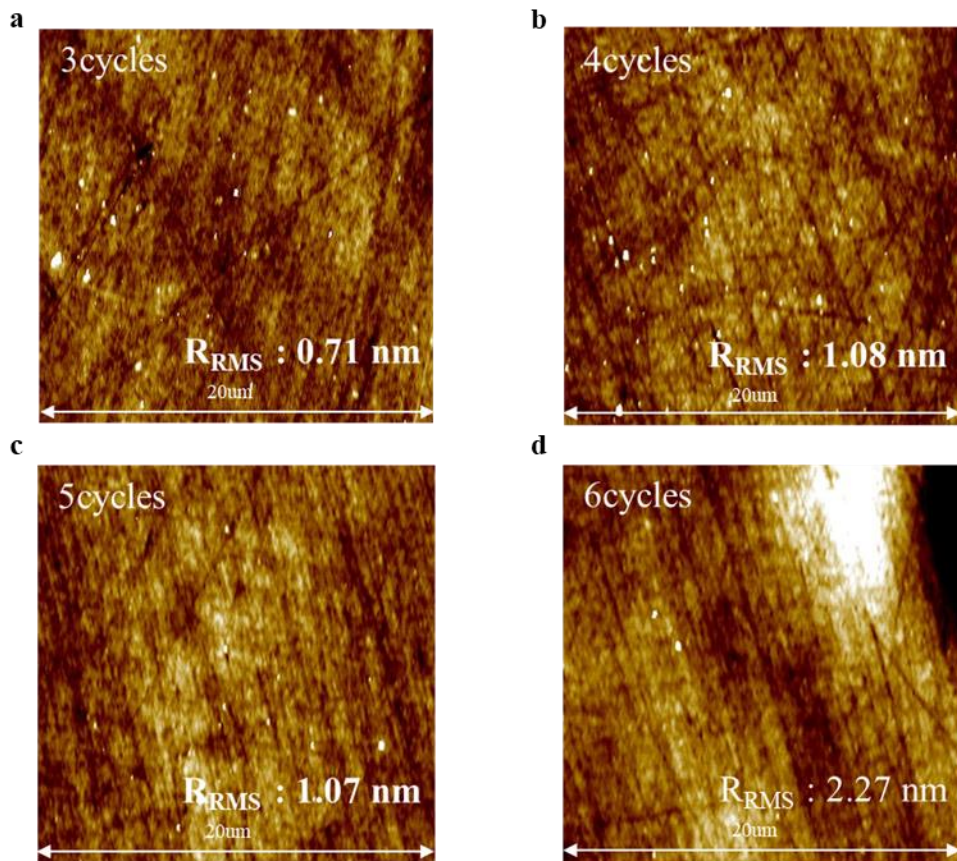


Figure 4.4. Atomic Force Microscopy height images of megasonic-spray coated PTAA films according to coating repetition at ambient conditions. The concentration of PTAA solution is 3mg/ml.

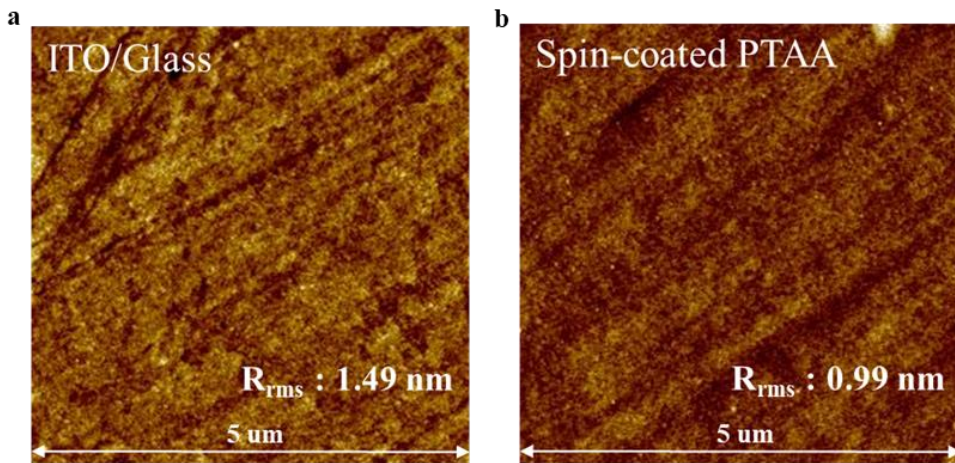
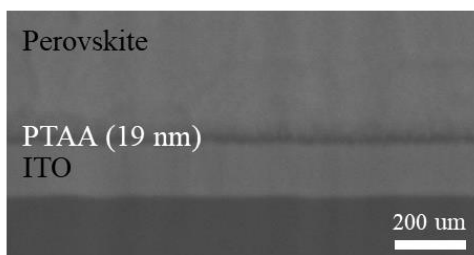


Figure 4.5. Atomic Force Microscopy height images of (a) bare ITO/Glass substrate and (b) spin-coated PTAA film.

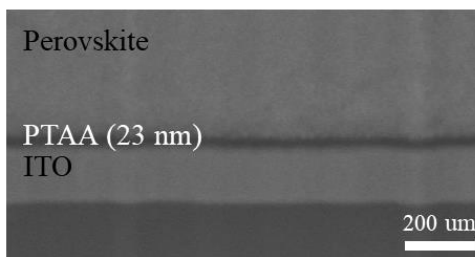
a Spin-coated PTAA



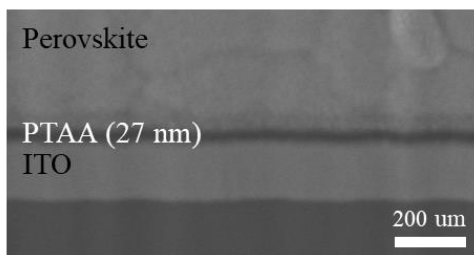
b Spray - 3 cycles



c Spray - 4 cycles



d Spray - 5 cycles



e Spray - 6cycles

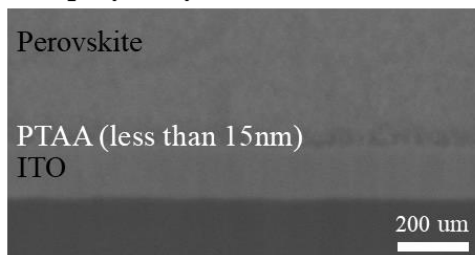


Figure 4.6. FIB-cross-section SEM images of (a) spin-coated PTAA film and (b-e) megasonic-spray coated PTAA films according to coating repetition at ambient conditions. The concentration of PTAA solution is 3mg/ml.

4.2.2. Fabrication of PSCs and Device Performance

To investigate the photovoltaic performance of devices with the spray-coated films, we prepared inverted PSCs (Glass/ITO/PTAA(spin-coating and megasonic-spray coating)/perovskite/fullerene (C_{60})/bathocuproine (BCP)/Cu) by using the perovskite composed of $FA_{0.4}MA_{0.6}Pb(I_{2.9}Br_{0.1})$. In this case, all layers of the perovskite solar cell are fabricated by scalable coating process (**Figure 4.7**). **Figure 4.8** presents photovoltaic performances of the devices. Because the fabricated perovskite layers are coated in the same megasonic-spray coating condition, the short circuit current density (J_{SC}) has a small difference. The open-circuit voltage (V_{OC}) and fill factor (FF) which are highly affected by the quality of the PTAA thin-film show difference, especially with the megasonic-spray coated PTAA devices that have large deviations. This means that although the local PTAA surface morphologies are equivalent among coating types, as discussed above, the megasonic-spray coated PTAA films have a lack of uniformity when considering the entire active area. However, as shown in the **Table 4.1**, the megasonic-spray coated cells show more effective performance than spin-coated cells in the best PCEs. These results demonstrate that the megasonic-spray coating system can produce high quality thin-films that have a thickness of tens of nanometers which has usually required solution coating process to produce.

PTAA thin-film		V_{oc} [V]	J_{sc} [mA/cm ²]	FF [%]	PCE [%]	R_{shunt} [Ω]
Spin-coating	Best	1.04	21.68	74.80	16.93	64456.03
	Average	1.03 \pm 0.01	21.50 \pm 0.20	73.73 \pm 0.96	16.35 \pm 0.40	55285.46 \pm 22512.76
Spray-coating (3 cycles)	Best	0.97	22.04	77.84	16.62	57710.60
	Average	0.95 \pm 0.05	21.85 \pm 0.19	74.77 \pm 2.26	15.58 \pm 1.00	33967.56 \pm 19770.76
Spray-coating (4 cycles)	Best	1.02	21.90	78.54	17.46	48339.53
	Average	0.97 \pm 0.06	21.64 \pm 0.15	75.79 \pm 2.54	15.93 \pm 1.48	25078.31 \pm 13783.60
Spray-coating (5 cycles)	Best	1.03	21.62	78.31	17.41	77641.03
	Average	0.98 \pm 0.05	21.43 \pm 0.55	74.94 \pm 4.00	15.77 \pm 1.63	35874.52 \pm 25123.21
Spray-coating (6 cycles)	Best	1.03	21.26	78.79	17.33	40115.28
	Average	0.96 \pm 0.08	21.30 \pm 0.23	74.98 \pm 5.26	15.40 \pm 1.98	32061.15 \pm 18594.95

Table 4.1. Perovskite solar cell performances according to the coating method.

The active area was 0.078 cm².

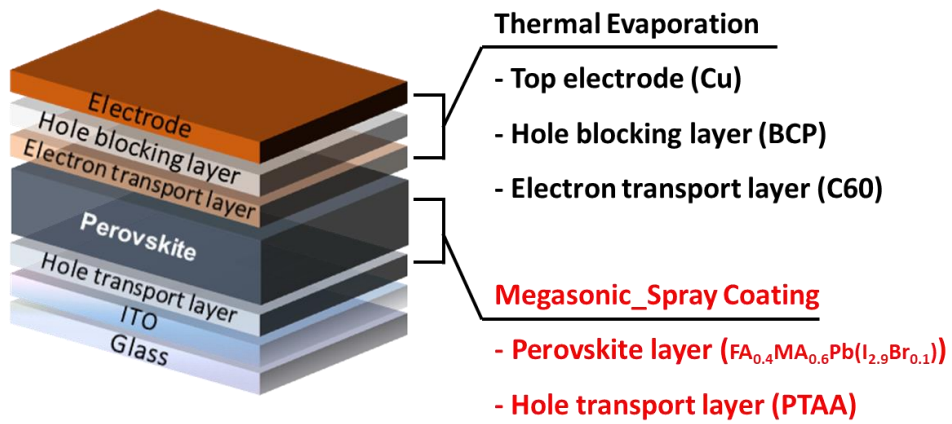


Figure 4.7. Schematic illustration of an inverted perovskite solar cell fabricated via megasonic-spray coating system.

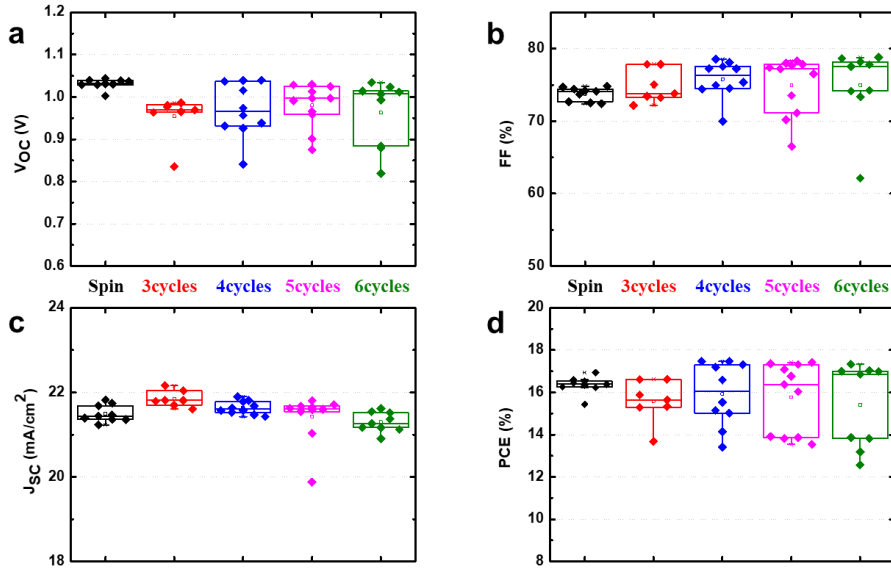


Figure 4.8. Box charts of performance parameters according to coating process of PTAA thin-film. The active area was 0.078 cm².

4.3. Conclusion

We have applied the megasonic-spray coating method to the fabrication of PTAA thin-film which is used as a hole transport layer in inverted PSCs. Optimization of the spray-coating condition is successfully conducted by the AFM and FIB-SEM analysis. We have achieved effective PCEs comparable to those of spin-coated PTAA devices. These results demonstrate that the megasonic-spray coating system can produce highly reproducible uniform films not only with the perovskite active layers but also with the charge transport layers that have a thickness of tens of nanometers. Our megasonic-spray coating method, therefore, is a highly practical, continuous fabrication technique for commercialization of perovskite solar cells.

4.4. Experimental Methods

4.4.1. Fabrication of PSCs Using the Megasonic-Spray Coating System

The poly(triaryl amine) (PTAA, MS solution) was diluted with 1,2-Dichlorobenzene (DCB, Sigma Aldrich) for megasonic-spray HTL coating. In case of spin-coating, the poly(triaryl amine) (PTAA, Sigma Aldrich) was diluted with Chlorobenzene (CB, Sigma Aldrich) and spin-coated on the substrates at 6000 rpm for 30 s. The Glass/ITO/PTAA substrate is post-annealed at 100°C for 10 min right after coating process. The FA_{0.4}MA_{0.6}Pb(I_{2.9}Br_{0.1}) perovskite precursor solution was deposited on the PTAA coated ITO/Glass substrate. The perovskite solution was prepared by dissolving PbI₂ (Alfa Aesar)/Formamidinium iodide (FAI, GreatCell Solar)/Methylammonium bromide (MABr, GreatCell Solar) (1:0.8:0.2 molar ratio) into γ -Butyrolactone (GBL, Junsei)/N,N-dimethylformamide (DMF, Sigma Aldrich)/dimethyl sulfoxide (DMSO, Sigma Aldrich) (16:4:1.125 volume ratio). The substrates were deposited on a hot-plate, located 1 mm under the nozzle. Temperature of the hot-plate was 85 °C during the spraying. After the spraying, the substrates were post-annealed at 115 °C for 45 min in air. All megasonic-spray coating and annealing processes were carried out in a chemical hood under ambient conditions. After the annealing processes, fullerene (C₆₀, 20 nm), bathocuproine (BCP, 6 nm), and Cu (50 nm) were sequentially deposited using thermal evaporator (Ultech).

4.4.2. Characterizations and Measurements

The current density-voltage (J - V) characteristics were measured using a source meter (Keithley 2400, Tektronix) under AM 1.5G illumination conditions with an intensity of 100 mW/cm² using an Oriel S013 ATM solar simulator, calibrated by a KG5 filtered monocrystalline silicon reference solar cell (91150-KG5, Newport). Our devices were tested at room temperature (25 °C) in a glove box. The scan rates were set to 50 ms per 20 mV. The devices were covered with a metal shadow mask of 0.078 cm² to restrict the size of the active area. Cross-sectional images were obtained with a focused-ion-beam (FIB) system (AURIGA, Carl Zeiss). Atomic Force Microscopy (AFM, Park Systems) analysis is performed to figure out both the surface morphology and the surface roughness of the thin-films.

4.5. References

- [1] M. He, B. Li, X. Cui, B. Jiang, Y. He, Y. Chen, D. O'Neil, P. Szymanski, M. A. El-Sayed, J. Huang, Z. Lin, *Nat. Commun.*, **2017**, *8*, 16045.
- [2] W.-Q. Wu, Z. Yang, P. N. Rudd, Y. Shao, X. Dai, H. Wei, J. Zhao, Y. Fang, Q. Wang, Y. Liu, Y. Deng, X. Xiao, Y. Feng, J. Huang, *Sci. Adv.*, **2019**, *5*, eaav8925.
- [3] H.-J. Kim, H.-S. Kim, N.-G. Park, *Adv. Energy Sustainability Res.*, **2021**, *2*, 2000051.
- [4] D.-K. Lee, K.-S. Lim, J.-W. Lee, N.-G. Park, *J. Mater. Chem. A*, **2021**, *9*, 3018-3028.
- [5] J. W. Yoo, J. Jang, U. Kim, Y. Lee, S.-G. Ji, E. Noh, S. Hong, M. Choi, S. I. Seok, *Joule*, **2021**, *5*, 2420-2436.
- [6] S. C. Hong, G. Lee, K. Ha, J. Yoon, N. Ahn, W. Cho, M. Park, M. Choi, *ACS Appl. Mater. Interfaces*, **2017**, *9*, 7879-7884.
- [7] M. Park, W. Cho, G. Lee, S. C. Hong, M. Kim, J. Yoon, N. Ahn, M. Choi, *Small*, **2019**, *15*, 1804005.
- [8] S. Bag, J. R. Deneault, M. F. Durstock, *Adv. Energy Mater.*, **2017**, *7*, 1701151.
- [9] L.-H. Chou, J. M. W. Chan, C.-L. Liu, *Solar RRL*, **2022**, *4*, 2101035.

Chapter 5. Concluding Remarks

In this dissertation, scalable spray-coating systems were developed and optimized to realize continuous fabrication of large-area perovskite solar cells (PSCs) and flexible PSCs (f-PSCs) with high power conversion efficiencies (PCEs).

First, we developed a highly reproducible megasonic-spray coating method for the fabrication of MAPbI₃ films for perovskite solar cells. In this method, high quality MAPbI₃ films can be prepared at low temperature with an anti-solvent free process at ambient conditions. The most efficient solar cells fabricated using megasonic-spray coating in our study exhibits a PCE of 16.9%, with an average PCE of 16.4%. The megasonic-spray coating was successfully applied to the continuous fabrication of uniform, highly crystalline, and large-grain MAPbI₃ films. Large-area optimized perovskite films were used to fabricate efficient PSCs with a PCE of 14.2% (with an active area of 1 cm²) and excellent film uniformity over large areas.

Second, we developed an automated, sustainable FGMSC system that continuously produces high-performance flexible perovskite solar cells and modules. By using fine perovskite droplets (< 10 μm) and coating repetition technique, we have coated pinhole-free, uniform perovskite films with large grain sizes on the flexible substrates and confirmed the results with the SEM, TRPL, XRD and EIS analysis. Our f-PSCs boasted the best PCE of 18.24%. The scalability of the system has also been validated in the fabrication of large area (100cm²) perovskite layer on a flexible substrate with uniform solar cells that have shown the average PCE of 17.47 ± 0.22% and flexible perovskite solar mini-module with PCE of

16.10% measured from an active area of 35.1 cm². Our FGMSC system, therefore, is a practical fabrication technique for large-area, highly efficient f-PSMs.

Third, we utilized the megasonic-spray coating method to the fabrication of PTAA thin-film. We successfully optimized the parameters of megasonic-spray coating by using the AFM and FIB- SEM analysis. Consequently, we have achieved effective PCEs comparable to those of spin-coated PTAA devices. These means that the megasonic-spray coating technology can fabricate highly reproducible uniform films not only with the perovskite active layers but also with the charge transport layers that have a thickness of tens of nanometers which has usually required solution coating process to produce. Our megasonic-spray coating method, therefore, is a highly practical, continuous fabrication technique for commercialization of perovskite solar cells.

Acknowledgement

This work was supported by the Global Frontier R&D Program of the Center for Multiscale Energy Systems funded by the National Research Foundation under the Ministry of Education, Science and Technology, Korea.

The research data of Chapter 2 are the result on the collaboration with Dr. Woohyung Cho. In addition, the research data have been reported in *Small* (*Small*, 2019, 15, 1804005). The results of Chapter 3 are produced by collaboration with Dr. Seung Chan Hong. In this dissertation, the results are reproduced under agree with each other, therefor it can include similar contents in dissertation of Dr. Seung Chan Hong. The research data of Chapter 3 will be published in the academic journals as co-first author.

I would like to thank my supervisor Prof. Mansoo Choi for their warm encouragement and helpful advices. I would like to especially thank Dr. Gunhee Lee, Dr. Wooik Jung, Dr. Junseop Byeon, Minsung Han, Kiwan Jeong, Yeoun-Woo Jang, Unsoo Kim, and Jihun Jang. I also appreciate all of my laboratory members for their kind support, assistance and many helps.

초 록

유기금속 할로겐화물 페로브스카이트 태양전지는 광전에너지변환을 위한 매우 유망한 차세대 태양광 발전원이다. 최근 글라스기판 기반의 페로브스카이트 태양전지 효율은 25% 이상을 달성했고, 플렉서블 페로브스카이트 태양전지 또한 그 다양한 응용 분야로 인해 수요가 증가하고있다. 이러한 추세에 발맞춰서, 페로브스카이트 태양전지의 상용화를 위해서는 스펀코팅기판의 랩스케일 공정을 뛰어넘는 대면적 연속 코팅 공정이 필수적으로 필요하다. 먼저, 우리는 1.7MHz 의 메가소닉 진동자를 활용하여, 글라스기판 위에 재현성이 확보된, 우수한 대면적 페로브스카이트 필름 코팅이 가능한 메가소닉 스프레이 코팅 공정을 개발하였다. 그 결과, 우리는 평균 16.4%, 최대 16.9%의 광전변환효율을 갖는 페로브스카이트 태양전지 소자 제작에 성공하였다. 또한 광전변환효율이 14.2%인 대면적-단일소자 제작(활성영역 : 1cm^2 , 코팅영역 : $7.5 \times 7.5 \text{ cm}^2$)에 메가소닉 스프레이 코팅 공정을 성공적으로 적용함으로써, 우리가 개발한 메가소닉 스프레이 코팅 방식이 대면적 코팅 공정에 적합하다는 것을 보여주었다. 둘째, 우리는 넓은 면적의 유연기판위에 페로브스카이트 필름을 균일하게 성장시킬 수 있는 대면적화 가능한 연속공정인 필름성장 메가소닉 스프레이 코팅(Film-Growth-Megasonic-Spray-Coating, FGMSC) 시스템을 개발하였다. 유연기판위에 스프레이 코팅을 했을 때 페로브스카이트 필름이 어떻게 성장하는지에 대한 핵심적인 원리를 심도있게 조사하였고, 그 결과 성공적으로 결함이 없는 균일한 페로브스카이트 필름을 유연기판위에 제작하였다. 또한 35.1cm^2 의 면적을 갖는 페로브스카이트 유연 태양전지모듈을 제작하여 16.1%의 광전변환효율을 달성함으로써, FGMSC 시스템의 우수한 대면적 코팅 성능을 증명하였다. 이러한 결과는, 개발한 FGMSC 시스템의 대면적 가능성과 효율성이 유연 페로브스카이트 태양전지 상용화에 적합한

자동화 코팅시스템임을 보여준다. 셋째, 페로브스카이트 태양전지를 구성하는 전하전달층(홀 전달층, 전자 전달층)의 코팅에 우리가 개발한 메가소닉 스프레이 코팅을 적용하였다. 특히, 홀 전달층으로 사용되는 PTAA(poly(triaryl amine))를 스프레이 코팅하여 성공적으로 페로브스카이트 태양전지를 제작하였다. 이는 태양전지를 이루는 모든 층이 대면적 연속공정으로 이루어진 것에 큰 의미를 가지고, 우리가 개발한 메가소닉 스프레이 코팅 기술이 실제 연속코팅공정에 적용가능한 실용적인 공정임을 보여준다.

주요어 : 페로브스카이트 태양전지, 유연 페로브스카이트 태양전지, 연속 공정, 대면적 공정, 메가소닉 스프레이 코팅

학 번 : 2016-20652

List of Publications

- [1] Seung Chan Hong†, Gunhee Lee†, Kyungyeon Ha†, Jungjin Yoon, Namyoung Ahn, Woohyung Cho, **Mincheol Park**, and Mansoo Choi* “Precise Morphology Control and Continuous Fabrication of Perovskite Solar Cells Using Droplet-Controllable Electrospray Coating System” *ACS Applied Materials & Interfaces* (2017)
- [2] **Mincheol Park**†, Woohyung Cho†, Gunhee Lee, Seung Chan Hong, Mincheol Kim, Jungjin Yoon, Namyoung Ahn and Mansoo Choi* “Highly Reproducible Large-Area Perovskite Solar Cell Fabrication via Continuous Megasonic Spray Coating of $\text{CH}_3\text{NH}_3\text{PbI}_3$ ” *Small* (2018)